UCLouvain

École polytechnique de Louvain

Development of a reference one-dimensional pyrolysis experiment

Authors: **Julien Benoit, Gilles Mottiat**
Supervisor: **Hervé Jeanmart**
Readers: **Julien Blondeau, Matthieu Duponcheel, Arnaud Rouanet**
Academic year 2019–2020
Master [120] in Mechanical Engineering

Abstract

Pyrolysis is the key step in all thermochemical biomass conversions and in the thermal protection systems of the spacial vehicles. However, these two applications are studied by different scientific communities developing their own model and code. In this work, we present the design of an experiment to benchmark the codes of both communities by permitting to measure the temperature and mass evolution of a macroscopic particle experiencing a high external heating flux in a set up allowing to assume the one-dimensionality of the problem.

A general design of this experiment has first been made. Then its dimensions have been computed with a two-dimensional preliminary model such as the difference in temperature profile of this model with a fully one-dimensional one is minimized. We have finally been able to approximate this difference thanks to the SPY algorithm. We can thus assess that the design presented in this work allows to measure the temperature and mass evolution with a difference of a few percents compared to a fully one-dimensional problem.

Remerciements

Ce travail vient marquer la fin de deux cursus remplis d'apprentissages, de rencontres et de développement personnel à l'Ecole Polytechnique de Louvain. Nous tenions donc à remercier toutes les personnes qui nous ont permis d'arriver jusqu'ici.

Nos remerciements vont tout d'abord au Pr. Jeanmart pour les conseils qu'il a pu nous prodiguer tout au long de l'élaboration de ce mémoire et particulièrement lorsque les objectifs de celui-ci ont dû être changés en raison des circonstances. Nous remercions également les membres du jury, le Pr. Blondeau, le Pr. Duponcheel et Mr. Rouanet, pour le temps qu'ils consacreront à la lecture et à l'évaluation de ce travail.

Merci à Dominique, et Timothée pour leurs relectures et leurs remarques ainsi qu'à Margaux pour ses précieuses réflections et à François pour ses conseils lors du développement des différents modèles.

Nous voulions aussi remercier Frank et Arnaud pour les connaissances techniques qu'ils ont pu nous apporter à travers leur expertise.

Enfin, un grand merci à nos parents et nos amis pour le soutien moral qu'ils nous ont prodigués, chacun à leur manière, dans la vie de tous les jours.

Table of contents

Nomenclature

Roman letters

$\dot{V}$	Volumetric flow rate [m^3 s^{-1}]
Bi	Biot number [-]
c	Heat capacity [J kg^{-1} K^{-1}]
D	Diameter [m]
F	View factor [-]
h	Convective heat transfer coefficient [W m^{-2} K^{-1}]
I	Current [A]
k	Heat conductivity [W m^{-1} K^{-1}]
L	Length [m]
m	Mass [kg]
Nu	Nusselt number [-]
P	Power [W]
Pr	Prandtl number [-]
Q	Heat source term [W m^{-3}]
q	Heat flux [W m^{-2}]
R	Radius [m]
r	Radial coordinate [m]
Re	Reynolds number [-]
S	Surface [m^2]
T	Temperature [K]
t	Time [s]
u	Velocity [m s^{-1}]
V	Voltage [V]
W	Power [W]
z	Longitudinal coordinate [m]

Greek letters

α	Diffusivity [$\mathrm{m^2\ s^{-1}}$]
ϵ	Emissivity [-]
$\hat{\rho}$	Intrinsic density [$\mathrm{kg\ m^{-3}}$]
μ	Viscosity [Pa s]
ρ	Apparent specific mass [$\mathrm{kg\ m^{-3}}$]
σ	Stephan-Boltzmann constant [$\mathrm{W\ m^{-2}\ K^{-4}}$]

Subscripts

0	Initial
∞	Free stream
$\perp$	Direction perpendicular to the axis of the sample
a	Annular
b	Biomass sample
c	Ceramic
d	Domain
e	Element
ext	Exterior
g	Gas
IC	Insulator coating
int	Interior
m	Mineral wood
N_2	Nitrogen
p	Particle
r	Radial direction
rad	Radiative
s	Sample
st	Stainless steel
w	Wall
z	Longitudinal direction

Abbreviations

FTIR	Fourier Transform InfraRed
GC	Gas Chromatography

Macro-TG	Macro-ThermoGravimetry
PICA	Phenolic Impregnated Carbon Ablator
SPAR	Single PArticle Reactor
SPY	Single particle PYrolysis
TGA	ThermoGravimetric Analysis
TPS	Thermal Protection System

Introduction

Pyrolysis, or thermal degradation under inert atmosphere, is a key phenomenon in many thermochemical processes. Several of these processes are developed for the conversion of biomass, fire prevention, the treatment of plastic waste as well as space vehicles entry into the atmosphere. In this work, we address wood biomass and thermal protection systems (TPS) of spacecrafts.

Biomass is a remarkable renewable source of energy production as it can be stored or transported. Its conversion has already been largely studied and its potential is widely aknowledged. However, the pyrolysis mechanisms have not yet been apprehended with enough depth, at the scale of a centimetric particle. There is a variety of large particle models, but the lack of information on parameters and experimental data makes it difficult to compare and validate them.

The TPS of spacecrafts is based on pyrolysis. As gaseous products form a kind of shield and the remaining solid product absorbs the heat until it is removed by spallation or decomposes through sublimation. A good understanding of this phenomenon is therefore crucial for a reliable prediction of the entry of vehicles into the atmosphere.

Scientists however are developing specific models without cooperating with other fields. In this context, it has been suggested to benchmark the codes from the two scientific communities: biomass conversion and TPS. One of the possible experiments for this comparison would be the pyrolysis of a large piece of wood or TPS material submitted to high heating flux. This setup should be designed in such a way that it can be modeled as a one-dimensional problem.

This work is the first step in the development of this reference experiment. We will start with the description of the pyrolysis phenomenon and a review of the state of the art of the single particle experiments. In the second chapter, we will develop the design of the reactor dimensioned by using the modelisation, later explained in chapter three. Then, we will demonstrate how we adapted the SPY algorithm (Single particle PYrolysis) developed by Blondeau and Jeanmart to validate our experimental apparatus. And finally, we will elaborate the experimental procedures and discuss the outlook for future researches.

Chapter 1

Large particle pyrolysis

In order to compare pyrolysis models from biomass conversion and spacecraft TPS, the first two materials to be studied - based on the experimental apparatus developed in this work - are wood and ablative TPS. In the first section of this chapter, we describe their composition and the products of their degradation after a brief description of pyrolysis. Then, we will review important large single wood particle experiments as well as the state of the art pyrolysis experiments on a particular TPS. Finally, we will give a more in-depth description of "one-dimensional" pyrolysis experiments.

1.1 Pyrolysis

Pyrolysis is the thermal decomposition of carbonaceous material under inert atmosphere[1]. When a particle is subjected to high heating flux in the absence of oxygen, heat is transferred inward and the heated surface starts to decompose into solid and volatile products, classified in three classes: (i) char, the solid residue; (ii) condensable volatiles, water and other organic species called tar[1]; (iii) non-condensable light gases. It creates a pyrolysis front progressing towards the inside depending on the heat transfer such that three different zones can be observed: a virgin zone, the pyrolysis front and a char zone (see Figure 1.1). Volatile products percolate through the porous char zone and can further react through what is called secondary reactions.

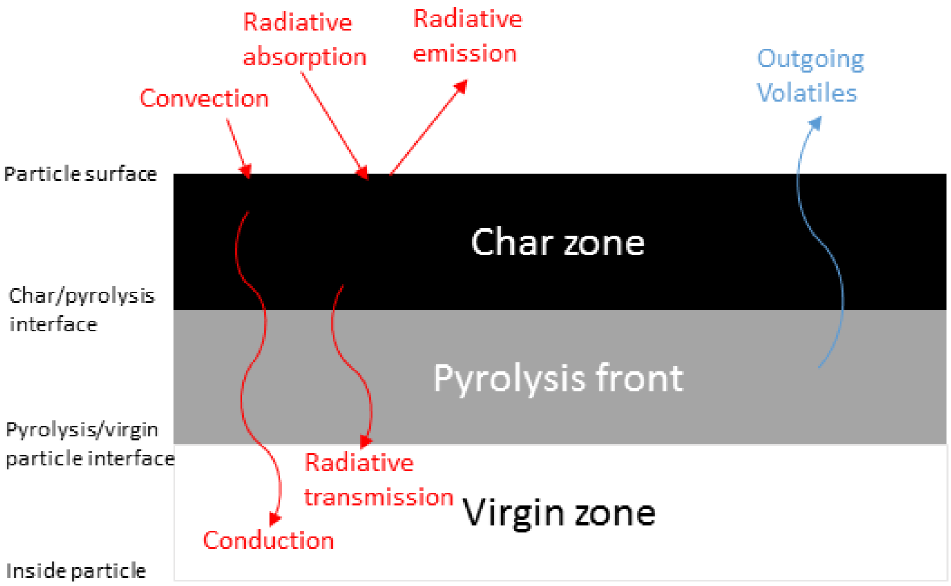

FIGURE 1.1: Representation of the physical phenomena of pyrolysis

Pyrolysis final products properties and yields are highly dependent on the material composition, residence time, heating rate, temperature and size of the particle. Feedstock composition has a great effect on the products elemental composition, while the other parameters have a greater effect on products elemental proportions [2].

1.1.1 Wood composition and pyrolysis

Wood is a lignocellulosic biomass. Lignocellulose is composed of hemicellulose (25-35%), cellulose (40-50%) and lignin (15-20%) [5]. Cellulose is a polymer of glucoses whose chains are linked by hydrogen bonds and assemble to form fibbers called microfibrils. Hemicellulose comprises sugar monomers (xylose, arabionose, glucoses, manoses and galactose). They are bonded to cellulose by hydrogen bonds (see Figure 1.2). Lignin is an amorphous polymer composed of phenylpropane structures providing rigidity and impermeability [6]. It is bonded to cellulose and hemicellulose by ether and ester bonds.

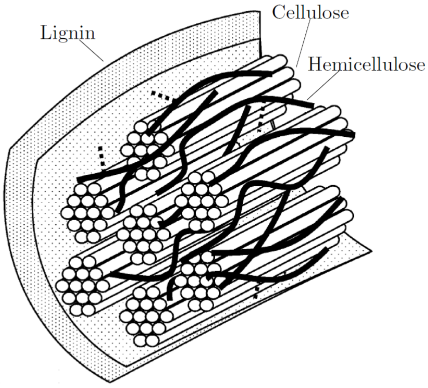

FIGURE 1.2: Schematic representation of the structure of lignocellulose [7]

Next to these polymers, wood is also made of inorganics, extractables and water. The latter is found free, in the liquid or gaseous state within the porous microstructure or as bound water, adsorbed in the form of hydrogen bonds by the hydroxyl groups of cellulose and hemicellulose [8]. The natural matrix of wood biomass differs a lot depending on the species but also between two samples of the same wood. This results in a high variability of its chemical and thermal properties, making it complicated to benchmark existing experiments and models. In the aim of setting up a reference experiment we choose to first focus on beech wood because it is easy to find and one of the most studied species in literature (e.g. [1, 9, 10, 11, 12]). Table 1.1 gives a complete analysis of a beech sample composition.

Wood pyrolysis is somehow dictated by the degradation of hemicellulose, cellulose and lignin respectively between 220 and 300°C, 250 and 350°C and 200 and 500°C [13]. Depending on the need, the conditions will be adapted to create a process giving higher yields and enhanced properties of the desired product. While the lowest char yield is set by the feedstock composition in fixed carbon the highest char yield is obtained for long residence time at low temperature (<400°C). With the

---

[1] Different definitions can be found in literature. For Guell et al. [3], tar are the products that remain liquid at 30°C. For Nunn et al. [4], it is the gaseous species condensing on the reactor's walls or trapped in glass wool downstream at 100°C.

TABLE 1.1: General description of dry beech wood (wt.%) [9, 10, 12]

Proximate analysis		Ultimate analysis		Structural analysis	
Volatile matter	85,3	Carbon	49,8	Cellulose	48
Fixed Carbon	14,3	Hydrogen	6,2	Hemicellulose	28
Ash	0,4	Nitrogen	0,4	Lignin	24
		Oxygen	42,7		

increase of temperature, char production shifts to liquid organic compounds production to reach the highest liquid yields at intermediate temperature (around 500°C). High temperature (>800°C) favours secondary reactions, further devolatilizing char and breaking down the liquid into gases. Higher heating rates enhance the main phase product yield at these given temperatures except for char [14].

1.1.2 Ablative TPS composition and pyrolysis

The second type of material of interest will be TPSs, studied for the entry of spacecrafts into the atmosphere. TPSs protect the payload of the spacecraft thanks to pyrolysis. A state of the art ablative TPS, successfully used in Stardust and Mars Science Laboratory missions has been developed by the Nasa Ames Research Center. Phenolic Impregnated Carbon Ablator (PICA) is a composite material made from a carbon fiber preform (Fiberform, see Figure 1.3) impregnated with phenolic resin. Its insulation properties are due to the high porosity of its carbon preform and the high surface area of phenolic resin [15]. The endothermic decomposition of the organic resin surrounding the carbon fiber substrate absorbs part of the heat. The gaseous products, making there way through the char, cool the leading edge of the ship and create a heat-shielding mechanism. The remaining char continues to absorb heat until it decomposes through sublimation or is removed by spallation [16].

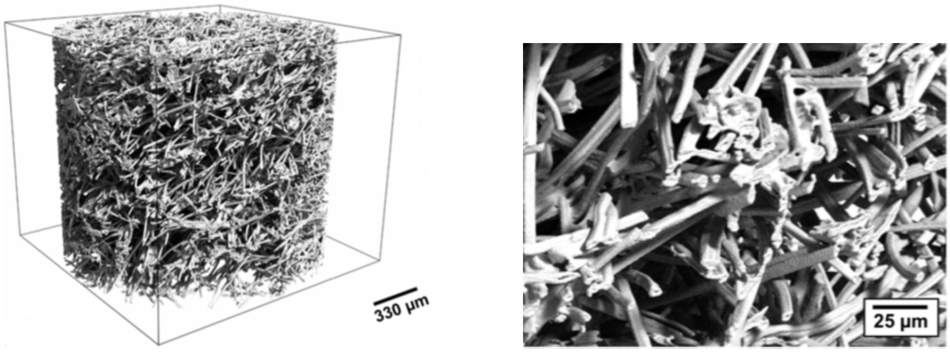

FIGURE 1.3: Micro-tomography ray-tracing rendering of PICA carbon fiber [17]

TPS pyrolysis experiments are conducted at an increasing temperature in order to study real conditions. Studies on the pyrolysis mechanisms of phenolic resins revealed three stages of decomposition at overlapping temperature ranges. At low temperatures (200-550°C), the main products are water, phenol and phenol derivatives. During the second stage (400-800°C), peaks of CO and CH_4 can be observed. Through fusing of the aromatic rings to form a carbonaceous char, H_2 is the dominant product evolving during the third stage (560-1000°C) [18]. More recent studies confirm these trends and outline the effect of heating rate on molar yields designating kinetically controlled processes [18].

1.2 Large single particle pyrolysis reactors

As our experiment is based on large particles, our study on the existing technologies focuses on large single particle reactors. However, thermogravimetric analysis (TGA) should not be neglected as they are useful to determine intrinsic kinetics and as models based on it are frequently used for comparison. TGA, in combination with other analytical devices, is widely used to study materials thermal stability and volatile components. It consists in the measurement of a sample mass loss over time with increase of temperature [19]. Mass is measured continuously using a precision balance with a sample pan inside a furnace with controlled temperature. This method is used at temperatures lower than 1000°C for low heating rate (<100°C/min) and for small particles ($\sim 100 \mu m$). It provides a good insight of the feedstock devolatilization kinetics. But its results are difficult to use in practical application as higher heating rates and/or bigger particle sizes (i.e. with $Bi >> 1$) lead to simultaneously structural and thermo-chemical modifications that are not predictable at low heating rate and for small samples [20, 21]. In TGA experiments, since Biot numbers are small ($Bi << 1$), the sample temperature can be considered equal to the reactor temperature. In order to use these results when that assumption is not valid, heat transfer effect are to be modelled leading to higher uncertainty. Efforts are therefore dedicated to creating experiments giving more accurate results under higher heating rates and/or for larger particles.

1.2.1 Wood biomass pyrolysis reactors

The first major work was presented by Gronli [22]. Based on Chan's apparatus [23], he built a bell-shaped pyrex reactor with a Xenon arc lamp radiatively heating one face of a cylindrical wood particle. The periphery of the sample was insulated in order to obtain a "one-dimensional" heating. His main studies focused on the effect of grain orientation and heating flux (80 kW m^{-2} and 130 kW m^{-2}), highlighting the existence of competing kinetics in the formation of char, tar and gas. Further description of the reactor used will be given in the dedicated section (section 1.3).

Di Blasi et al. [11] kept on with lamp reactor, using infrared lamps for the heating of hardwoods and softwoods samples in a vertical cylindrical quartz reactor (see Figure 1.4). Applying a radiative flux in the range of 28-80 kWm^{-2}, they studied the role of the feedstock variety on temperature, weight loss, product yields and gas composition. It was found that above 40 kWm^{-2} all the species tend to have the same qualitative behavior and process dynamics, that is, when internal heat transfer is controlling the pyrolysis mechanism ($Bi >> 1$). Nevertheless, as chemical composition vary consequently, large quantitative differences were observed concerning pyrolysis temperature (also called peak temperature and defined as the temperature at which pyrolysis terminates and products start to cool down [5]), product yields and devolatilization rates.

The applicability of macro-TGA was studied in Khalil et al. [24] based on the set up developped in Becidan et al. [25]. The results confirm it is suitable for the study of large sample pyrolysis but the disadvantage of the low heating rates for such analysis (here 10°C min^{-1}) still applies.

In their respective thesis, Lu [26] and Bellais [27] describe quite similar single particle reactor. These were built as open platforms so that different analysis could

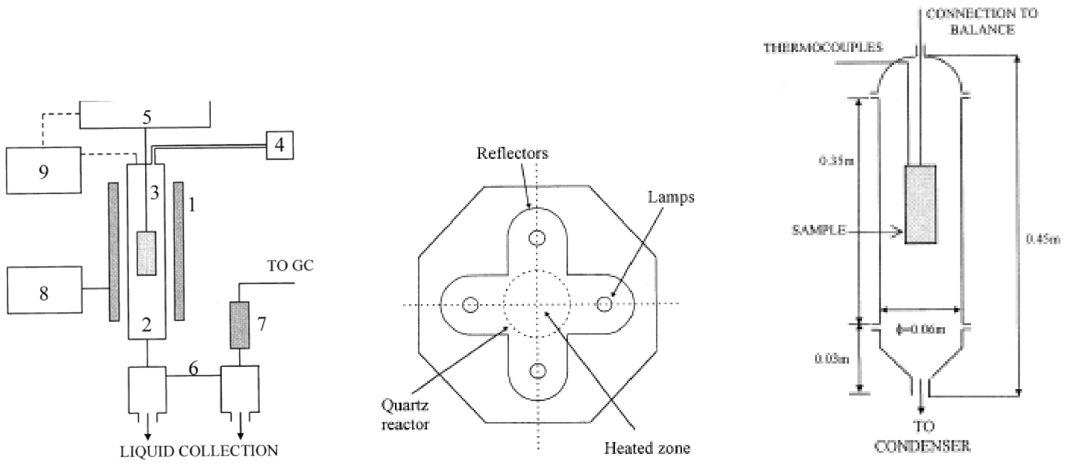

(A) General view (B) Cross section of the heater (C) Quartz reactor

FIGURE 1.4: Schematic representation of Di Blasi et al. [11] pyrolysis system. 1 : radiant heater, 2 : quartz reactor, 3 : sample holder, 4 : flowmeter, 5 : precision balance, 6 : condensers, 7 : filters, 8 : controller, 9 : data acquisition system

be added. Windows openings give optical access to the sample. In Lu, these view ports are placed in the three orthogonal directions. The sample is suspended on a type-B thermocouple connected to a wireless data logger (see Figure 1.5). The data logger, the thermocouple and the particle rest on a balance. An outside pyrometer focused on a surface records changes in surface temperature and shape/size of the sample. Lu et al. [28] studied the effect of particle shape and size on devolatilization showing that spherical particles reacted slowlier than discs and cylinders. This mass loss difference increases with the increase of aspect ratio (D/L) to reach a factor of two or more for diameters bigger than $10mm$.

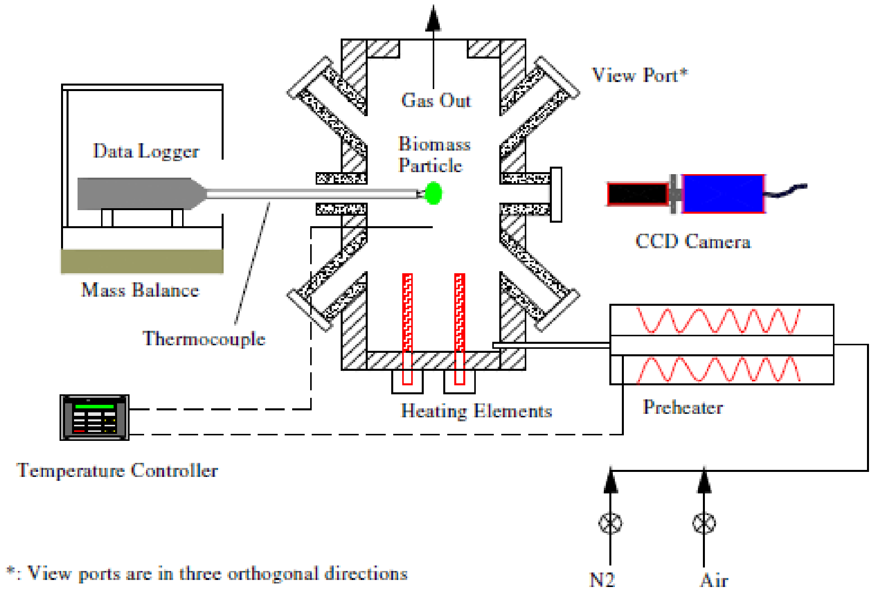

FIGURE 1.5: Schematic representation of the reactor used in Lu [26]

For his studies, Bellais used the Single PArticle Reactor (SPAR) of the KTH (Royal

Institute of Technology, Stockholm, Sweden). Among the five windows openings placed at the sample's height, one was modified to install a capillary tube connected to a mass spectrometer (see Figure 1.6). The particle is dropped on a weighing platform through a retractable air-cooled tube. The reactor is heated by 5 U-shaped vertical heaters at constant temperatures up to 1000°C. The analysis of the temperature is done remotely by Laser-Induced Phosphorescence, using one of the window. Based on temperature, mass loss and dimension changes measurements, he studied the influence of geometry and the type of shrinkage model on the heating rate of the particle. He concluded that shrinkage was strongly dependent on the thermal gradients and the heating rate. Furthermore, it was also concluded that a strong correlation exists between the geometry of the particle and the implementation of shrinkage concerning heating rate.

The SPAR was also used in Davidsson and Pettersson [29], where shrinkage in different directions as function of the conversion is calculated combining results from the balance and measurements from cameras recording in multiple directions. The main observation were the following : (i) longitudinal shrinkage weakly depends on heating rate and begins only after 60% of mass loss; (ii) Maximum radial shrinkage occurs between 500 and 700°C; (iii) tangential shrinkage is maximum at 400°C. Unfortunately, sample used were to small to observe a significant impact of shrinkage on mass loss.

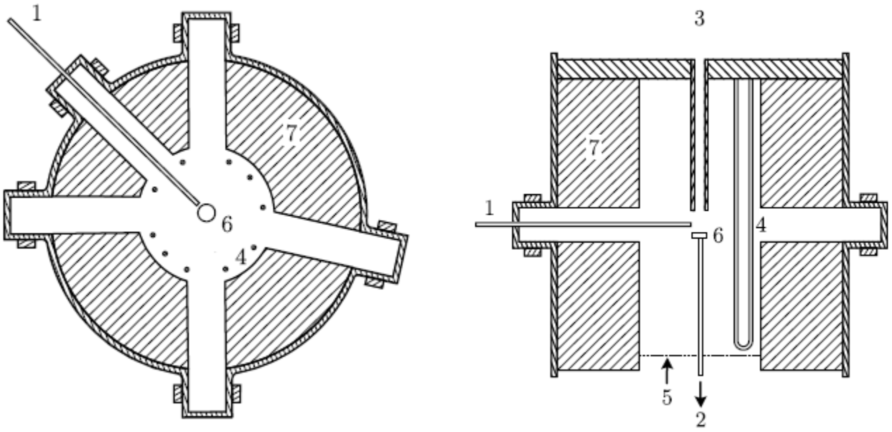

(A) Vertical view (B) Horizontal view

FIGURE 1.6: Schematic representation of the reactor used in Bellais [27], Davidsson and Petterson [29]. 1: capillary, 2: to the balance, 3: insertion tube, 4: heater, 5: pre-heated gas, 6: landing plate, 7: insulating material.

In order to study heat and mass transfer as well as internal pressure during pyrolysis, Park et al. [30] placed spherical samples in a vertical tubular furnace. The choice for spherical particle was motivated by a goal of one-dimensionality, allowing easy modeling. The particular study of the enthalpy of the reactions lead them to the conclusion that an intermediate solid state between virgin wood and final char is to be considered. Unlike suggested in literature, the contribution of the decomposition of secondary tar and lignin to the center temperature peak is small compared to the contribution of exothermic decomposition of that intermediate solid. They also point out the importance of internal pressure generation as it controls mass transfers, impacting heat transfer and residence time of the gases. At relatively high temperature, they observed coincidence between pressure peak and splitting of the char. Further description of this set up is given in section 1.3.

Okekunle et al. used an infrared cylindrical furnace (see Figure 1.7) to investigate intra-particle heat transfer and tar decomposition during pyrolysis of cylindrical woody biomass [31]. Tar was collected in a cold-trap for analysis. Experimental results showed a decrease of total tar yield with the increase of heating rate. Even though both primary formation and intra-particle decomposition of tar increased, the latter became dominant affecting tar yield.

In a second paper, they studied the effect of size and aspect ratio, maintaining the same diameter, on intra-particle tar decomposition [32]. Calculations based on the experiment showed that residence time is related to intra-particle tar decomposition and that the temperature gradient is a significant factor. The thermal conductivity of unpyrolysed wood in the radial direction is known to be lower than along the fibers ([1, 22, 27]). For this reason, a lower aspect ratio, and thus a larger side surface, caused the apparition of a higher temperature gradient. With high temperature gradient, the surface layer temperature was high enough for the intra-particle tar decomposition to further progress while passing through it, thus enhancing tar decomposition. An optimum aspect ratio was then calculated based on thermal conductivity in the grain and radial direction as well as change in residence time.

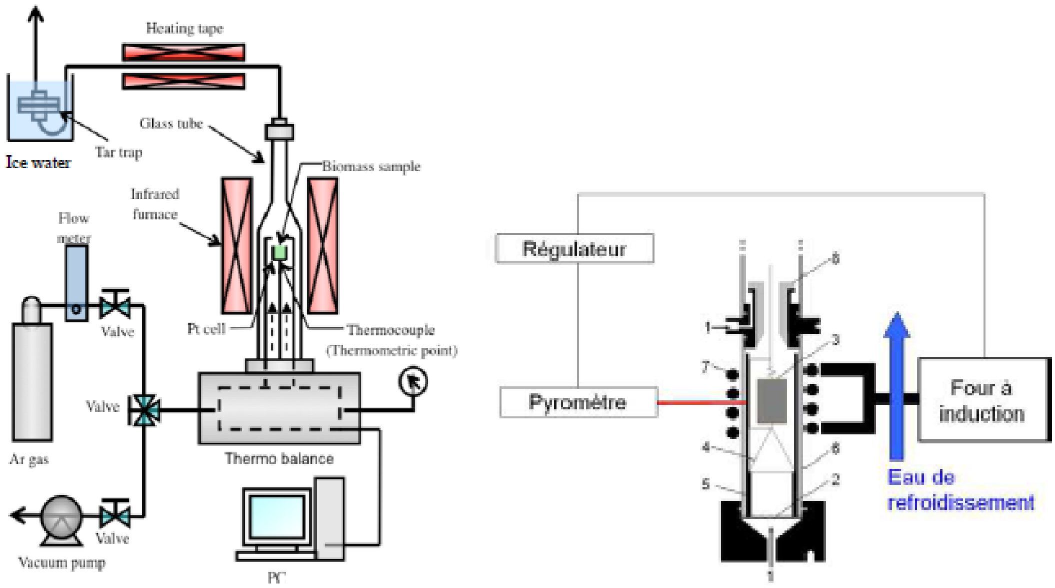

FIGURE 1.7: Schematic representation of the reactor used in Okekunle et al. [31, 32], on the left, and in Gauthier [1], on the right. 1 : Nitrogen inlets, 2 : Inductor, 3 : Inconel pipe heated by induction, 4 : Wood sample, 5 : Metallic sample holder, 6 : Quartz pipes, 7 : Tar collector.

Noticing a lack of experimental data, both chemical and thermal, for the characterization of large sample pyrolysis, the experimental apparatus PYRATES was built for the following study of Gauthier [1]. A 12 kW coil inductor heats up a tube inside which a cylindrical, beechwood particle is placed (see Figure 1.7). The heating rate of the tube is controlled based on the temperature measurement of a pyrometer and can reach 500°C s^{-1}. Measurement of the inside and surface temperature of the sample as well as the temperature of the surrounding gas and of the reactor surface allowed a complete characterization of the heating of the sample. Outgoing tar, water and gas were collected with the main gaseous species being analyzed on line. The analysis of the solid final mass and of the main tar species were also determined such as the accurate and complete set of data collected allows to quasi fully-characterize the pyrolysis of the wood particle.

Recently, Rezaei et al. [33] developed an infrared reactor to study the overall mass loss during pyrolysis. The particle was placed on a plate connected to a digital balance and heated by an infrared 62 kWm^{-2} heater with fused quartz surface. The purge gas flow was pre-heated to avoid temperature gradient inside the reactor. Like in [30], they observed a variable order of mass loss in two temperature zones. Varying the particle size, they also studied the effect of the external fluid temperature on the critical size for the possibility to use a lumped approach. The variation was not found significant as critical size decreased of 1mm each 100°C.

1.2.2 Carbon/phenolic pyrolysis reactors

The first experiments on phenolic carbon ablators were made in the 1960s with TGA and gas chromatography (GC) at heating rates and temperatures ranging from 3-60°C min^{-1} and 350-850°C respectively [34, 35]. In the 90s, similar experiments were made by Trick and Saliba, adding Fourier Transform Infrared Spectroscopy (FTIR) analysis of the pyrolyzed particle [36, 37]. Milos et al. based their study on data collected from planetary probes such as the Mars Path Finder or the Galileo probe [38, 39, 40]. Analyzes determined radiative heat flux and heating rate of the order of 120 W cm^{-2} and 30 kW cm^{-2} respectively on the TPS of these probes made of silicone-impregnated reusable ceramic ablator or carbon phenolic heatshield for example. The models they have built are still used for the dimensioning of today's NASA's PICA heat shields [41].

However, limited data were available on the pyrolysis of PICA. For the latter reason, Wong et al. [42] used the following protocol combining batch reactions with mass spectrometry and GC in parallel with mass balance to report accurate quantitative species production. That is, they increased sample temperature by 50°C steps keeping the target temperature for 1h under vacuum. Between each temperature step, the reactor was quenched to stop the reaction. The sample could be weighted and all condensed products could be collected from the wall and analyzed as well as the gas collected during the reaction. The reactor was made of a stainless steel assembly and a quartz tube directly connected to the gas extraction and placed inside a ceramic furnace heated by nichrome heating wires. The PICA sample was loaded in the quartz tube and the outflow of its volatile products to the condenser was ensured by temperature gradients, limiting secondary reactions.

Until then, the kinetic at higher rate than possible with TGA was extrapolated. The effective properties were averaged between virgin and fully charred state leading to erroneous predictions of the decomposition, as explained in the introduction of this section. That is why Bessire and Minton [18] studied the decomposition of PICA with temperature and heating rate under vacuum atmosphere. To do so, they used what is called "Joule heating". That is, they passed electric current trough the sample itself applying a voltage at its extremities (see Figure 1.8). Doing so, the carbon substrate was resistively heated so that the phenolic matrix of the material was pyrolysed at linear heating rates from 3 to 25°C s^{-1}. This experiment allowed to highlight the non equilibrium of the pyrolysis process as the obtained data show the relative importance of competitive mechanisms depending on heating rate.

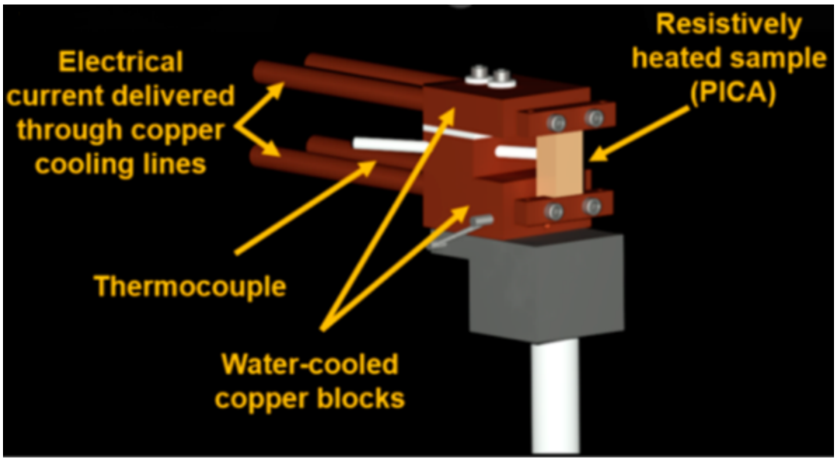

FIGURE 1.8: Sample holder for resistive heating of PICA samples in Bessire and Minton [18].

1.2.3 Conclusion

Many experiments have been carried out to validate, create, modify or compare some of the existing models (Table 1.2 provides an overview of the aforementioned apparatus). However, the operating conditions and/or the results are rarely fully described. This, linked to the variability of the feedstock used, does not allow a comparison between these different experiments and therefore does not allow an objective comparison on a larger scale of the different models.

Furthermore, a deep understanding of the influencing phenomena is necessary for the development of reliable models. These observations underline the importance of creating an experience allowing to investigate a large panel of materials and operating conditions, and thus acquire precise experimental data, useful for modelling and comparison. By reducing the number of variables and simplifying the problem, the development of a one-dimensional experiment could contribute to the objective. Additionally, the study of different materials such as wood or TPS could help join forces of two scientific fields working on their side.

TABLE 1.2: Overview of the characteristics of different experimental setups used to study the pyrolysis of large particles (adapted from [1])

t_{res} : Is the residence time of pyrolytic vapour characterized?
$\dot{T}$: Is the heating rate controlled?
q_{ext} : Is the external heat flux characterized?
T_{in} : Are internal profiles measured?
$\dot{m}$: Is the sample mass loss measured online?

Ref	Reactor	Feedstock	Shape & Size	Purge gas	t_{res}	Temperature	$\dot{T}$	q_{ext}	T_{in}	$\dot{m}$
Gronli [22]	Xenon arc lamp	Birch, spruce and pine	Cylinder Ø20x30	N2 4,4Nl/min	<1s	up to 900°C	V	80&130kW/m^2	V	X
Di Blasi [11]	Infrared lamps	Beech, chestnut, douglas fir, redwood & pine	Cylinder Ø40x40	N2 12,5l/s	6s	up to 700°C	V	$28-80kW/m^2$	X	V
Lu [26]	SPAR	Poplar	Sphere, disc & cylinder Ø3 to 12	N2 700°C	>1s	up to 1000°C	V	X	V	V
Bellais [27]	SPAR	Pine, birch	Cube l = 1, 2 & 5 Cylinder Ø5x5 & Ø10x15	N2	X	300 to 800°C	V	X	X	V
Khalil [24]	Macro-TG	Poplar pannonia, hongarian poplar & ailanthus altissima	Pieces 20 to 40	N2	X	up to 900°C	10°C/min	X	X	V
Park [30]	Carbolite furnace	Maple	Sphere Ø25,4	Ar 0,21g/s	X	365-907°C	X	X	V	V
Okekunle [31]	Infrared lamp	Cypress	Cylinder Ø8x2;5;9	Ar	X	up to 700°C	5, 10 & 30°C/s	X	V	V
Gauthier [1]	PYRATES	Beech	Cylinder Ø20x30	N2 2-4Nl/min	<1s	450-1050°C	V	65kW/m^2	V	X
Rezaei [33]	Infrared lamp	Pine chips and pellet	w = 1 to 5 l = 5 to 25	N2 3NL/min 300°C	X	300-500°C	unknown	62kW/m^2	X	V
Wong [42]	Ceramic furnace	PICA	100 mg $\sim 360mm^3$	Vacuum	X	47-977°C	X	X	V	X
Bessire [18]	Joule heating	PICA	25x9x7	Vacuum	$\sim 10^{-2}s$	100-1200°C	3-25°C/s	X	V	X

1.3 One-dimensional pyrolysis experiments

Of all the literature reviewed, only two experiments have been dimensioned in such a way that they can easily be considered one-dimensional when modeled. An in-depth description as well as the analysis of the one-dimensionality of the first set-up is given in this section.

1.3.1 Xenon arc lamp cylindrical reactor

As part of his PhD thesis [22], Gronli developed a single-particle glass tube reactor (see Figure 1.9) whose purpose was to study the influence of heating conditions, grain orientation and wood species on the product yields of centimetre-scale samples pyrolysis. The cylindrical particle of 20 mm diameter and 30 mm length is radiatively heated on one face using a 1100 Watt Xenon arc lamp at two different heat fluxes (80 kWm^{-2} and 130 kWm^{-2}). This uniform and constant radiant heat flux is focused on the pellet surface using the lamp's housing reflector and varying the distance with the reactor.

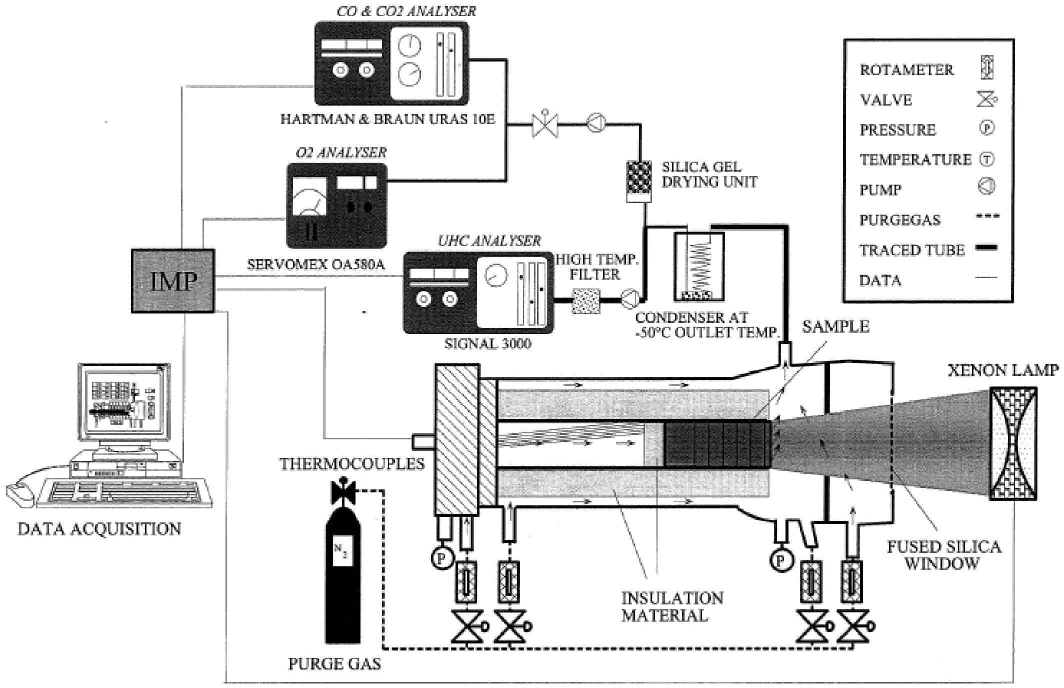

FIGURE 1.9: Schematic diagram of the Xenon Arc Lamp single-particle pyrolysis reactor [22]

The reactor features two main parts: a front window and the sample holder. The fused silica front window provides a maximum radiation transmission. The sample is fitted into a glass tube placed inside the aluminium sleeve closing the back of the reactor. The exposed face of the sample coincides with the end of the tube which is insulated by 20 mm of glass wool (Fiberfrax) to ensure one-dimensional heating. A Nitrogen flow is used as purge gas to ensure an inert atmosphere and sweep out the volatiles limiting back-mixing. Two ports are located close to the window, three others on the back of the reactor and the last one purges the glass tube from the back to the sample. A small pressure gradient is induced to purge volatiles toward the outlet. The outflow is split to hydrocarbon, CO/CO_2 and O_2 analyzers after passing by a cold trap and a filter.Room temperature, condenser internal and outlet temperatures, sample surface and internal temperatures were measured using type-K thermocouples. The ones placed inside the sample were positioned in the center, every 4mm along the axis.

Gronli faced several experimental problems causing uncertainties in measurements and thus in the one-dimensionality of its experiment. The Xenon arc lamp intensity was not stable and the position of the focus point could sometimes vary during the experiment; therefore, the highest intensity was not at the center of the sample surface. This, taking into account that the intensity of the light beam was 8% lower at the edges of the sample, shows a limitation of this device. Furthermore, the sample outer face did not fit perfectly with the surrounding glass tube; Consequently, the insulation was not perfect and volatiles could flow in spaces between the sample and the glass tube. They also had trouble drilling the holes for the positioning of the thermocouples which made the positioning in the plots considered as approximate. All these problems impacted the uniformity of the heating as well as the precision of their measurement, making some of the results difficult to analyze . Figure 1.10 gives an indication of the reproducibility of the experiments with the temperature histories of three identical experiments at low heating rate on spruce.

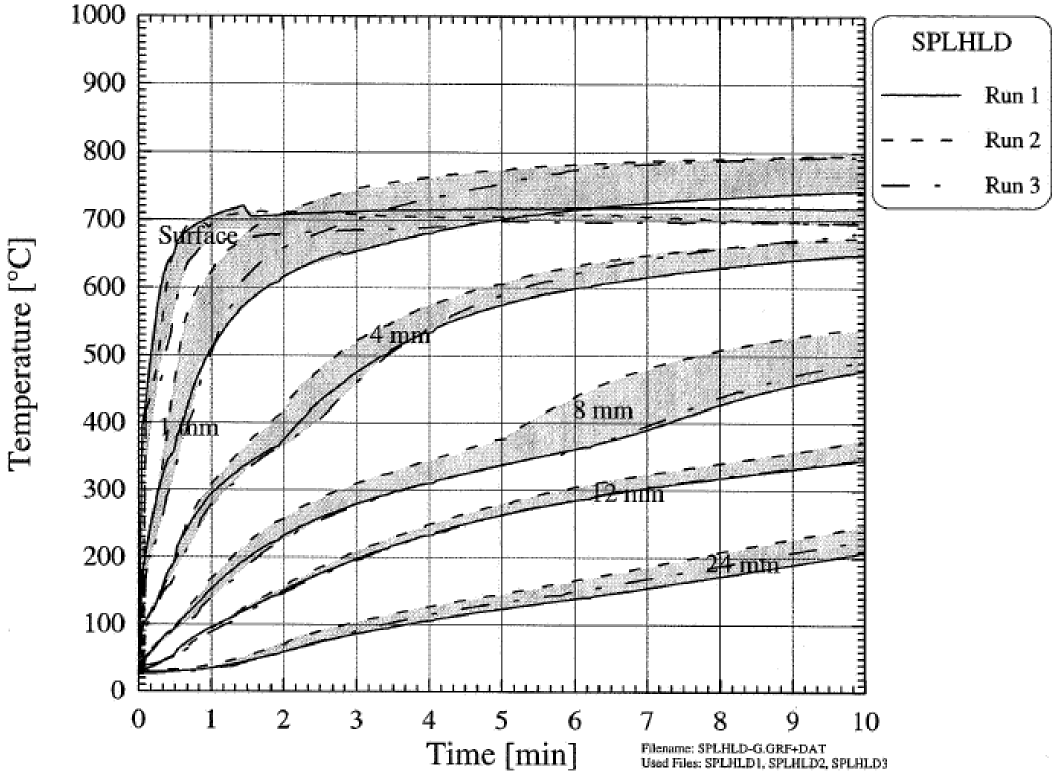

FIGURE 1.10: Temperature histories of three identical experiments [22]

1.3.2 Vertical tube furnace reactor

For the purpose of analyzing heat and mass transfer during wood pyrolysis, Park et al. [30] developed the experimental apparatus shown in Figure 1.11. They pyrolyzed 25,4 mm diameter maple wood spheres choosing that shape to maintain one-dimensionality and thus facilitate modelisation. The previously dried wood was placed in the middle of the vertical tubular furnace, hanging from a precision balance (located above the furnace) continuously measuring mass loss. It was positioned in such fashion that grain wood direction would be horizontal. The furnace consisted of a mullite tube (length of 558 mm and diameter of 106 mm) and two electric heaters (length of 300 mm), with a temperature controller. The outside surfaces were insulated and covered with a stainless steel layer.

Furnace temperature was monitored using eight thermocouples located on the tube inside surface and one on the upper and lower insulating caps as shown on the schematic. A type-K thermocouple (⌀0,2 mm) was glued in a tinny slot cut in the surface of the sphere to measure the sample surface temperature. The inner temperature of the sample was measured using two type-K thermocouples (⌀0,25mm) inserted in the centre ($r = 0$) and half-way between the center and the surface thermocouple ($r = r_0/2$). The holes were drilled in the radial wood fiber direction. To ensure inert atmosphere and the outflow of pyrolysis volatile products, the furnace was purged by a 0.21 g s^{-1} Argon flow. The gas temperature near the sample was measured to calculate the convective heat losses.

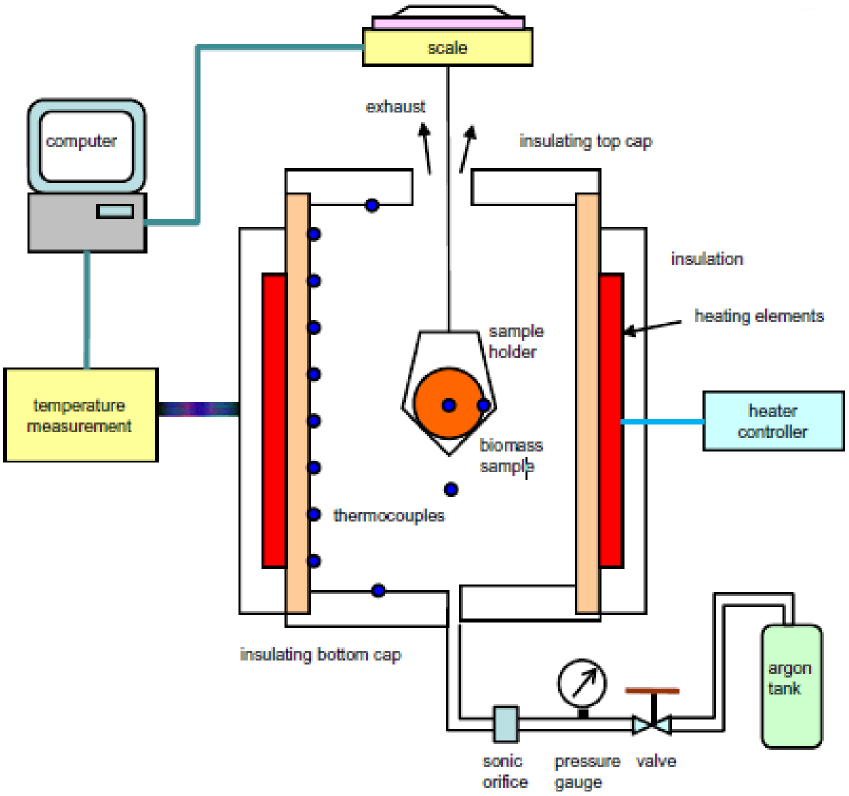

FIGURE 1.11: Schematic of Park et al. one-dimensional pyrolysis apparatus [30]

Chapter 2

General design of the reactor

After reviewing the literature, the next main step is the design of a reactor pyrolysing a large sample at high heating flux in such a way that it can be assumed as one-dimensional. In this work, we focus on the shape and size of the apparatus, the radiative heating of the sample under inert atmosphere as well as the control and measurement of the related parameters. This chapter will describe the final design of the device, based on an iterative work between its development and the parametric study of its characteristics. The calculation and modelisation are presented in the next chapter.

The resulting reactor (Figure 2.1) consists in a cylindrical sample, heated on one face and insulated on the others. This assembly is hanging from a balance. A cylindrical casing internally insulated closes the reactor and a N_2 flow flushes the inside.

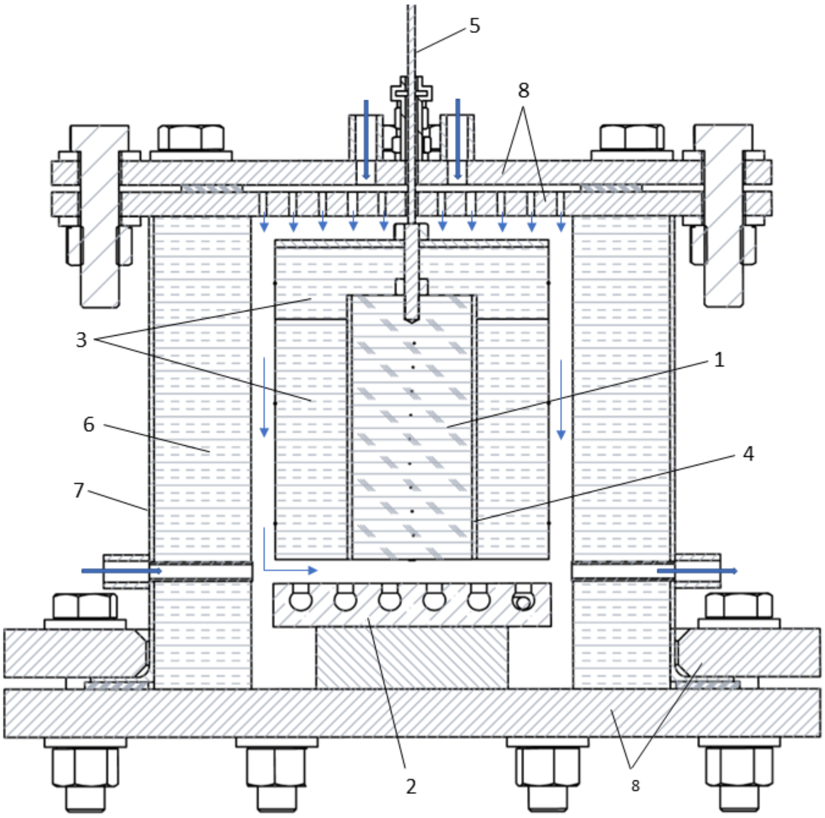

FIGURE 2.1: Overview of the pyrolysis reactor. 1: Sample; 2: Heating source; 3: Sample insulation; 4: Insulation fixing tube; 5: Hanging cable connecting to balance; 6: External insulation; 7: Casing; 8: Clamp.

We will start this chapter by explaining the constraints related to the goal of one-dimensionality. Later on, the size and geometry will be described and justified, along with the material used. It will be followed by the description of the heating source. Taken together, these last two sections are critical to achieve the aforementioned objectives within the related constraints. Afterwards, we will describe the system for weighing the sample. Finally, we will tackle the piping and the instrumentation necessary for the operation of the apparatus. The complete drawings of the reactor containing cut views and depicting all the dimensions are provided in Appendix A.

2.1 Constraints

We chose a cylindrical shaped sample with one of its bases undergoing an external heat flux. This configuration already allows us to have an axisymmetric problem and thus remove the angular dimension by keeping the radial and longitudinal dimensions.

In order to be able to make the assumption of the one-dimensionality of our experiment, we have to minimize the heat transfers in the radial direction. This can be done in three different ways:

- By decreasing the lateral heat losses to the surrounding environment;
- By decreasing the diffusivity in the radial direction;
- By homogenizing the external heat flux.

During the experiment, the sample will be weighted. For our mass evolution to be as close as possible that in the one-dimensional case, we need to homogenize the mass flow rates over the surface of the sample which is directly linked to the homogenization of the temperature in the radial direction. Finally, the particle has to be long enough to assume a semi-infinite problem. Our design will thus attempt to fulfill these characteristics.

2.2 Geometry and material

To mitigate the radial heat losses with the surrounding environment, the faces of the sample that are not supposed to undergo the external heat flux should be insulated. The material used for this purpose is the *ProRox SL 980* mineral wool of 30 mm thickness (see section 3.2) from *Rockwool*®, withstanding high temperatures. Above the sample, the wool is simply laid on its upper face. As the wool cannot be fixed directly around the sample, the latter will be inserted in a thin stainless steel (AISI304 steel of 2 mm thickness) tube. The wool will be fixed with a noncombustible glue (*Rockwool*® Conlit) to the steel tube. It is this assembly, together with the fixing gear that is going to be weighted by the balance.

The diameter of the sample (50 mm, see Section 3.2 for the dimensioning) was chosen sufficiently large to neglect the radial losses in the central region and consider the problem as unidirectional. The length also had to be large enough (100 mm) so that for the duration of the experiment the heat cannot diffuse until the top of the sample and the problem can thus be considered as semi-infinite. To avoid the problem of space between the sample and the surrounding material faced by Gronli (see section 1.3) the inner diameter of the steel tube should be slightly smaller than the diameter of the sample and their coaxiality must be accurate.

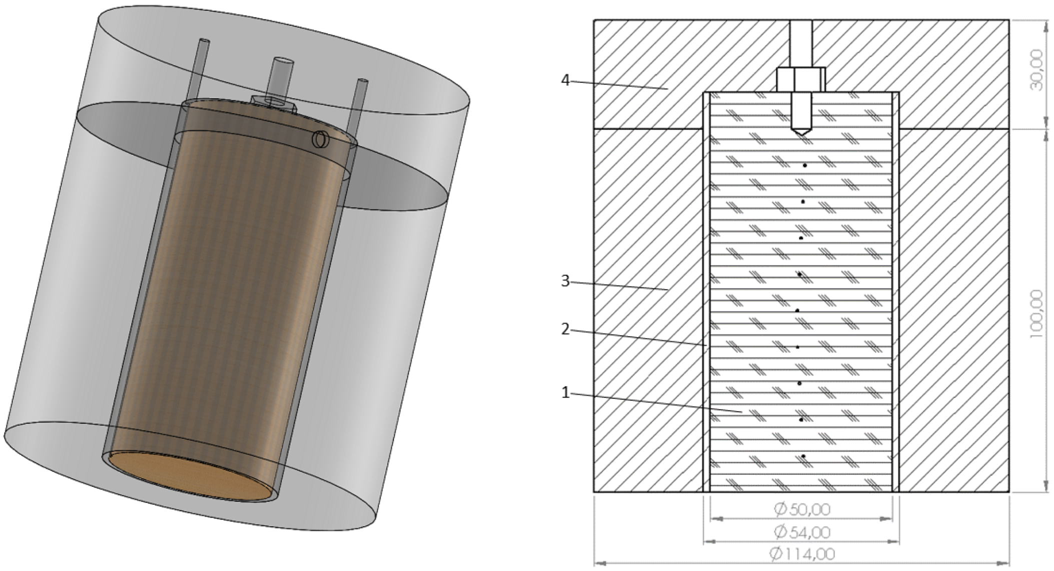

FIGURE 2.2: 3D drawing and sectional view of the sample and its insulation. 1 : Sample; 2 : Steel tube; 3 : Surrounding insulation; 4 : Upper insulation

The casing of the reactor is made of stainless steel. It is composed of an external wall of 215mm inner diameter, internally insulated with wool and sealed by clamps. The diameter was determined in order to use standard size clamps while having a space of 10 mm between the wool insulating the sample and the external wool. That space was necessary to avoid friction interfering with the weighing and its size was selected in order to obtain a low Reynolds number for the Nitrogen flow in that region (Re = 42, see Section 3.1).

2.3 Heating source

The main specifications for the heating source were determined in order to reach a high and uniform temperature (800 °C) in quite a short amount of time (around 2 min). In consultation with *Kamenev bvba*, a specialised manufacturer, we have developed the following.

It is composed of a coil of diameter 7.5 mm made of a 12 m resistive wire of section 0,16 mm^2 and linear resistance 8,86 Ωm^{-1}. The maximum reachable temperature on the wire is 1200°C. To obtain a uniform heating surface, the coil is inserted in a circular ceramic slab in which 10 grooves have been drilled (see Figure 2.3). Part of the wire length is used to connect it to the power source. Ceramic was chosen for its high conductivity and emissivity enabling rapid and uniform heating of the slab and a high heat radiation. This solution allows us to easily achieve the desired heat flux.

The distance between the sample and the ceramic slab as well as its diameter were dimensioned (as explained in Section 3.2) to ensure uniformity of the sample surface heating and thus the one-dimensionality of the heating. As a result, the diameter was defined as equal to the outer diameter of the wool surrounding the sample; there is a 1cm distance between the slab and the assembly formed by the sample and its insulation. At the standard voltage 230V, the manufactured resistance has a power of 500W. Experiments need to be done in order to obtain the different thermal characteristics of the heating source (heating rates, temperature distribution,...). However, in Chapter 4, the heating of the slab will be modelised adapting the voltage to obtain the desired heat flux.

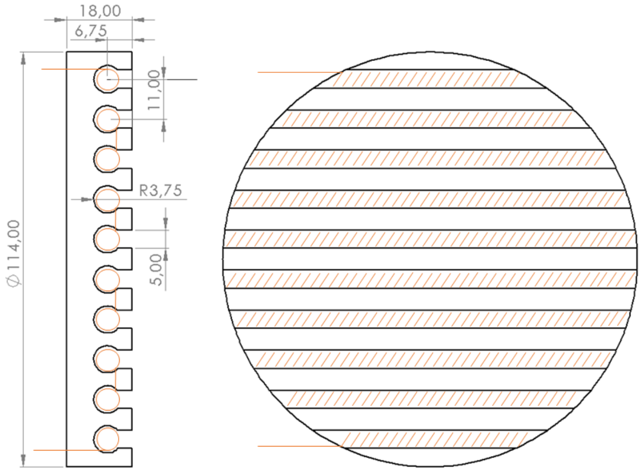

FIGURE 2.3: Ceramic slab for the heating source. The coil-shaped wire resistance is represented in orange.

2.4 Weighing apparatus and fixing of the sample

In order to develop the understanding of the different phenomena involved in the pyrolysis and as no gas analysis will be carried out in the first instance, the apparatus enables continuous measurement of the sample mass. This way, we do not only calculate the char yield but we are able to easily establish a precise mass profile.

The solution that appeared to be the most simple and precise regarding the high inside temperature is to hang the sample to a weighing balance placed on a fixed plane above the reactor (see Figure 2.4a). The sample will be suspended on its upper face by a stainless steel cable (⌀3mm) fixed by a stainless steel M51 screw (see Figure 2.4b). On the other side, the cable will be hooked to the underside of the weighing balance through a hole drilled in the plate supporting it.

A nut ensures not to screw too deep into the sample. It serves as a marker to vertically position the assemble at 1 cm from the heating source. The steel tube will be fixed to the sample using a tap screw. The upper face insulation is pressed with a stainless steel disk compressing it, using a nut, to avoid gas flowing at the interface between the two wool surfaces. As the contact and friction of the hanging cable with other components must be avoided, no bulkhead or joint can be used for sealing, passing through the outer clamp. The clamps will thus be drilled with a diameter slightly bigger than that of the cable (⌀5mm). To ensure the outgoing of all the volatile products through the outlet and avoid oxygen to enter the reactor, a small nitrogen flux will be injected through the outer clamp (see Figure 2.4c) around the cable forming a gas seal [43].

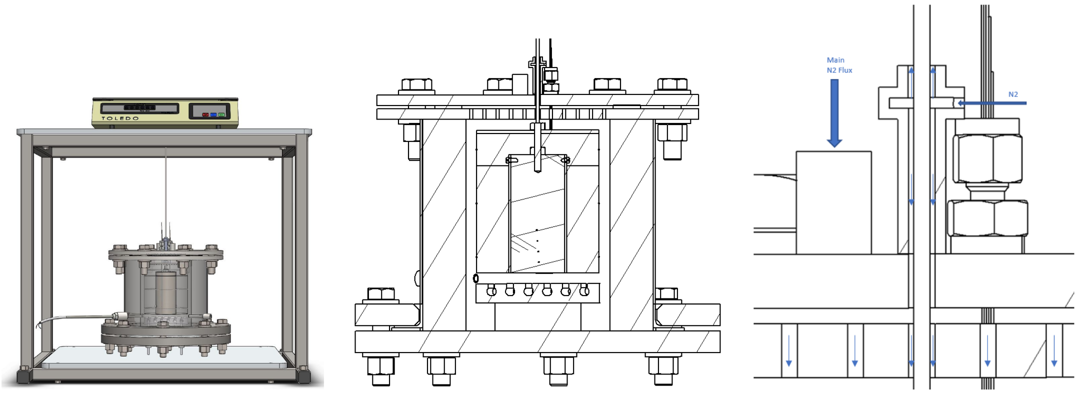

(A) Overall installation (B) Reactor's level cut (C) Gas seal

FIGURE 2.4: Weighing of the sample

Finally, the choice of the balance was made in function of the sample mass and the overall mass hanging at the balance (sample, isolation, fixing gear). For the sample dimension given in Section 2.2, TPS and wood mass order range from 10 to 100 g and the total hanging mass should not exceed 3500 g. Therefore, a precision balance similar to the *Sartorius® ENTRIS4202-1S* with a maximum capacity of $4200g$ and an accuracy of $10mg$ will be suitable.

2.5 Piping and instrumentation

Several values need to be measured and controlled such that the pyrolysis experiment can be properly characterized. Since we are not dealing with tar and gas analysis, only the temperature, pressure and flow measurements as well as their control will be developed here. This will result in the P&ID given at the end of this section (Figure 2.6).

2.5.1 Temperature measurement and control

Nitrogen and exhaust gas temperatures will be measured at the inlets and outlets of the reactor. To determine the pyrolysis temperature profiles, 10 type-K 0,5mm thermocouples will be inserted into radial holes in the sample. Their tips will be reaching the central axis every centimeter with the first one placed on the heated surface. The holes should be drilled using a guide to ensure an accurate angle and thus reach the center. For example, we could use a flat ring with sample diameter perforated and welded to a guide tube.

In addition, slots will have to be cut longitudinally so that the sample with the thermocouples can be inserted into the steel tube (see Figure 2.5a). Their cables will then have to be pulled through the upper insulation of the sample and the compression disk through two holes (see Figure 2.5b) that can be filled on the disc level with a modeling clay if necessary. The passage through the outer clamp is made by means of two multiple transducers sealing glands. To avoid interference in the mass weighing, a loop or a fold will have to made with the thermocouples in the space between the disk and the clamp. This way, the assembly will not be pulled upwards.

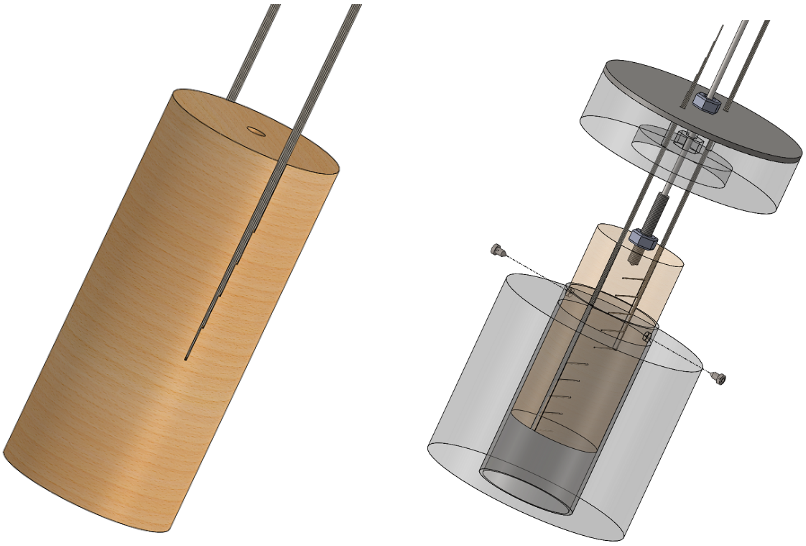

(A) Drilled sampled (B) Exploded view

FIGURE 2.5: Drawing of the thermocouples assembly for the measurement of the temperature profiles in the centre of the sample

A temperature probe will also be used to control the temperature of the heating plate using a solid state relay controlled by an acquisition system or a single-channel temperature regulator.

2.5.2 Nitrogen flow

The N_2 flow ensures an inert atmosphere inside the reactor and purges the volatile products from the reactor. It is injected uniformly through holes drilled in the upper clamp. To ensure that the volatiles between the sample and the heating plate are swept out, a lower flow is inserted laterally at that height. The gas outlet is diametrically opposed to this latter N_2 inlet (see Figure 2.6). A small pressure gradient is imposed to ensure the outflow of the volatiles. It is controlled using a pressure regulator upstream of the upper inlets. The outgoing gas passes through an O2 analyser to verify whether the atmosphere is well inert.

The N_2 flow is an important characteristic for the analysis of the gas products. When an analysis is performed, back-mixing must be avoided by ensuring a laminar flow, whose speed is chosen depending on the desired volatile residence time in the reactor, boosting or not secondary reactions. Since we mainly focus on the heating, this is outside of the scope of this work. Consequently, we fixed a residence time of about 5s with a total flow of 7,9 Nl min^{-1} distributed proportionally to the reactor volume between the upper inlets (6,5 Nl min^{-1}) and the lateral inlet (1,4Nl min^{-1}). These two flows will be delivered by two valves controlled using thermal mass flowmeters. The N_2 flow inserted at the cable level should still be determined. As it should not be really high and changed a lot, we chose to measure it with a rotameter and to regulate it with a manual valve.

To allow the verification of the oxygen concentration, an O_2 analyser is placed at the outlet of the reactor. The atmosphere is considered inert when the O_2 becomes lower than 0,1%

2.5.3 Piping and instrumentation diagram

The following diagram (Figure 2.6) represents the overall piping, measurement and control of the apparatus and its functioning. An enlarged version of the diagram can be found in the Appendix B together with the attribute list.

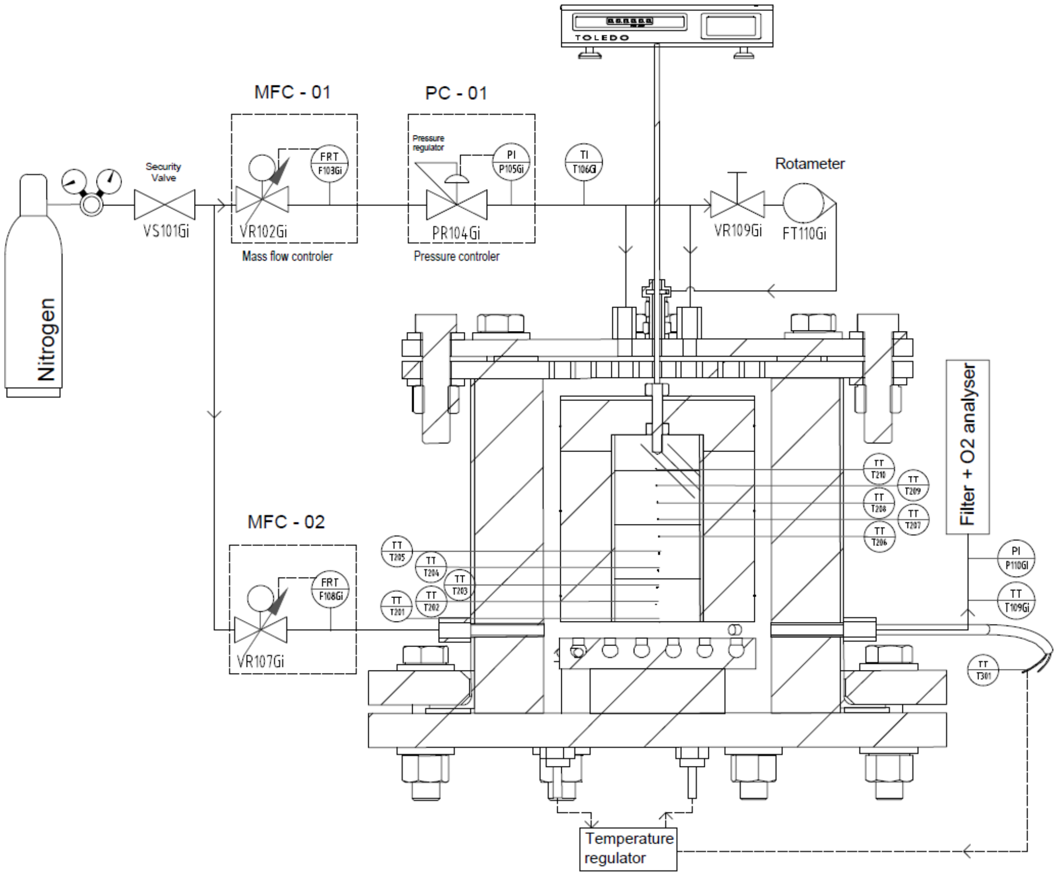

FIGURE 2.6: Piping and instrumentation diagram of the apparatus

Chapter 3

Dimensioning of the reactor

In this chapter we present the method used to determine the four following dimensions:

- The thickness of the insulating layer ;
- The diameter of the heating source ;
- The distance between the sample and the heating source ;
- The diameter of the sample.

These dimensions are critical for our design because making them vary has an impact on the one-dimensionality of our experiment.

3.1 Physical model

A two-dimensional model of the heat transfer in the assembly formed by the sample, the stainless steel and the insulating layer is assumed here. Since this is a preliminary design, we will not consider the effects of pyrolysis. This model is therefore only valid for sample temperatures below 200°C, temperature at which the pyrolysis first stage of the wood [9] and the PICA [16] occurs on average. The main features of this model are:

- Conductive heat transfers inside the assembly ;
- Convective and radiative heat transfer on the side of the assembly facing the heating source ;
- Convective and radiative heat transfer on the periphery of the insulating layer.

This leads us to the following energy conservation equation in cylindrical coordinates:

$$\rho c \frac{\partial T}{\partial t} = \frac{1}{r}\frac{\partial}{\partial r}\left(kr\frac{\partial T}{\partial r}\right) + k\frac{\partial^2 T}{\partial z^2} \tag{3.1}$$

with ρ, c, k and T the local density, specific heat, conductivity and temperature. The variables t, r and z respectively correspond to the time and radial and longitudinal coordinates. The considered problem is assumed axisymmetric.
The boundary conditions are:

$$k\frac{\partial T}{\partial r}(r = R_d, z) = h_z(T_{N_2} - T) + q_{rad}(R_d, z) \tag{3.2}$$

$$k\frac{\partial T}{\partial z}(r, z = L_d) = h_\perp(r)(T_{N_2} - T) + q_{rad}(r, L_d) \tag{3.3}$$

$$\frac{\partial T}{\partial z}(r, z = 0) = 0 \tag{3.4}$$

with h_z and $h_\perp$ the convective heat transfer in the direction parallel and perpendicular to the axis, R_d and L_d the radius and the length of the domain and q_{rad} the radiative heat flux. The spatial derivatives of these equations are discretized with a second order finite difference scheme and the time integration is performed with an explicit Euler scheme.

3.1.1 Physical parameters

The purpose of this model is to approximate the heat transfers in the particle in order to determine the dimensions mentioned above. The following assumptions have been made to simplify the problem and determine the physical parameters accordingly.

Firstly, all the materials are considered as isotropic. This assumption is very close to reality for wool and the stainless steel since the fibers of these materials do not have a preferential order. However, wood and PICA are both anisotropic materials and their heat conductivity is very different whether it occurs along the fibers or in the perpendicular direction. The conductivity of PICA in the longitudinal direction is about 2.4 times higher than in the radial direction [44]. For beech, this ratio is around 2 between 20°C and 400°C (value obtained with the model of Kollmann and Cote [45]). Yet, in order to simplify the model and due to a lack of values in the literature for the exact difference of conductivity in the parallel and transverse direction for the PICA, we set the same conductivity in all the directions.

Secondly, we consider that the thermal properties of the materials remain constant. Since we stop the simulation before the first stage of the pyrolysis, this is a valid assumption for the emissivity and the intrinsic density of the elements. This simplification can also be considered valid for the heat capacity of the wool and the stainless steel AISI 304, as it hardly changes with temperature. Nevertheless, the heat capacity of biomass and PICA and the conductivity of all the materials are temperature dependent.

The values of the temperature dependent parameters were obtained by computing their average value between 20°C and 200°C. Regarding biomass, we used the models of Kollmann and Cote for the conductivity and Blondeau and Jeanmart [46] for the specific heat. The heat capacity and the conductivity of PICA were computed with the values found in [44] as for the conductivity of stainless steel and wool we used the values found in Chu and Ho [47] and in *Rockwool® Technical Insulation*'s catalog respectively. The values of these physical parameters are given in Table 3.1.

The diffusivity computed for the different materials is presented in the Figure 3.1. There is an average thermal diffusivity error of 10% for the insulating layer, 4% for the stainless steel and the PICA, 25% for the wood in its longitudinal direction and 49% in its transverse direction. The error for wood is much larger than for the other materials because we do not take its anisotropy into account. The error for

---

[1] The physical parameters of the mineral wool are given by *Rockwool® Technical Insulation* for the product ProRox SL 980 with white enamel coating.

TABLE 3.1: Apparent density, heat capacity, thermal conductivity and emissivity of biomass, PICA, AISI 304 and insulating layer and emissivity of ceramic.

Material	ρ [kg m^{-3}]	c [J kg^{-1} K^{-1}]	k [W m^{-1} K^{-1}]	ϵ [-]
Biomass	710 [48]	1646	0.26	0.94 [49]
PICA	280 [50]	1500	0.28	0.91 [44]
Stainless steel	8000 [51]	500 [52]	16.3	0.4 [53]
Insulating layer	145	840	0.047	0.91[1]
Ceramic				0.9 [53]

PICA, should be greater too for the same reason, but the values found in the different studies do not consider anisotropy.

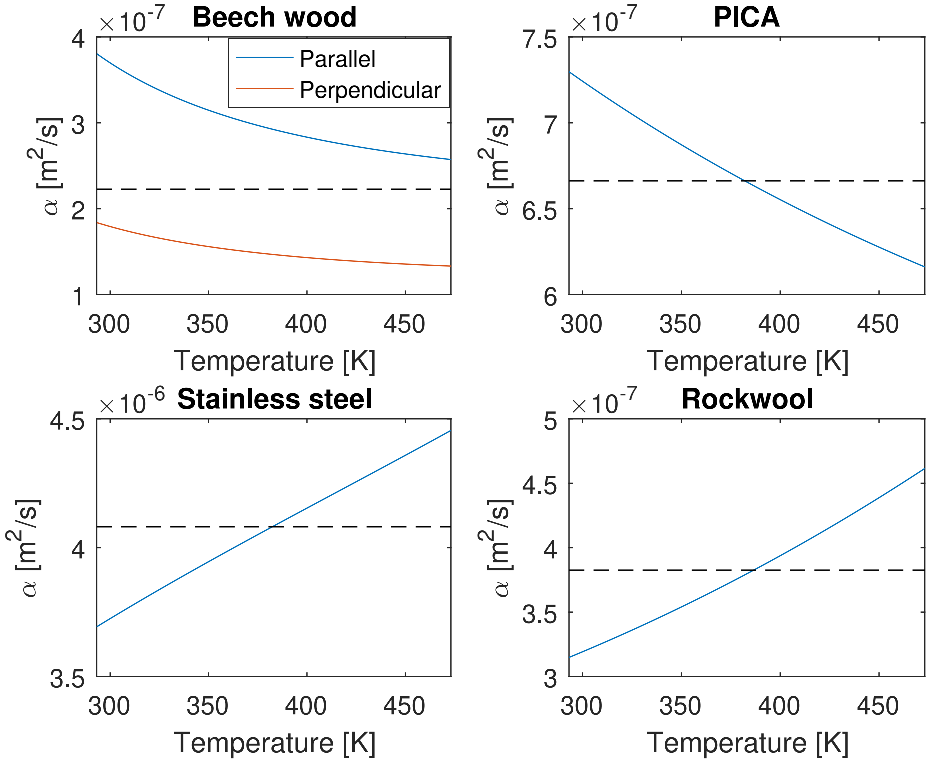

FIGURE 3.1: Thermal diffusivity of beech wood (in the direction parallel and perpendicular to the fibers), PICA (considered as isotropic), AISI304 and mineral wool. The dashed line represents the value of the diffusivity used in the model for each material.

3.1.2 Convective heat transfer

To ensure the two-dimensionality of our model, we assume that the nitrogen flow remains at room temperature (20°C) in the reactor. This is a weak assumption as its residence time is low.

The Reynolds number of the flow passing through the annular section formed by the walls and the assembly can be computed with the following relation:

$$Re_{D_h} = \frac{\rho_{N_2} D_h u_{\infty,z}}{\mu_{N_2}} \tag{3.5}$$

where $u_{\infty,z}$ is the free-stream velocity of the flux in the longitudinal direction, D_h is the hydraulic diameter of the annular section and μ_{N_2} and ρ_{N_2} are respectively the viscosity and the density of the nitrogen at room temperature. We obtain a Reynolds number of 42 and the flow can thus be considered as laminar.

Since the thickness of the annular section formed by the walls of the reactor and the assembly is weak compared to its diameter, we can approximate the Nusselt number with the one of a fully developed laminar flow passing in a channel insulated on one side, with uniform surface temperature in the direction of the flow and along its perimeter [54]:

$$Nu_z = 4.861 \tag{3.6}$$

We then obtain the convective heat transfer coefficient in the longitudinal direction:

$$h_z = \frac{Nu_z k_{N_2}}{D_h} \tag{3.7}$$

with k_{N_2} the thermal conductivity of the nitrogen at room temperature.

The Nusselt number of the nitrogen flowing between the heating plate and the heated surface of the assembly is estimated using the laminar-flow forced heat convection relationship between two flat plates [55]:

$$Nu_{\perp}(r) = 0.664 Re_L(r)^{1/2} Pr^{1/3} \tag{3.8}$$

To compute the Reynolds number Re_L, we need the free stream velocity. This value is problematic since it is not constant as it varies radially over an element of the mesh. Indeed, at constant volumetric flow rate, the velocity of the flux will decrease until it arrives halfway where the duct is the widest and then increases again. Furthermore, the volumetric flow rate is not constant since the flux coming from the top of the reactor will progressively be added to the one coming from its side when the latter moves off its entry (see Figure 2.1). Since we have a two-dimensional model, we need to set a constant velocity for each annular element. Consequently, we compute the average value of the velocity over one element of the mesh:

$$u_{\infty,\perp}(r) = \frac{(\dot{V}_{\perp} + 0.5\dot{V}_z)}{\overline{w}(r) L_{c-d}} \tag{3.9}$$

with $\dot{V}_{\perp}$ and $\dot{V}_z$ the volumetric flow rates of the fluxes coming from the side and the top of the reactor, L_{c-d} the distance between the sample and the ceramic plate and $\overline{w}$ the average width of the duct over the sample computed with this relation:

$$\overline{w}(r) = \frac{1}{r}\int_0^r 2\sqrt{R_w^2 - \rho^2} d\rho = \frac{1}{r}\left(r\sqrt{R_w^2 - r^2} + \arcsin\left(\frac{r}{R_w}\right) R_w^2 \right) \tag{3.10}$$

with R_w the radius of the walls surrounding the assembly. We then can obtain the Reynolds number and the convective heat transfer coefficient for each element:

$$Re_L(r) = \frac{\rho_{N_2} D_d u_{\infty,\perp}(r)}{\mu_{N_2}} \tag{3.11}$$

$$h_\perp(r) = \frac{Nu_\perp(r) k_{N_2}}{D_d} \tag{3.12}$$

3.1.3 Radiative heat transfer

In this model, all the materials are considered as gray bodies. To compute the radiative heat transfer between the periphery of the assembly and the insulating layer covering the walls of the reactor, we make the assumption that the walls remain at constant temperature T_w = 20°C. Since they surround the assembly, the view factor between the periphery of the domain and the walls is equal to 1. The radiative heat flux between each element of the periphery and the walls is thus obtained as follows:

$$q_{rad,e} = \frac{1}{S_{ext,e}} \frac{\sigma(T_w^4 - T_e^4)}{\frac{1-\epsilon_{IC}}{S_{ext,e}\epsilon_{IC}} + S_{ext,e}^{-1} + \frac{1-\epsilon_{IC}}{\epsilon_{IC} S_w}} \tag{3.13}$$

with $S_{ext,e}$ the exterior surface of the element e, T_e its temperature, ϵ_{IC} the emissivity of the insulating layer.

The heating source is modelled as a disk with a temperature increasing linearly during the first 120 seconds of the simulation to reach its maximum temperature (800°C). We suppose that there is no radiative heat transfer between the base of the assembly and the walls of the reactor. The view factor between the heating plate and each element on the side of the assembly facing it is obtained thanks to the formula of the view factor between a disk and a coaxial annular ring on a parallel disk (see Appendix C.1). We thus compute the radiative heat flux between the ceramic and each element at the base of the assembly with the following equation:

$$q_{rad,e} = \frac{1}{S_{a,e}} \frac{\sigma(T_c^4 - T_e^4)}{\frac{1-\epsilon_e}{S_{a,e}\epsilon_e} + (F_{c-e} S_c)^{-1} + \frac{1-\epsilon_c}{\epsilon_c S_c}} \tag{3.14}$$

with $S_{a,e}$ the annular section of the element, T_c the temperature of the ceramic, F_{c-e} the view factor between the heating plate and the element and ϵ_c and ϵ_e the emissivity of the ceramic and of the element (which will vary with the radial position depending if the element is part of the sample, the steel or the wool).

3.2 Dimensions

In this section, we will study the impact of the four critical dimensions on the one-dimensionality of our experiment in order to choose the ones that best fit our constraints. This will be done by comparing the results obtained thanks to the present model to the results obtained with a fully one-dimensional model.

3.2.1 One-dimensional model

This model is the same as the previous one but the radial dimension is removed here and the physical properties are those of beech wood or PICA, depending on the material studied.

$$\rho c \frac{\partial T}{\partial t} = k \frac{\partial^2 T}{\partial z^2} \tag{3.15}$$

with the boundary conditions:

$$k \frac{\partial T}{\partial z}(t, z = L_d) = q_t \tag{3.16}$$

$$\frac{\partial T}{\partial z}(t, z = 0) = 0 \tag{3.17}$$

with q_t the external heat flux arriving on the central element of the base at time t in the 2D model.

To fit our design, the temperature profile of the two-dimensional model has to be as close as possible to the one of the one-dimensional model. The temperature difference is maximal for the node located in $z = L_d$ when its temperature in the two-dimensional model reaches 200°C. All the graphs in this section therefore show the dependency of this particular difference with the four critical dimensions.

3.2.2 Heating source

Figure 3.2 shows the percentage difference in temperature between the two models as a function of the ratio between the diameter of the heating source and the assembly for different vertical distances between the sample and the heating source. We can see that the difference between the two models decreases when the ratio increases. This is due to the fact that a bigger heating source implies a better distribution of the radiative flux. Its diameter however can not exceed the diameter of the assembly since it would imply a radial heating of the walls of the assembly.

The closer the heating source is to the sample, the closer our results are to the one-dimensional ones, except for small heating diameters for which a small distance engenders a much smaller radiative heat flux on the periphery of the sample than on its center and thus more radial losses. Still, this distance can not be too small in order to let the gases freely escape the particle. We therefore set this value to 1 cm (note that for large heating source diameters this value has a low impact on the one-dimensionality of our model).

3.2.3 Assembly

Now that we have the distance between the heating source and the sample, and the relative diameter of the heating source, we can determine the diameter of the sample and the insulation thickness.

On the Figure 3.3, it appears that, in order to minimise the difference between the two models, we have to maximise these dimensions. Increasing these dimensions has indeed two effects: (i) it decreases the radial heat losses at the center of the particle, since it is better insulated, and makes the temperature profile in the 2D case closer to the 1D one; (ii) it increases the diameter of the heating source which has

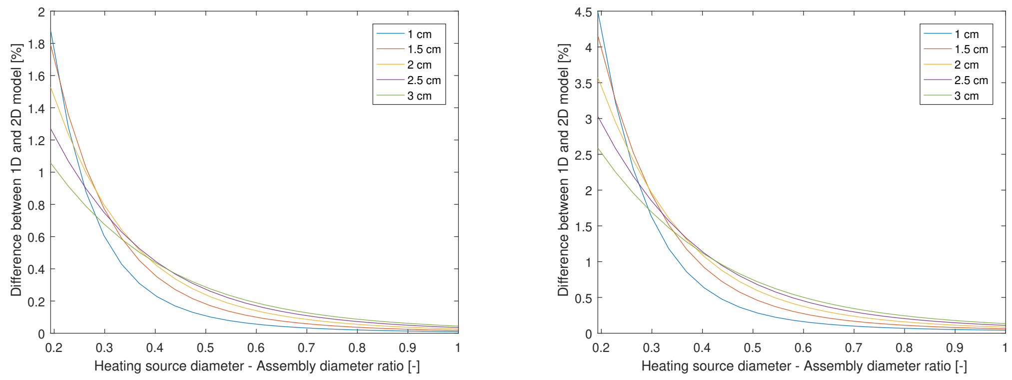

(A) Beech wood sample (B) PICA sample

FIGURE 3.2: Percentage difference in temperature between a 1D and a 2D model for distances between the sample and the heating source between 1 cm and 3 cm. These results are obtained for a sample diameter of 5 cm and an insulation thickness of 3 cm.

the consequence of decreasing the radiative heat flux gradient at the center of the particle.

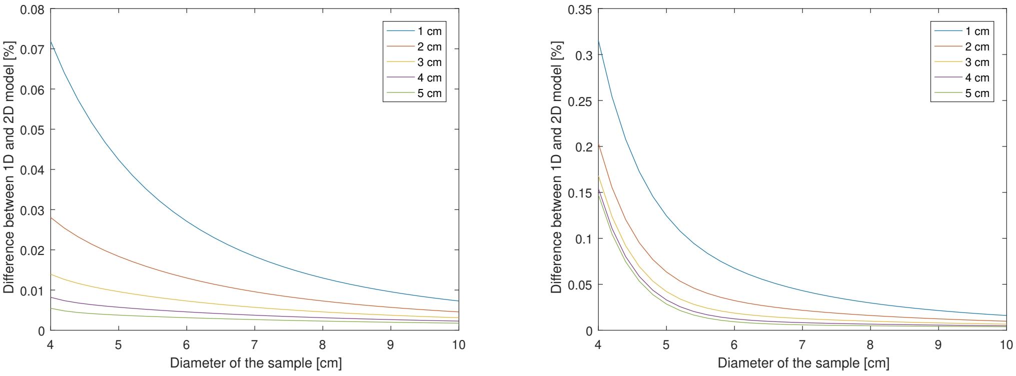

(A) Beech wood sample (B) PICA sample

FIGURE 3.3: Percentage difference in temperature between a 1D and a 2D model for insulation thicknesses between 1 cm and 5 cm.

In addition to increasing the cost of the reactor machining, increasing those dimensions involves some disadvantages. Indeed, increasing the insulation thickness increases the total mass of the assembly which lowers the precision of the weighting system. We thus set this dimension at 3 cm because the difference varies slightly from this value.

Furthermore, as presented in Figure 3.4a for wood, increasing the diameter of the sample increases the temperature difference between its axis and its periphery. This means that the central part of the sample will pyrolyse faster than its periphery and thus the mass flows recorded with the weighting apparatus will get off those obtained in the one-dimensional case. However, on the Figure 3.4b, we can see that beyond 4 cm, the temperature difference decreases with the diameter. This is caused by the fact that, above this value, the increase of the radiative heat flux difference is compensated by the radial diffusivity. This effect also appears for the wood, but for

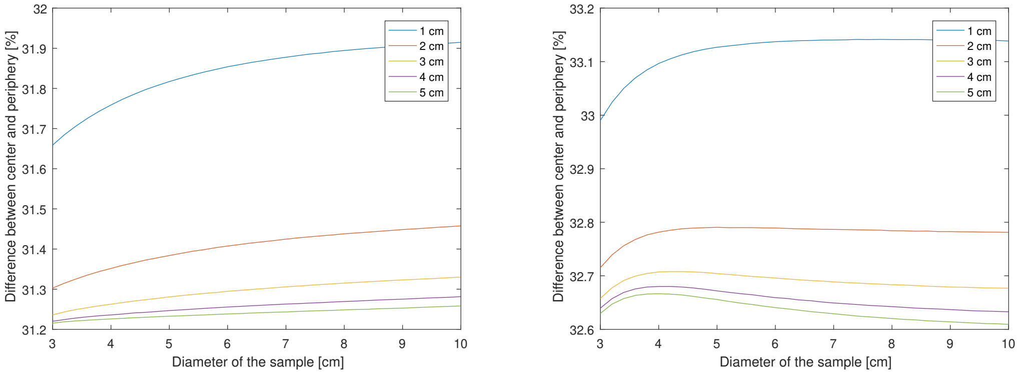

(A) Beech wood sample (B) PICA sample

FIGURE 3.4: Percentage difference in temperature at the base of the assembly between the center of the sample and its periphery for insulation thicknesses between 1 cm and 5 cm.

larger diameters because it has a weaker diffusivity than the PICA.

We therefore set a sample diameter of 5 cm which is a good compromise between the constraints of mass flow and temperature.

3.3 Results

We obtain the following values for the critical dimensions studied in this chapter:

- An insulating layer thickness of **3 cm** ;
- A heating source diameter of **11.4 cm** ;
- A distance between the sample and the heating source of **1 cm** ;
- A sample diameter of **5 cm**.

These dimensions lead to a temperature difference between the two-dimensional and the one-dimensional models of 0.01% for beech and 0.04% for PICA. This value is an upper bound of the error since we consider that the walls of the reactor and the nitrogen flux remain at constant temperature; consequently, the radial heat losses should be smaller. Nevertheless, we have to keep in mind that this model is only valid for temperatures below 200°C and thus the error will continue to grow with temperature, as we shall see in the next chapter.

The Figure 3.5 show the temperature profile in the wood and in the PICA sample when the temperature of each of these materials reaches 200°C. We can see that, close to the base, the temperature gradient in the radial direction becomes very large at the periphery of the sample. This is due to the fact that a lot of heat is lost in the stainless steel since it has a diffusivity about 10 times higher than the one of the sample, and a smaller emissivity, which makes it colder than the wood.

However, when we move away from the base, the stainless steel will radially heat up the sample due to its high diffusivity. In Chapter 5, we discuss a solution to this problem. Nevertheless, this has a small impact on the temperature profile along the axis since the wood is an good insulator and it will not impact the pyrolysis even after a long heating time because the temperature in the stainless steel sheath remains somewhat low.

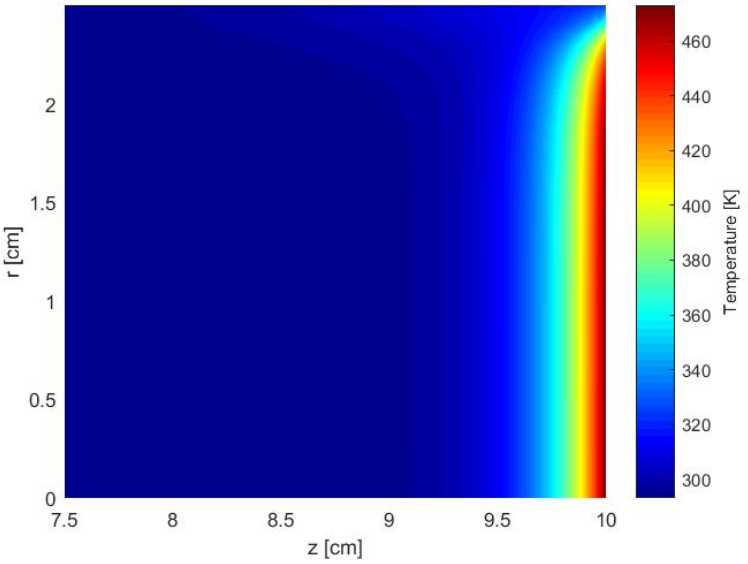

(A) Beech wood sample

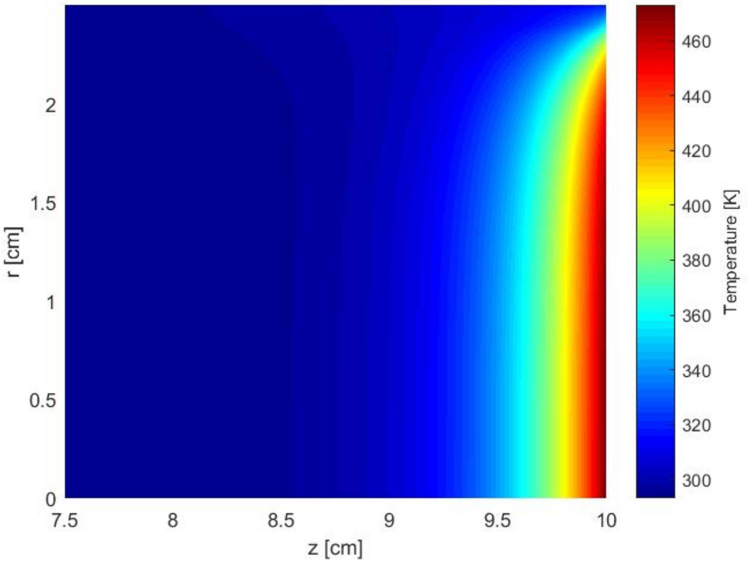

(B) PICA sample

FIGURE 3.5: Temperature profile in the sample when the center of its base reaches 200°C

Chapter 4

Modelisation of the experiment

The SPY algorithm (Single particle PYrolysis) developped by J. Blondeau and H. Jeanmart [46] simulates the pyrolysis of a two-dimensional cylindrical particle under the effect of radial and longitudinal radiative and convective heat fluxes. In order to validate the design and the dimensions of our experiment, we have adapted this algorithm so that it fits our problem. Since this model applies to lignocellulosic biomass only, the pyrolysis of beech wood will be studied here.

4.1 Physical model

The main features of the physical model are :

- Conductive, convective and radiative heat transfers inside the particle;
- Volatiles convection and diffusion in the sample;
- Conductive heat transfers inside the stainless steel sheath and the insulating layer;
- Particle shrinkage evolution;
- Local equilibrium between the solid and the gaseous phase;
- Negligible heat transfer due to species diffusion;
- Convective and radiative heat transfer on the surface of the assembly facing the heating source;
- Convective and radiative heat transfer on the periphery of the insulation;
- Conductive heat transfer between the sample and the stainless steel sheath;
- Radiative heat transfer between the periphery of the sample and the stainless steel and between the periphery of the sample and the heating source when the particle has shrunk.

The energy conservation equations of the previous model is thus adapted as follows:

$$\frac{\partial}{\partial t}(\rho c T) = Q - \frac{1}{r}\frac{\partial}{\partial r}\left(r\hat{\rho}_g c_g u_r T - r k_r \frac{\partial T}{\partial r}\right) - \frac{\partial}{\partial z}\left(\hat{\rho}_g c_g u_z T - k_z \frac{\partial T}{\partial z}\right) \quad \textbf{for} \quad r < R_s \tag{4.1}$$

$$\rho c \frac{\partial T}{\partial t} = \frac{1}{r}\frac{\partial}{\partial r}\left(r k_r \frac{\partial T}{\partial r}\right) + \frac{\partial}{\partial z}\left(k_z \frac{\partial T}{\partial z}\right) \quad \textbf{for} \quad r > R_{s,0} \tag{4.2}$$

with R_s the radius of the sample and $R_{s,0}$ its initial radius (thus equal to the inner radius of the stainless steel sheath), $\hat{\rho}_g$ the intrinsic density of the gases, c_g their specific heat, u_r and u_z their velocity in the longitudinal and radial direction and Q the heat source term computed thanks to the kinetic model of Miller and Bellan [12]. The new boundary conditions are:

$$k\frac{\partial T}{\partial r}(r = R_d, z) = h_z(T_{N_2} - T) + q_{rad}(R_d, z) \tag{4.3}$$

$$k\frac{\partial T}{\partial r}(r = R_s(z), z) = q_{rad}(R_s(z), z) \quad \textbf{if} \quad R_s(z) < R_{s,0} \tag{4.4}$$

$$k\frac{\partial T}{\partial r}(r = R_{s,0}, z) = q_{rad}(R_{s,0}, z) \quad \textbf{if} \quad R_s(z) < R_{s,0} \quad \text{or} \quad z > L_s \tag{4.5}$$

$$k\frac{\partial T}{\partial z}(r, z = L_d) = h_\perp(r)(T_{N_2} - T) + q_{rad}(r, L_d) \tag{4.6}$$

$$\frac{\partial T}{\partial z}(r, z = 0) = 0 \tag{4.7}$$

4.1.1 Physical parameters

In the present model, the stainless steel and the wool are considered as isotropic materials with constant heat capacity and specific mass. Indeed, the stainless steel expansion under the influence of heat is insignificant. These values are thus the same as in the previous chapter. However, the conductivity of these materials (k_{st} for the steel and k_w for the wool) are temperature-dependent and are fitted with the following third order polynomials:

$$k_{st}(T) = 4.31 \cdot 10^{-9}T^3 - 1.16 \cdot 10^{-5}T^2 + 2.4 \cdot 10^{-2}T + 8.62 \tag{4.8}$$

$$k_m(T) = 4.18 \cdot 10^{-11}T^3 + 8.45 \cdot 10^{-8}T^2 + 1.52 \cdot 10^{-5}T + 2.46 \cdot 10^{-2} \tag{4.9}$$

Except for the sample, the emissivity of all the materials is taken as constant and has the same value as in the preliminary model. The sample will have a different emissivity whether it is mainly composed of virgin biomass or of char. Its emissivity is therefore fixed at 0.9, which is a value slightly lower than the one of the virgin beech wood and higher than the one of the char.

The local heat capacity of the sample depends on the temperature and the amount of virgin biomass, char, tar and gases. It is computed thanks to the approach of Blondeau and Jeanmart. The density is dependent on the porosity of the particle, which evolves with the reaction rate. And finally, the conductivity will vary according to the direction of the fibers, the porosity of the medium and the temperature. It is obtained with the model of Kollmann and Cote. In the present model, the fibers are oriented parallel to the axis of the sample.

4.1.2 Heating of the ceramic plate

Given the complexity of the shape of the ceramic plate, we will use a simplified model to determine its heating rate. However, more precise data on its temperature evolution should be obtained experimentally.

We thus make the following assumptions:

- The temperature rises uniformly all over the plate;
- The resistive wire behaves as a perfect resistor and all the power produced by Joule effect is converted into heat and is transmitted to the ceramic;
- The physical properties of the ceramic remain constant;
- No heat is lost by conduction with the surrounding environment.

The temperature evolution of the plate can then be computed with the following equation:

$$c_c m_c \frac{\partial T_c}{\partial t} = W_{ohm} + h_\perp(R_c) S_c (T_{N_2} - T_c) - W_{rad} \tag{4.10}$$

with c_c and m_c the specific heat and the mass of the ceramic plate equal to 0.9 kW kg^{-1} K^{-1} and 0.26 kg respectively, R_c the radius of the heating source and S_c its surface.

The resistive wire passing through the plate slots is 12 m long and its total resistance is thus of 106 Ω. We set an electric potential of 400 V at the borders of this wire. The current is thus equal to 4 A and the heat transmitted from the wire to the plate W_{ohm} is thus obtained as follows:

$$W_{ohm} = IV = 1500 \text{ W} \tag{4.11}$$

As in the previous model, we suppose that there is no radiative heat transfer between the heating source and the walls of the reactor. W_{rad} therefore corresponds to the heat transmitted from the plate to the assembly. The temperature profile obtained with these equations and by limiting the temperature of the plate to 800°C is shown in the Figure 4.1.

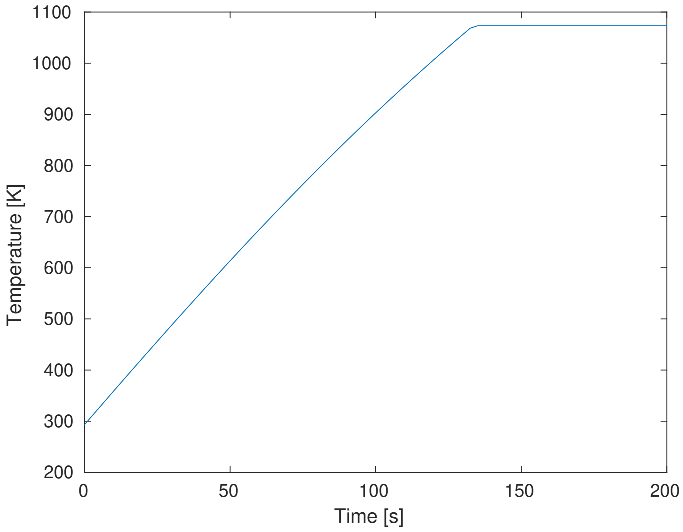

FIGURE 4.1: Temperature evolution in the heating plate

4.1.3 Convective heat transfers

During its pyrolysis, the sample experiences an outflow of volatiles at the same time as it undergoes a cooling convective heat transfer from the nitrogen. This process is called transpirational heating or cooling depending on the direction of the heat flow. Due to the fluid outflow, a thicker boundary layer will be created which will act as an insulator and thus decrease the heat transfer between the surface and the cooling gas [22].

When the particle shrinks, it creates a space between the steel sheath and itself in which gases can flow. However, due to the transpirational effect, we suppose that the convective heat transfer between the sample and the gases is negligible. The one between the sheath and the gases is also neglected due to its weak value compared to the radiative heat transfer.

The convection between the periphery and the base of the assembly and the nitrogen is computed as in the previous model. We consider that the nitrogen flux remains at room temperature.

4.1.4 Radiative heat transfers

We make the same assumptions on the radiative heat transfers as in the previous chapter. This time, not considering the increase of the wall temperature is a stronger assumption since the present model applies to higher temperatures. However, we maintain this assumption since it allows to considerably reduce the computational time.

When shrinkage implies that an element of the sample periphery is no longer in contact with the steel, we compute the radiative heat flux between this element *e* and an element *j* on the inner face of the sheath with the following equation:

$$q_{rad,e,j} = \frac{1}{S_{ext,e}} \frac{\sigma(T_j^4 - T_e^4)}{\frac{1-\epsilon_s}{S_{ext,e}\epsilon_s} + \left(F_{e-j}S_{ext,e}\right)^{-1} + \frac{1-\epsilon_{st}}{S_{int,j}\epsilon_{st}}} \tag{4.12}$$

with $S_{ext,e}$ and $S_{int,i}$ representing the outer surface of the element *e* and the inner surface of the element *j*, ϵ_s and ϵ_{st} the emissivity of the sample and of the stainless steel. F_{e-j} represents the view factor between the element *e* and the element *j* computed thanks to the formula presented in the Appendices C.2 to C.6 (depending on the configuration between the elements). In the same way, we can compute the heat flux between an element on the inner face of the sheath and another one on the outer face of the sample:

$$q_{rad,j,e} = \frac{1}{S_{int,j}} \frac{\sigma(T_e^4 - T_j^4)}{\frac{1-\epsilon_s}{S_{ext,e}\epsilon_s} + \left(F_{e-j}S_{ext,e}\right)^{-1} + \frac{1-\epsilon_{st}}{S_{int,j}\epsilon_{st}}} \tag{4.13}$$

When the particle shrinks, a part of the heat coming from the heating source passes between the interstice formed by the sample and the sheath. We suppose that all this heat is transmitted to the sample and heats its periphery. For each elements *e* on the periphery of the sample and *j* on the inner face of the sheath, not in contact with the other component, the heat flux is thus equal to:

$$q_{rad,e} = \frac{1}{S_{ext,e}} \frac{\sigma(T_c^4 - T_e^4)}{\frac{1-\epsilon_s}{S_{ext,e}\epsilon_s} + (F_{c-e}S_c)^{-1} + \frac{1-\epsilon_c}{S_c\epsilon_c}} + \sum_{j=1}^{N_{st}} q_{rad,e,j} \tag{4.14}$$

$$q_{rad,j} = \sum_{e=1}^{N_s} q_{rad,j,e} \tag{4.15}$$

with N_{st} the number of elements of the sheath no longer in contact with the particle and N_s the number of elements of the particle no longer in contact with the sheath.

Let F_{c-e} be the view factor between the ceramic plate and the periphery of the sample. Since there is no trivial formula to compute it, we approximate it with the following approach:

First, we compute the view factor F_{int} between the heating source and the annular section S_{int} formed at the base of the interstice (see Figure 4.2) with the formula of the Appendix C.1. We then distribute this view factor between the different elements. Since the radial heat flux will be larger for the elements at the base of the sample (represented by point a on the figure) than for those that are further from it (point b), we use the following equation to compute the view factor for each element:

$$F_{c-e} = \frac{F_{int} S_e}{\sum\limits_{k=1}^{N_s} S_k} \tag{4.16}$$

with S_e the section of the heating plate that directly radiates on the periphery of the element e (see Figure 4.2).

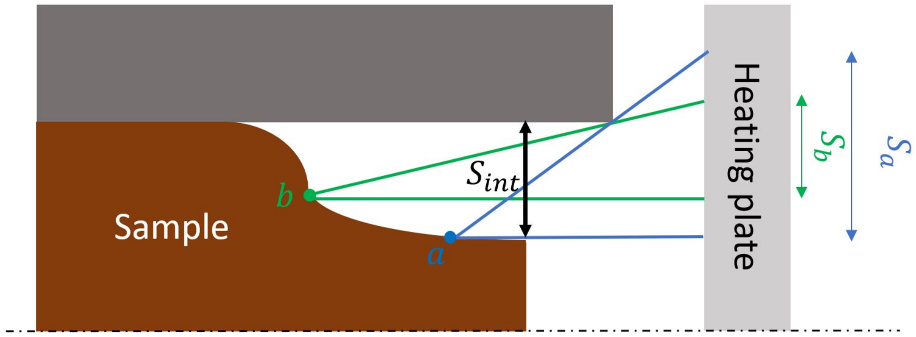

FIGURE 4.2: Schematic of the configuration when a part of the sample has shrunk under the effect of the pyrolysis

4.2 Miller and Bellan kinetic model

The SPY algorithm allows the use of two kinetic models: a version of Ranzi et al. for high temperatures and Miller and Bellan's model. Since our reactor works at relatively low temperature (maximum 800°C), we use the model of Miller and Bellan.

This multi-component model starts from the lignocellulosic biomass composition to compute the global production of char, tar and gaseous species (see Figure

4.3). The same pyrolysis mechanism is applied in parallel to cellulose, hemicellulose and lignin. The kinetic parameters used in the three mechanisms are provided in Table 4.1.

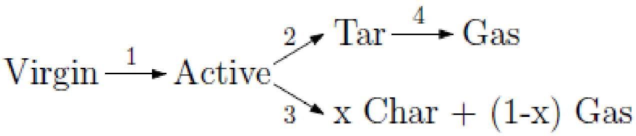

FIGURE 4.3: Miller and Bellan [12] pyrolysis mechanism applied in parallel to cellulose, hemicellulose and lignin (from [20])

.

The activation step (step 1) converts virgin biomass into its activated form, which can be seen as depolymerization and does not produce any mass change. The primary reactions ruling the relative concentrations of char, gas and tar products from the activated solid, are competitive (step 2 and 3). Char and gas are the main products at low temperatures. Their production results from the same reaction and their relative concentration are ruled by the parameter x. The value of this parameter for cellulose, hemicellulose and lignin is also given in Table 4.1. Tar production is dominant at high temperatures and high heating rates.

TABLE 4.1: Kinetic constants for the mechanism of Miller and Bellan [12]

		Cellulose	Hemicellulose	Lignin
A_1	$[s^{-1}]$	2.8×10^{19}	2.1×10^{16}	9.6×10^{8}
E_1	$[kJ\ mol^{-1}]$	242.4	186.7	107.6
A_2	$[s^{-1}]$	3.28×10^{14}	8.75×10^{15}	1.5×10^{9}
E_2	$[kJ\ mol^{-1}]$	196.5	202.4	143.8
A_3	$[s^{-1}]$	1.3×10^{10}	2.6×10^{11}	7.7×10^{6}
E_3	$[kJ\ mol^{-1}]$	150.5	145.7	111.4
A_4	$[s^{-1}]$	4.28×10^{6}	4.28×10^{6}	4.28×10^{6}
E_4	$[kJ\ mol^{-1}]$	108.0	108.0	108.0
x	$[-]$	0.35	0.6	0.75

External reactions are neglected so that secondary reactions are simply described by a heterogeneous tar cracking (step 4). These reactions occur inside the pores of the solid char, with the latter acting as catalyser. As it can be observed from the table, the kinetic constants for this mechanism are the same for the three lignocellulosic components.

4.3 Results and discussion

As in the previous chapter, we will compare the results obtained with the present model with the ones obtained with a one-dimensional model. This model is characterized by pure longitudinal heat and mass transfer as well as shrinkage. It has the same physical characteristics than the sample and it undergoes the same external heat flux than the center of the exposed surface in the two-dimensional model. The previous equations thus become:

$$\frac{\partial}{\partial t}(\rho c T) = Q - \frac{\partial}{\partial z}\left(\hat{\rho}_g c_g u_z T - k_z \frac{\partial T}{\partial z}\right) \tag{4.17}$$

with the boundary conditions:

$$k\frac{\partial T}{\partial z}(t, z = L_d) = q_t \tag{4.18}$$

$$\frac{\partial T}{\partial z}(t, z = 0) = 0 \tag{4.19}$$

with q_t the sum of the radiative and convective heat fluxes arriving on the center of the base at time t.

Since the goal of our experiment is to study the pyrolysis of a semi-infinite particle, the temperature of the point placed at its top along the axis can only slightly increase. Otherwise, the screw inserted at the top of the sample will produce unreliable results. In our simulation, this increase happens after 610 sec. In order to have a better idea of the temperatures and mass flows evolution, we will study the the results obtained during 1000 sec since at this time, the temperature at this point has only increased of 9°C and the results are thus slightly impacted.

The temperature evolution at different points along the axis for the two-dimensional and the one-dimensional model is presented in Figure 5.4.

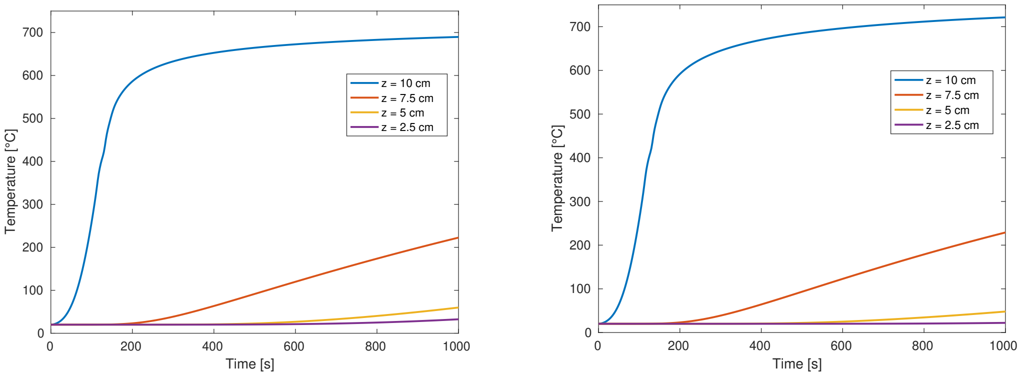

(A) 2D model

(B) 1D model

FIGURE 4.4: Temperature evolution of the points located at 2.5 cm, 5 cm, 7.5 cm and 10 cm from the top of the sample.

We can see that the temperature in the two-dimensional model remains lower than in the one-dimensional model close to the heated surface and slightly higher far from it (difference of 10°C and 6°C for the points at 2.5 cm and 5 cm from the top after 1000 sec). This is due to the fact that the sample is radially heated by the stainless steel. The latter having a higher conductivity than the wood, this impact is more pronounced when moving away from the heat source . However, as mentioned in the previous chapter, this impact is really low.

The Figures 4.5 and 4.6 present the evolution of the relative mass of the sample and the mass flow rates. We see that the mass loss is higher in the one-dimensional case. This is due to the fact that the reactions will happen faster owing to its higher temperature. However, the difference between the two models will tend to decrease after approximately 800 sec because, at this moment, the lower residual mass in the 1D model will counterbalance its higher reaction rate due to the higher temperature.

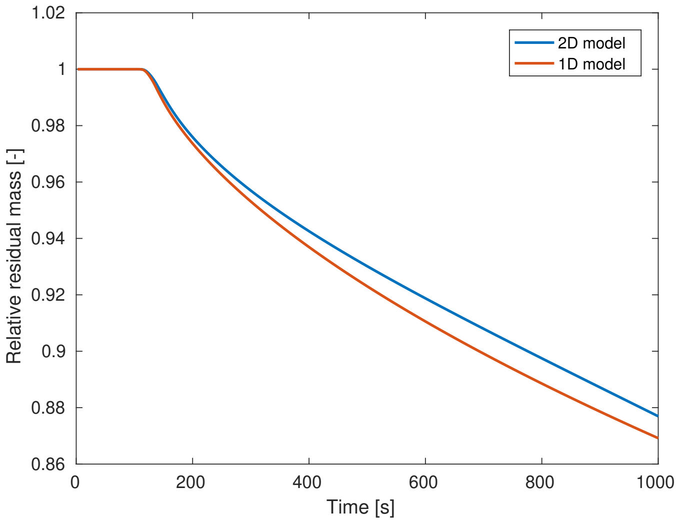

FIGURE 4.5: Evolution of the relative residual mass in the two-dimensional and one-dimensional models

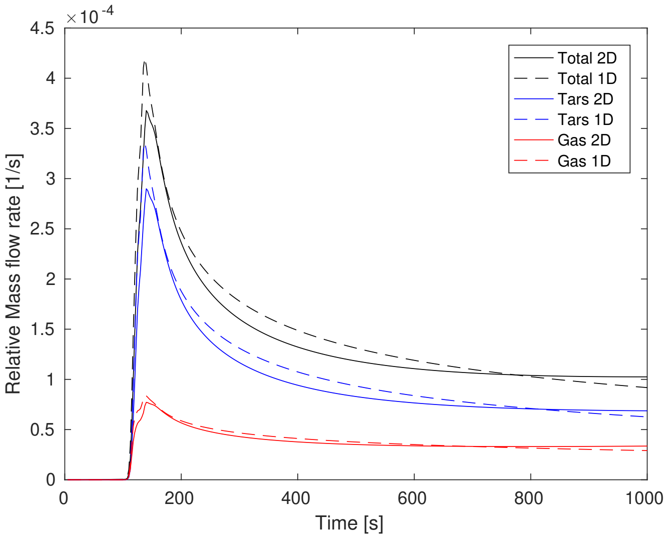

FIGURE 4.6: Evolution of the relative mass flow rate of tar and gas in the two-dimensional (plain) and one-dimensional (dashed) models

The Figures 4.7 and 4.8 present the differences in temperature and residual mass for the two models. We see that these differences remain respectively below 3.5 and 1.5 % during all the simulation which is an acceptable error and confirms the soundness of the chosen dimensions.

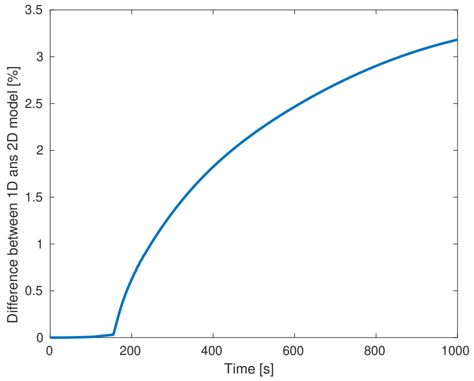

FIGURE 4.7: Evolution of the maximum percentage difference in temperature between the one-dimensional and two-dimensional model

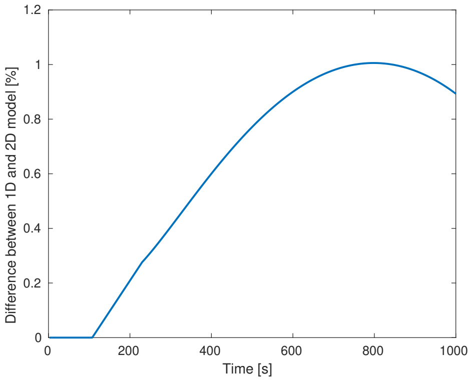

FIGURE 4.8: Evolution of the percentage difference in relative residual mass between the one-dimensional and two-dimensional model

The temperature profiles in the sample at different times are presented in Figure 4.9. It clearly shows the impact of the stainless steel sheath. In the next chapter, we will discuss a solution to diminish this impact.

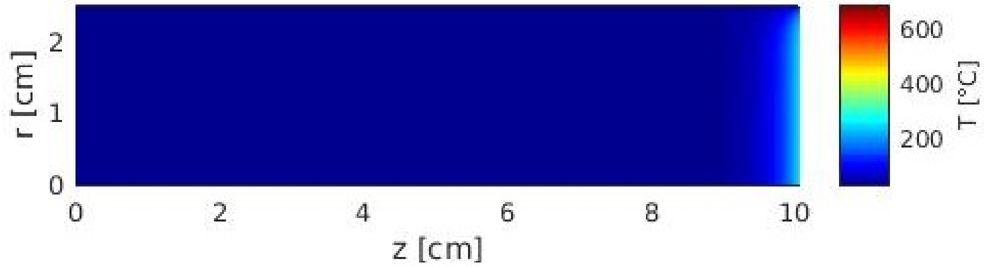

(A) 100 sec

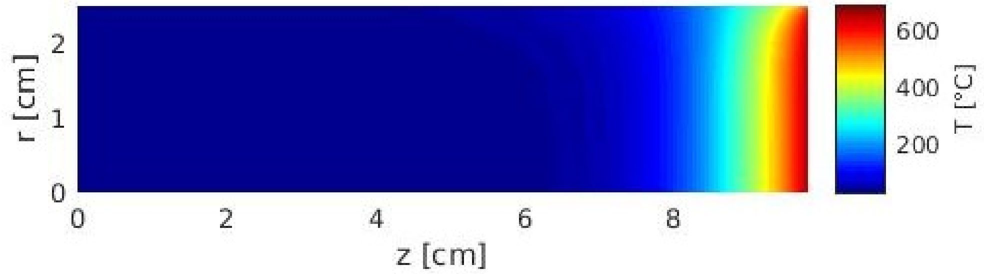

(B) 400 sec

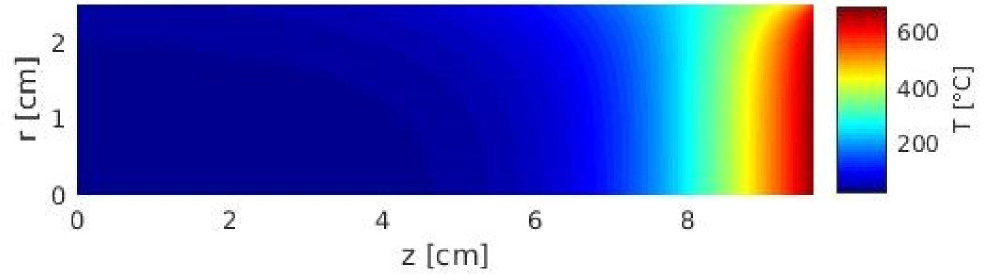

(C) 700 sec

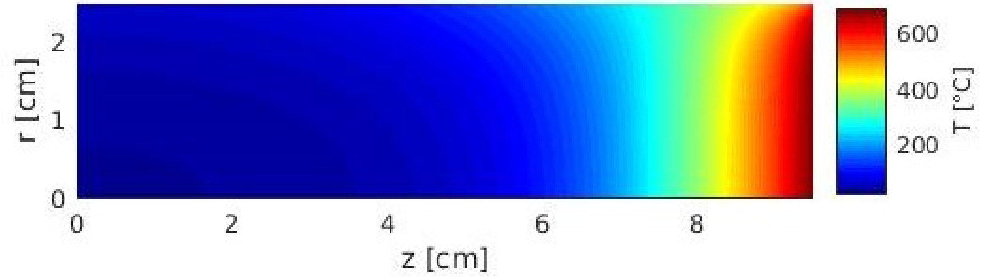

(D) 1000 sec

FIGURE 4.9: Temperature profile in the sample after 100 sec, 400 sec, 700 sec and 1000 sec

Chapter 5

Experiments and outlook for future work

5.1 Assessment of the bench

Before any one-dimensional pyrolysis experiment can be done on the bench, its features should be characterized and its one-dimensionality should be assessed. In this section, we elaborate possible experiments to determine :

- the temperature distribution and heating rate of the heating source;
- the radiative heat flux distribution at the base of the sample;
- the time necessary to purge the oxygen out of the reactor;
- the temperature uniformity of the sample along different cross-section.

5.1.1 Heating source

The temperature distribution and the heating rates of the heating source depend on different parameters as explained in Subsection 4.1.2. These values could be obtained by varying the voltage across the resistive wire and thus varying the heat dissipated by the resistive wire. The temperature profiles could be computed from the measurement of 8 and 9 thermocouples respectively placed on the coil and on the ceramic slab, as shown in Figure 5.1.

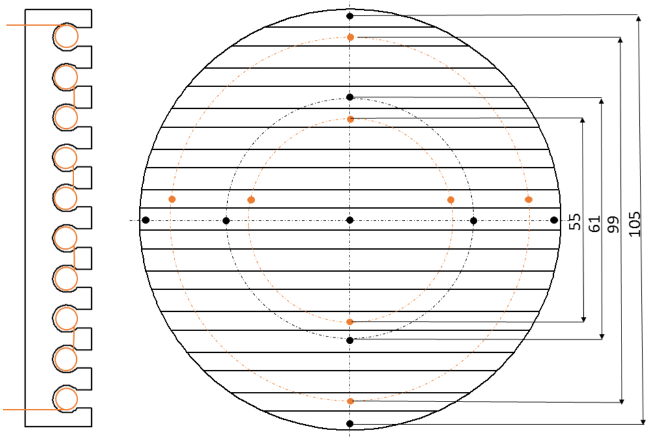

FIGURE 5.1: Positions for the temperature distribution measurements on the heating source (Black : ceramic, orange : coil).

The uniformity of the heating source is an important aspect for the one-dimensionality of the whole setup. It could be determined with the temperature distribution at several voltages. Thus, the slab could be heated step by step, applying 10 different voltages, ranging from 50 to 400V. Each step should be sufficiently long so that the ceramic temperature can stabilize and the temperature distribution can be measured.

Five of the ten voltage values set in the first experiment could be used to compute the heating rate of the ceramic slab. This time, for each voltage, the slab should be heated from ambient to stable temperature. The heating should be quite constant such as the heating rate will simply be computed by dividing the temperature difference by the heating time.

5.1.2 Radiative heat flux

One way to measure the radiative heat flux on the face of the sample assembly would be to heat a plate at the same distance from the heating source as in the reactor (i.e. 1cm) and to place a heat flux meter behind that plate. The intensity distribution could be analyzed by measuring the heat flux in small holes drilled in the plate at certain radii (r = 0, 12.5, 25, 41 and 57mm). These radii were chosen in a way that we would obtain measures at the corresponding positions : the center of the sample, half-radius of the sample, at the intersection between the sample and the steel tube, half-way between the intersection and the edge and at the edge of the insulation. The holes should be positioned along orthogonal axis (see Figure 5.2), with one of the axis parallel to the slots of the ceramic slab. While the intensity is measured in a particular hole, the others should be closed by magnets.

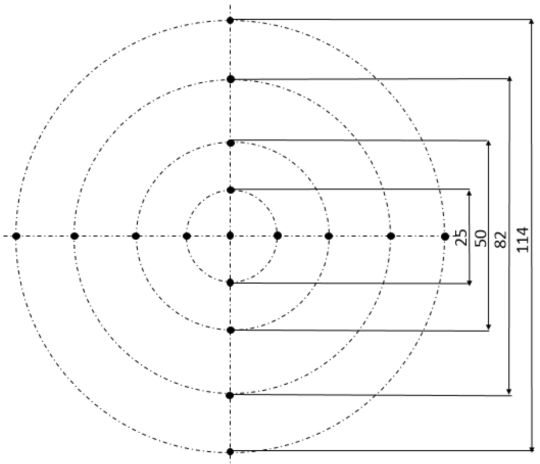

FIGURE 5.2: Positions for the measurement of the intensity of the radiative heat flux

5.1.3 Oxygen purge time

In this work, the nitrogen flow in the reactor was simplified to an isothermal flow for the modelisation of the convective heat transfer. No further analysis was made, as it was outside of the scope of the project (as explained in Subsection 2.5.2). Therefore, it is necessary to measure the time needed to purge the oxygen from the reactor. As various N_2 flows might be used during the experiments, it could be interesting to determine that value for different flow speeds. In the absence of reaction in the reactor, its atmosphere can be considered as inert if the O_2 concentration of the outgoing gas is lower than 0,01%.

When the sample is introduced in the reactor, it will be filled with ambient air and thus with oxygen. Therefore, the oxygen must be flushed before the reaction starts in the sample. It can be done by purging the reactor before heating it with the sample inside. If the heating source is preheated, then the N_2 flow and the temperature of the ceramic slab should be chosen in order for the outflow of the oxygen to be faster than the heating of the sample.

If we consider the mean residence time as the ratio ratio of the internal volume of the reactor and the nitrogen flow at inlet ($t_res = V/\dot{V}$) we obtain a value of 5,7s. Off course, the real value will depend on the laminarity of the flow. We can suppose that with the flow rates chosen 30s should be sufficient.

5.1.4 Sample temperature uniformity

The more uniform the temperature is, the more accurate the one-dimensional approximation will be in our experiments. As during the experiments the temperature will be measured along the axis only, it could be useful to measure the temperature distribution at various heating temperatures and cross-sections. The data obtained will provide an estimate of the error of a 1D modelisation compared to a 2D one, similar to what was done in the previous sections.

For this experiment, each sample will be heated up until the thermocouple at its top records an increase in temperature of approximately 10°C, with heating source control temperatures of 300, 425, 550, 675 and 800°C. An inert atmosphere must be ensured in the reactor. To study the uniformity, measurements can be taken in the same conditions as during the main experiments, but the thermocouples should be placed differently. The temperature could be measured at 0, 30 and 60 mm from the base for radii r= 0, 10 and 20 mm. Four thermocouples should be used per radii in order to obtain multiple values. Because the thermocouples might have a local effect on temperature, it should be avoided to place two thermocouples side by side. One possible positioning is given in Figure 5.3. The acquisition card being equipped with 16 entries, the experiment should be carried out section by section with a new sample.

As the materials used are known to be anisotropic [22, 42], the result will depend on the orientation of the fiber in the sample. Indeed if the fibers are oriented along the axis, the temperature gradient along the cross section will be higher because wood thermal conductivity in the perpendicular direction is lower than along the fibers.

The results obtained with a fiber orientation perpendicular to the axis should however be considered carefully. Indeed, the temperature profile with this configuration will be further away from the one-dimensional case due to the higher radial conductivity of the sample and thus the increase of radial losses. Furthermore, the radial shrinkage will not happen uniformly as it is influenced by the angular position.

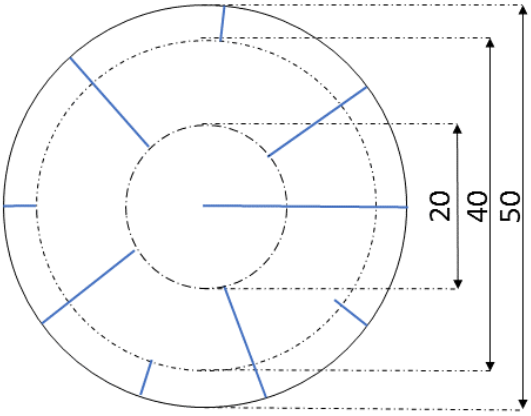

FIGURE 5.3: Measuring of the temperature distribution in the sample (blue : Thermocouples).

5.2 Experimental procedure

The way the reactor is designed allows us to study the evolution of the mass of the sample during pyrolysis as well as the properties of the produced char. In this section, we describe the sample preparation and an experimental procedure.

5.2.1 Sample preparation

In order to insert the 0.5mm thermocouples into the sample, 9 holes of the same diameter should be drilled radially to its center. As explained in Subsection 2.5.1 it is recommended to use a guide to help with the radial drilling. Starting from the base of the cylinder, a distance of 1cm should separate every hole along the axis. Furthermore, 10 tracks (1 thermocouple will be positioned on the surface) should be shaped from the upper face of the sample to the hole for the corresponding thermocouple. They should be grouped in two groups of five tracks, side by side and radially opposed to the other group as shown in Figure 5.4b.

Moreover, a M51 tapped hole should be drilled on the upper face for the insertion of the screw of the hanging cable (see Figure 5.4a). Once this is done, the wood samples should be dried in an oven at 105°C for 12 hours and saved in a desiccator until they are used (Following french standard NF EN 14774 and procedure used in [1, 22, 27]). No drying is needed for PICA as it should not contain moisture.

5.2.2 Experiment

Before starting the experiment, the sample will need to be weighted. Then, the thermocouples can be positionned into the sample pulling them along their respective track before inserting the sample into the stainless steel tube (see Figure 5.5a). The face of the sample that will be heated should coincide with the faces of the tube and the surrounding wool glued to the latter. The sample and the tube are maintained together using tap screws.

Once this is done, the cable can be screwed into the sample, up to the positioning nut and the thermocouples can be pulled through the two holes in the upper insulation wool and the disk (see Figure 5.5b). The disk can be tightened against the wool

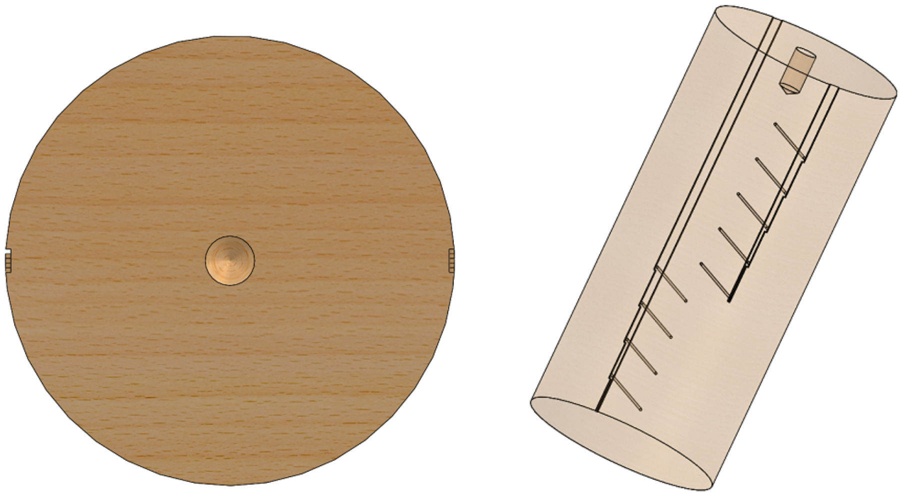

(A) Upper face

(B) Overview

FIGURE 5.4: Drawing of the sample preparation : thermocouple holes and tracks, tapped hole for the screw to hang the sample

to press it against the upper face of the sample and its surrounding insulation.

Then, the cable can be pulled through the clamps and the gas seal to be hooked under the weighing scale. The thermocouples can be pulled through the two clamps, plugged into the acquisition card. The transducers sealing glands can be assembled around them and fixed in the upper clamp (see Figure 5.5c). Finally, the clamps can be placed correctly and the reactor can be sealed.

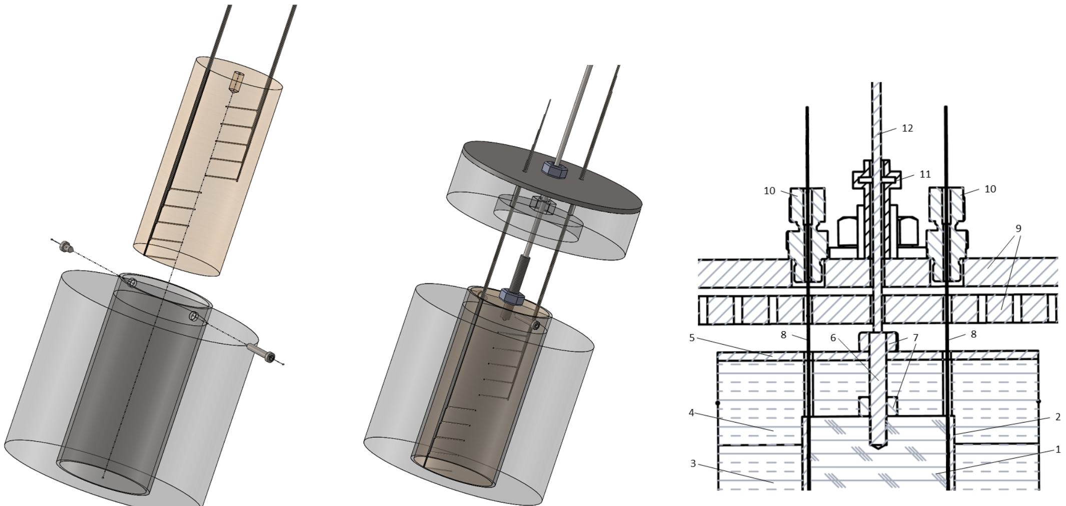

(A) Sample insertion

(B) Cable and upper insulation

(C) Cable and thermocouples in the clamp

FIGURE 5.5: Schematic drawing of the installation procedure (1 : Sample; 2 : Steel tube; 3 : Surrounding wool; 4 : Upper wool; 5 : Pressing disk; 6 : Screw; 7 : Nut; 8 : Thermocouple; 9 : Clamp; 10 : Transducer sealing gland; 11 : Gas seal; 12 : Cable)

Once the reactor is sealed, oxygen can be purged from it by setting a high N_2 flux until the O2 concentration reaches less than 0,1%. We then set the top N2 flow to 6.5 NL min^{-1} and the lateral one to 1.4 Nl min^{-1} (see Section 2.5.2) and the heating source to the desired temperature.

At the end of the experiment, the power source of the resistance is turned off. The N_2 flow should not be shut off and could even be increased, as no gas analyze is made. This way, the gas flow will cool down the heating source and the sample, stopping the reactions.

After the experiment, the shape and size as well as the weight of the sample will need to be measured. Analysis of the temperature profile and the mass loss can be done from the data collected during the experiment. Furthermore, using the data collected before and after the experiment, the apparent density and shrinkage can be analysed. The porosity of the obtained char could also be observed by micrography.

5.3 Outlook for future works

In this section, we present several features that can be added to improve the present design and obtain results closer to the one-dimensionality.

In terms of insulation, using a quartz glass tube instead of stainless steel might improve the assembly. The purpose of this tube is to fix the wool around the sample. Therefore it needs to be really thin and its diffusivity needs to be low. Expressions to compute the conductivity and the specific heat of the quartz are respectively given in Equations 5.1 and 5.2, its density is equal to 2200 kg m^{-3} [56] and its emissivity to 0.93 [49]. As presented in Figure 5.6, the diffusivity of the quartz is in average 12 times lower than the one of the stainless steel.

$$k(T) = 3 \cdot 10^{-9} T^3 - 6.31 \cdot 10^{-6} T^2 + 4.94 \cdot 10^{-3} T + 0.36 \tag{5.1}$$

$$c(T) = 931.3 + 0.256T - 24 \cdot 10^6 T^{-2} \tag{5.2}$$

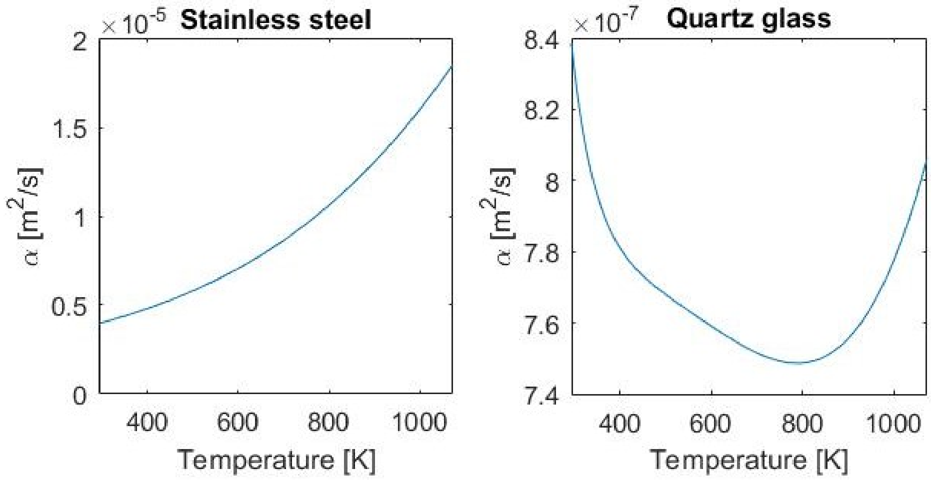

FIGURE 5.6: Thermal diffusivity of stainless steel AISI304 and quartz glass

The quartz glass is thus a more fitted material than the stainless steel for our design since it will lower the radial heat losses near the base of the sample and will transmit less heat to the points that are far from it. However, stainless steel is easier to assemble with the other components and is also cheaper. One should thus determine if the gain in one-dimensionality of a quartz sheath is worth it.

Moreover, to lower the convective heat losses, the N_2 flow could be preheated. Indeed, the temperature difference between the flow (20°C) and the sample is high. However, knowing that the convective heat transfer is small and that the sample is insulated with mineral wool, it should be assessed if it is worth adding another heating source for the gas flow. Once again, this would require a more accurate modelling of the N_2 flow in the reactor.

Finally, analysing the char, tar and gas products would allow a deeper study of the pyrolysis mechanisms in the reactor. FTIR for example would enable to have a closer look at the remaining solid. Installing a cold trap at the outlet of the reactor would enable the analysis of the tar while the use of a GC would allow to identify and quantify the gaseous products. But these tests would require to optimize the N2 flow dragging these species out of the reactor. Indeed, residence time has a big impact on secondary reaction and thus on the tar and gas products. Furthermore, an online analysis require to avoid back-mixing. This is partly done by ensuring a laminar flow.

Conclusion

The aim of this thesis was to create a pyrolysis reactor in such a way that the problem could be modelled as one-dimensional. Starting from the experimental data collected, models from biomass conversion and thermal protection systems could be compared. As a first step, our work is only focused on the heating of a large piece of wood or Phenolic Impregnated Carbon Ablator (PICA) under inert atmosphere. A weighing system is also integrated to the apparatus.

The state of the art review reveals a lack of information on operating conditions and experimental data. This, linked to the variability of the feedstocks used, does not allow a comparison between the different pyrolysis experiments on large particles. Among them, only two experiments were created with the same objective of one-dimensionality. The work of Gronli, in particular, has been very helpful in carrying our thesis as the geometry chosen is similar to it.

The reactor consists in a cylindrical sample, radiatively heated on one face and insulated on the others. This assembly is hanging from a balance - placed above the reactor - to measure the evolution of the relative mass of the sample. A cylindrical internally insulated casing closes the reactor. A Nitrogen flow ensures an inert atmosphere and flushes the volatiles produced at the level of the particle. The heating is done with a resistive wire inserted in a ceramic plate. In order to measure the temperature profile, thermocouples are inserted along the axis of the sample.

The critical dimensions were determined based on a preliminary model. The heating of the sample was characterized below pyrolysis temperatures considering conductive heat transfers inside the assembly formed by the particle, its sheath and its surrounding insulation, as well as radiative and convective heat transfers at the base and the periphery of the assembly. The diameter of the sample and the heating source, the thickness of the insulating layer and the distance between the assembly and the heating source were studied in order to best satisfy the constraints of one-dimensionality. Based on the chosen dimensions, the temperature evolution along the axis fits quite well the constraint of one-dimensionality with a maximum difference between the one-dimensional and two-dimensional case of 0.04% for the PICA and 0.01% for the wood.

In order to validate the setup designed, we adapted the SPY algorithm simulating the pyrolysis of a cylindrical biomass particle under radiative and convective heat fluxes. In addition to the heat transfers considered in the preliminary model, this two-dimensional model includes: (i) convective and radiative heat transfers inside the particle; (ii) mass transfers; (iii) shrinkage of the particle; (iv) local equilibrium between the solid and the gaseous phase; (v) pyrolysis kinetic reactions (Miller and Bellan's model). The results are encouraging as the differences in temperature profiles and residual mass with a one-dimensional model remain below 3.5

and 1.2%.

Before any one-dimensional pyrolysis experiment can be done on the bench, its features should be characterized and its one-dimensionality should be assessed. Possible experiments were suggested to determine the temperature distribution and the heating rate of the heating source, the radiative heat flux distribution and the temperature uniformity of the sample cross-sections. Finally, an experimental procedure was described and the outlook for additional features and further improvement was discussed. In particular, we have addressed the possibility to choose quartz instead of steel to wrap the sample, the need to optimise the N_2 flow. Adding tar and gas analysis could also permit to achieve a complete characterisation of the pyrolysis in the reactor.

Appendix A

Technical drawings of the pyrolysis bench

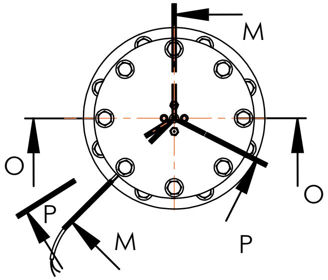

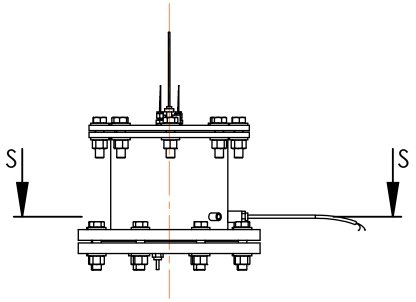

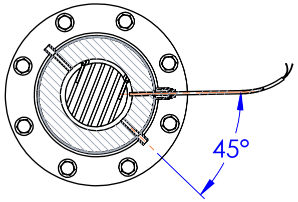

COUPE S-S

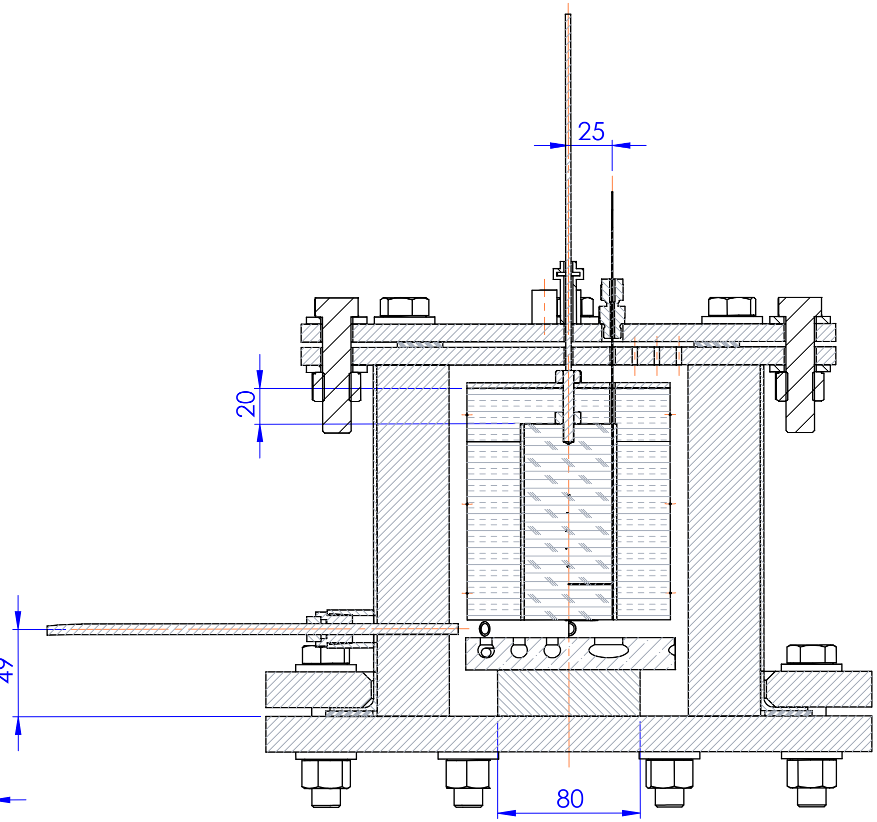

COUPE M-M
ECHELLE 1 : 3

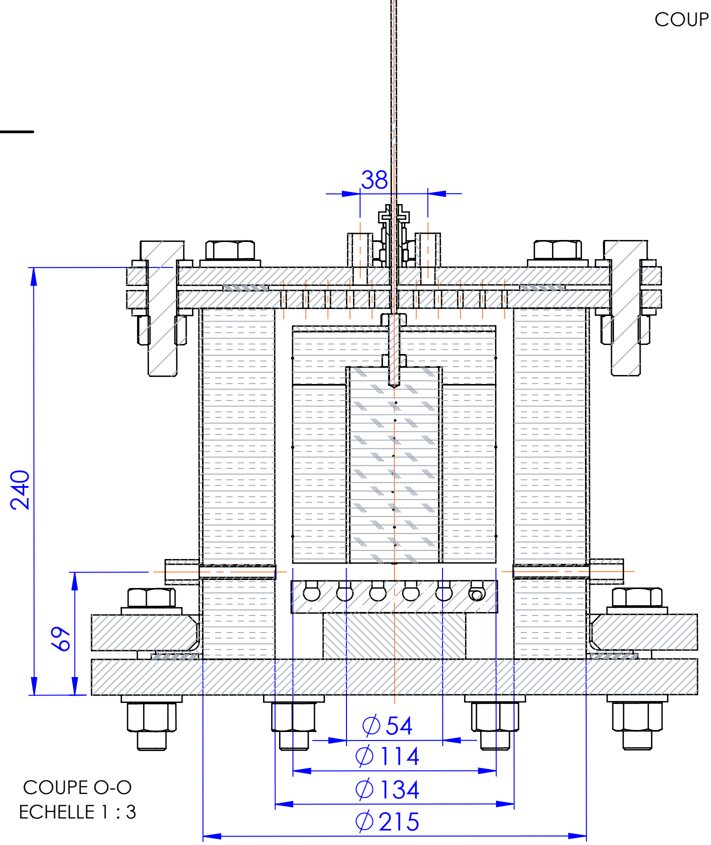

COUPE O-O
ECHELLE 1 : 3

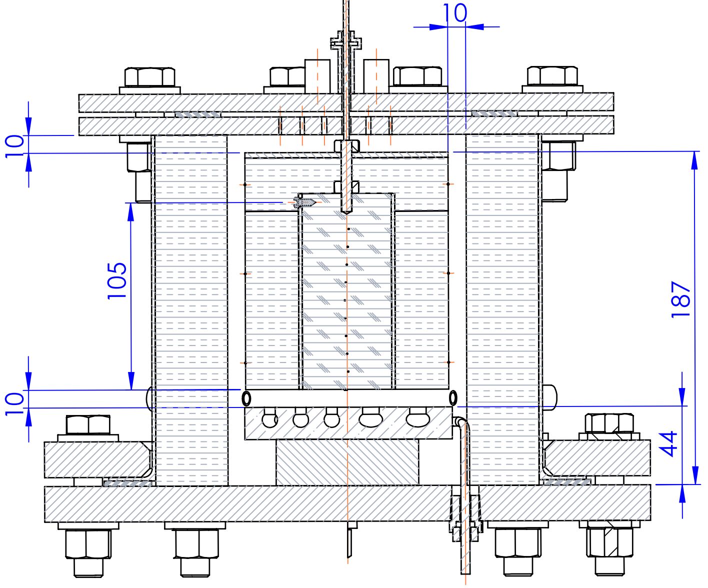

COUPE P-P
ECHELLE 1 : 3

Tolérance:
Etat de surface:
Auteur: Arnaud Lion
Date: 05-05-20
Rév:
Matériau:
Masse: 44815.53 gr
Projet: Projet
Description:
Banc Pyrolyse

Conception, Réalisation et Essais de Dispositifs ElectroMécaniques
Institute of Mechanics, Materials, and Civil Engineering
Place du levant, 2 bte L5.04.03 B-1348 Louvain-la-Neuve

Référence:
No. de plan:
Echelle: 1:10
Feuille: 1/2
Format: A3

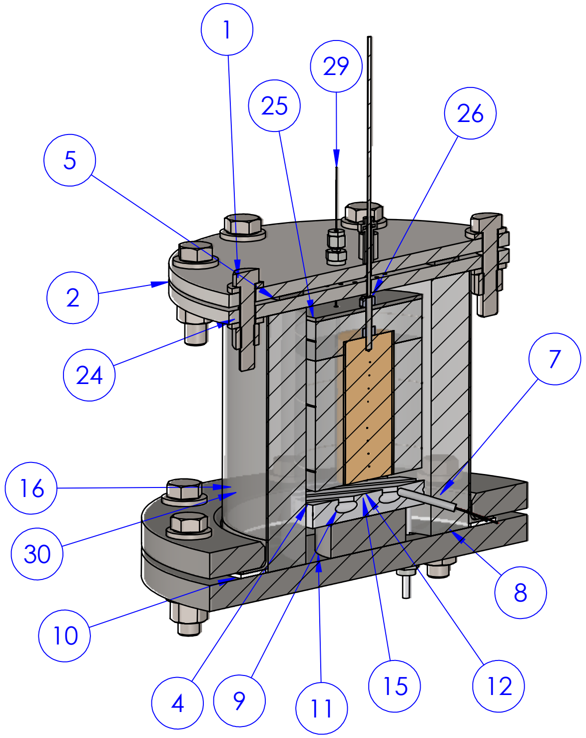

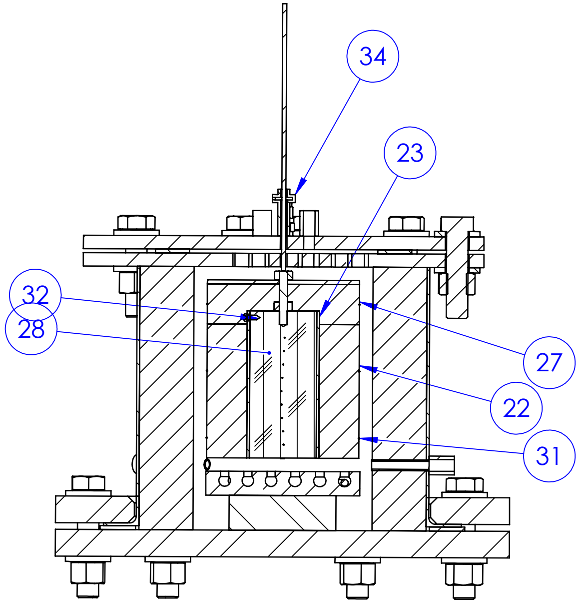

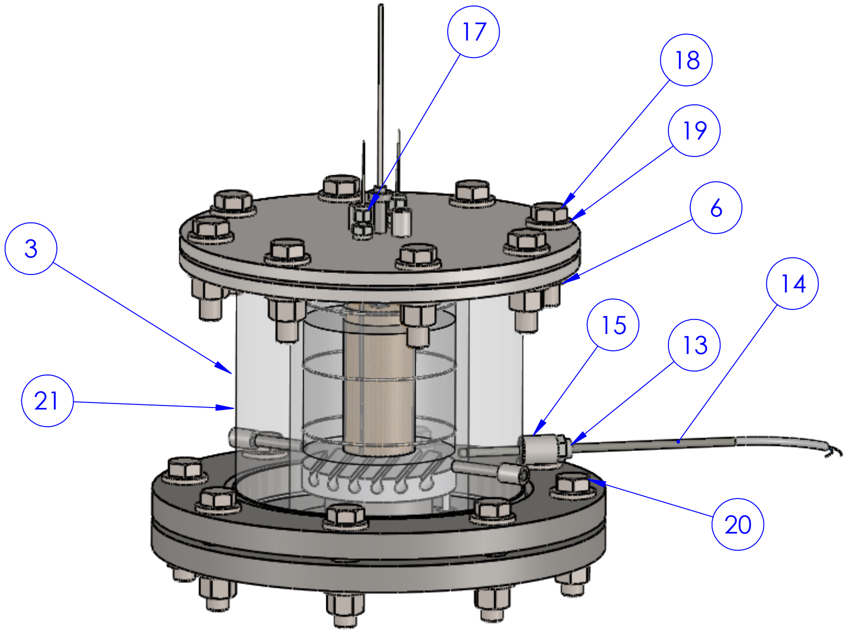

No. ARTICLE	NUMERO DE PIECE	QTE
1	Bride Dia.300	1
2	Bride Dia.300 - 2	1
3	Enveloppe extérieur	1
4	Dalle céramique avec fil	1
5	Joint DN100	1
6	ISO - 4033 - M16 - W - N	16
7	Bride DN 200	1
8	Bride DN 200 - pleine	1
9	collet DN200	1
10	Joint DN200 Graphite	1
11	Entretoise	1
12	SS-CM-FL4-NS6 (FITOK).stp	3
13	E9rieure .stp	3
14	Sonde température	1
15	Manchon inox 3-8	1
16	Manchon 1-8 gaz	4
17	presse étoupe 1-8 G.stp	2
18	DIN EN 24016 - M16 x 65 x 38-WN	8
19	Washer ISO 7415 - 16	32
20	DIN EN 24016 - M16 x 80 x 38-WN	8
21	Fibre céramique extérieur	1
22	Fibre extérieur bois	1
23	Tube extérieur bois	1
24	Câble	1
25	Disque de presse	1
26	Ecrou	2
27	Fibre supérieur	1
28	Echantillon	1
29	Thermocouple	10
30	Tube de sortie	2
31	Fil serrage fibre céramique	3
32	Tapping Screw ISO 14585 - ST2.9 x 9.5-C-N	1
33	Tapping Screw ISO 14585 - ST2.9 x 6.5-C-N	1
34	Gas seal	1

Tolérance:
Etat de surface:
Auteur: Arnaud Lion
Date: 22/04/20
Rév:
Projet: Projet
Matériau:
Masse: 44815.53 gr
Description:
Banc Pyrolyse

UCLouvain
Conception, Réalisation et Essais de Dispositifs ElectroMécaniques
Institute of Mechanics, Materials, and Civil Engineering
Place du levant, 2 bte L5.04.03 B-1348 Louvain-la-Neuve

Référence:
No. de plan:
Echelle: 1:4
Feuille: 2/2
Format: A3

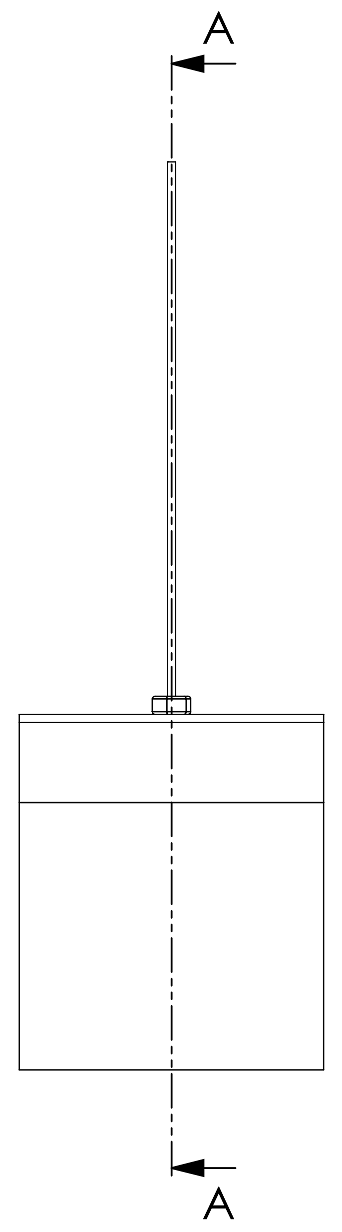

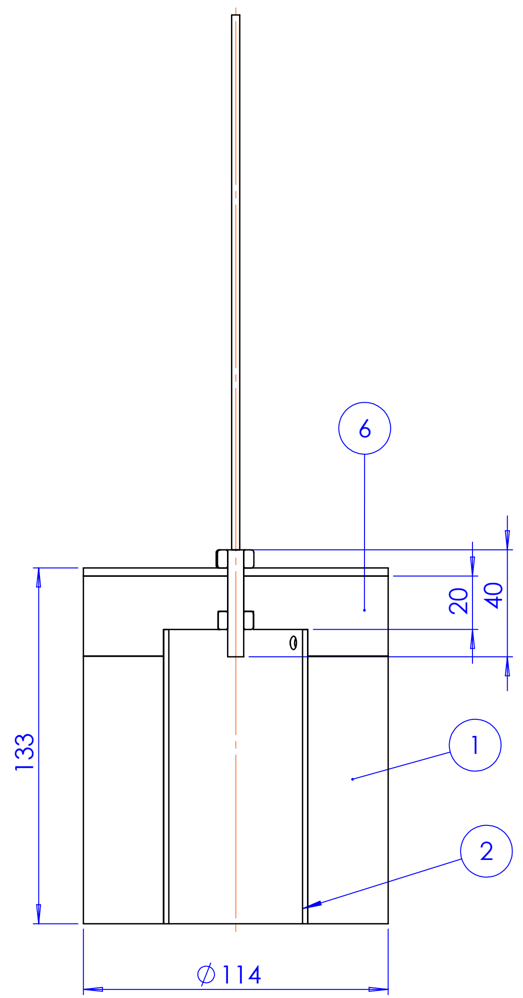

COUPE A-A
ECHELLE 1 : 2

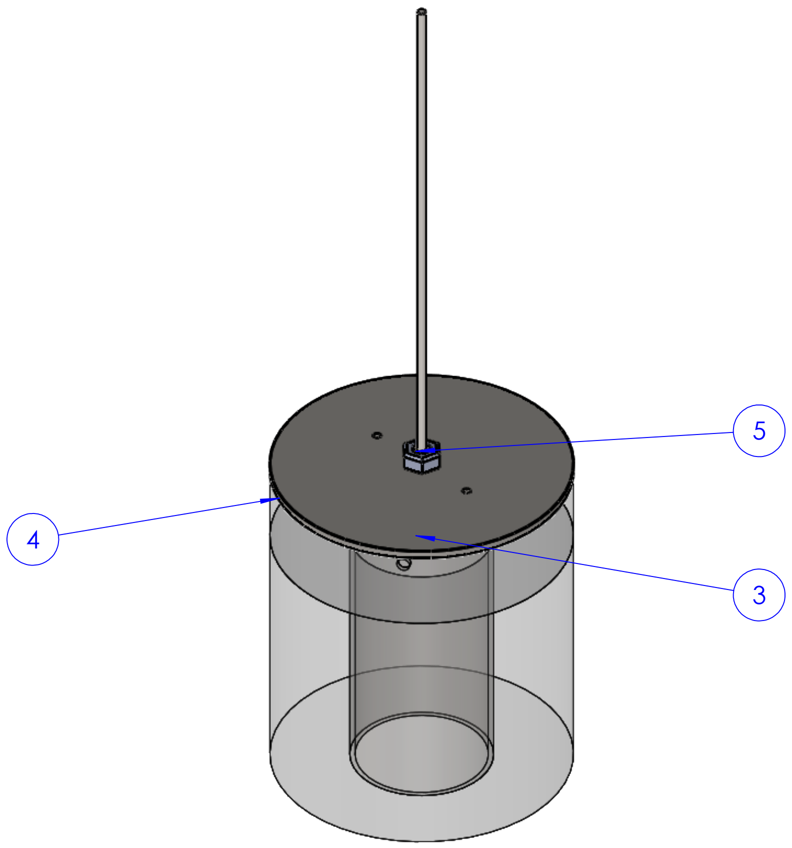

No. ARTICLE	NUMERO DE PIECE	QTE
1	Fibre extérieur bois	1
2	Tube extérieur bois	1
3	Câble	1
4	Disque de presse	1
5	Ecrou	2
6	Fibre supérieur	1

Tolérance: 1
Etat de surface:
Auteur:Arnaud Lion
Date: 05-05-20
Rév: 1
Projet: Banc pyrolyse
Matériau:
Masse: gr
Description: Assemblage peson échantillon

UCLouvain

Conception, Réalisation et Essais de Dispositifs ElectroMécaniques
Institute of Mechanics, Materials, and Civil Engineering
Place du levant, 2 bte L5.04.03 B-1348 Louvain-la-Neuve

Remarques: Modifié par Julien Benoit
No. de plan:
Echelle: 1: 2
Feuille: 1/1
Format: A3

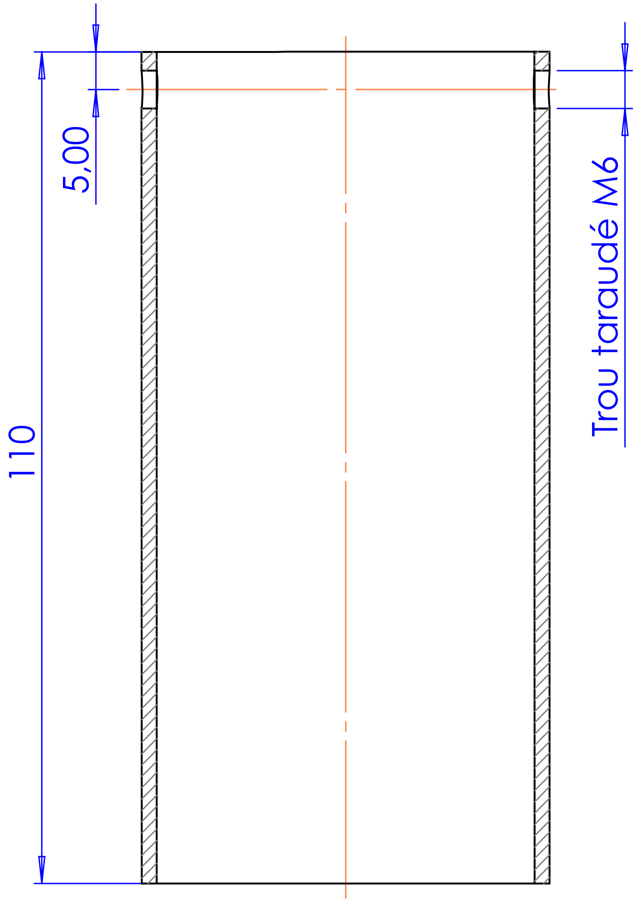

COUPE A-A
ECHELLE 1 : 1

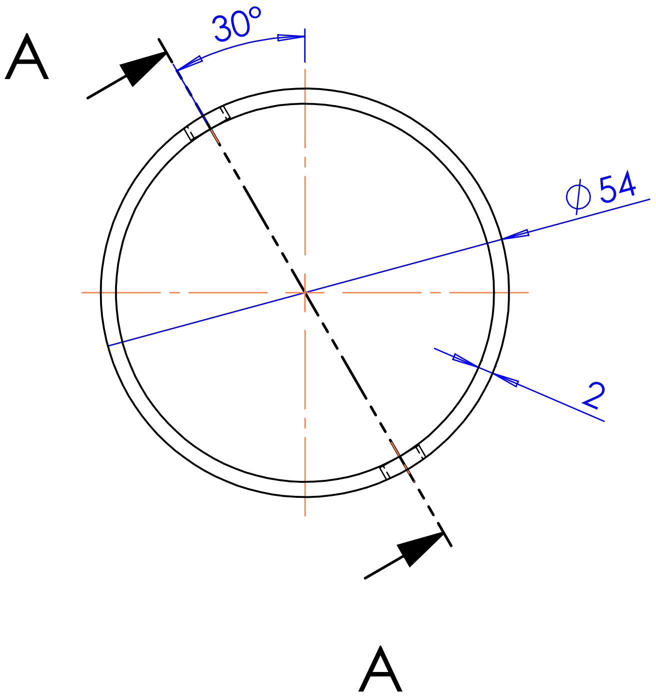

			Tolérance: 1	Etat de surface:
Auteur:Arnaud Lion	Date: 05-05-20	Rév: 1	Projet: Banc pyrolyse	
Matériau: AISI 304				
Masse: 286.89 gr			Description: Tube inox Extérieur bois	
UCLouvain **Conception, Réalisation et Essais de Dispositifs ElectroMécaniques** Institute of Mechanics, Materials, and Civil Engineering Place du levant, 2 bte L5.04.03 B-1348 Louvain-la-Neuve			Remarques: Modifié par Julien Benoit	
			No. de plan:	
			Echelle: 1:1	Feuille: 1/1
			Format: A4	

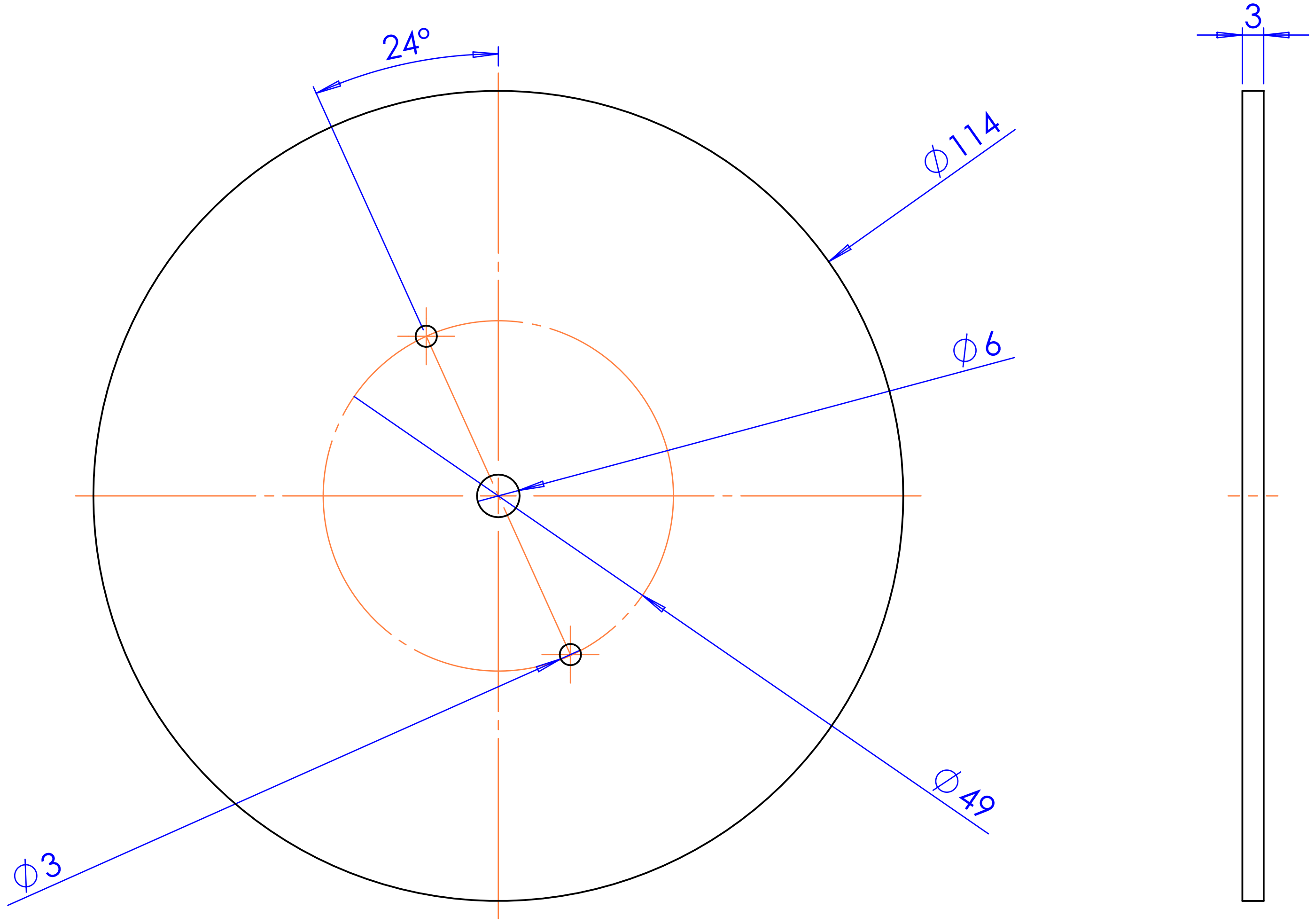

Tolérance: 1
Etat de surface:

Auteur:Arnaud Lion
Date: 04-05-20
Rév:
Matériau: Aisi 304
Masse: 243.95 gr

Projet: Banc pyrolyse
Description: Disque de presse

UCLouvain

Conception, Réalisation et Essais de Dispositifs ElectroMécaniques
Institute of Mechanics, Materials, and Civil Engineering
Place du levant, 2 bte L5.04.03 B-1348 Louvain-la-Neuve

Remarques:
No. de plan:
Echelle: 1:1
Feuille: 1/1
Format: A4

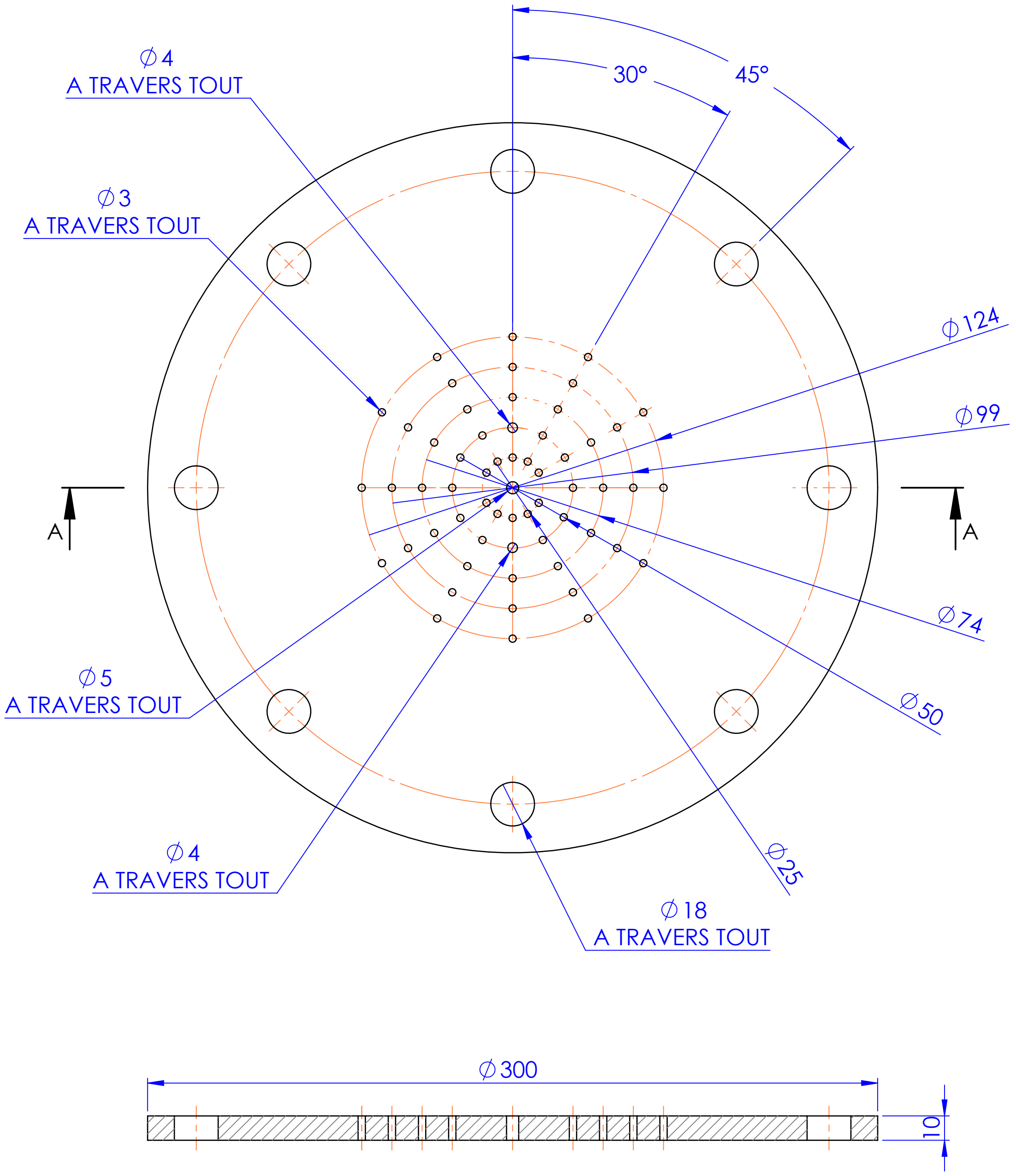

COUPE A-A
ECHELLE 1 : 2

Auteur: Arnaud Lion	Date: 04-05-20	Rév:	Tolérance: 0.1 / Etat de surface: 1.6
Matériau: 1.0037 (S235JR)			Projet: Banc pyrolyse
Masse: 5320.34 gr			Description: Bride Ø300
UCLouvain Conception, Réalisation et Essais de Dispositifs ElectroMécaniques Institute of Mechanics, Materials, and Civil Engineering Place du levant, 2 bte L5.04.03 B-1348 Louvain-la-Neuve			Référence: No. de plan: / Echelle: 1:2 Feuille: 1/1 Format: A3

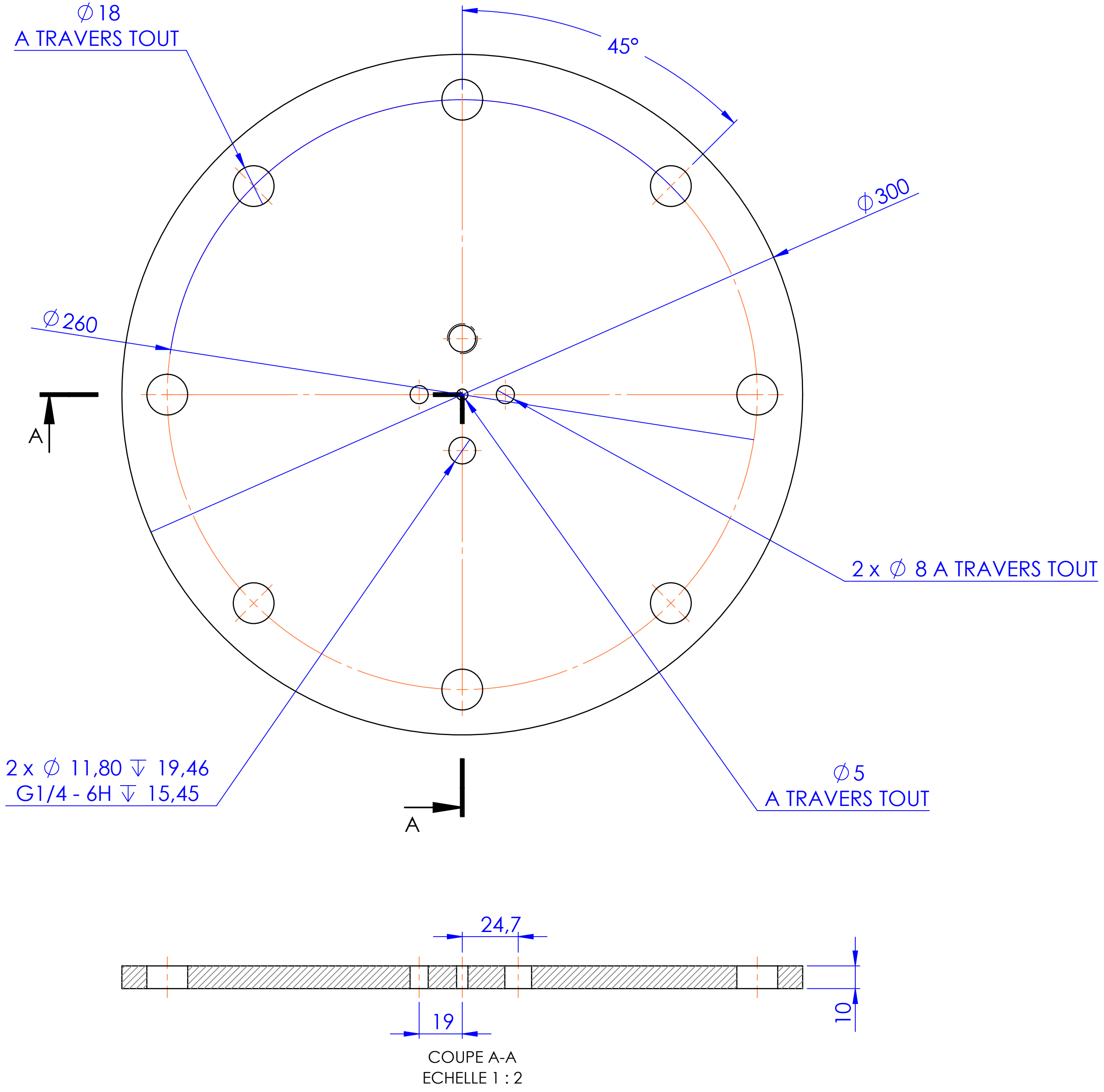

Tolérance: 0.1
Etat de surface: 1.6
Auteur: Arnaud Lion
Date: 30-04-20
Rév:
Projet: Banc pyrolyse
Matériau: 1.0037 (S235JR)
Masse: 5328.27 gr
Description:
Bride Ø 300
UCLouvain
Conception, Réalisation et Essais de Dispositifs ElectroMécaniques
Institute of Mechanics, Materials, and Civil Engineering
Place du levant, 2 bte L5.04.03 B-1348 Louvain-la-Neuve
Référence:
No. de plan: /
Echelle: 1:2
Feuille: 1/1
Format: A3

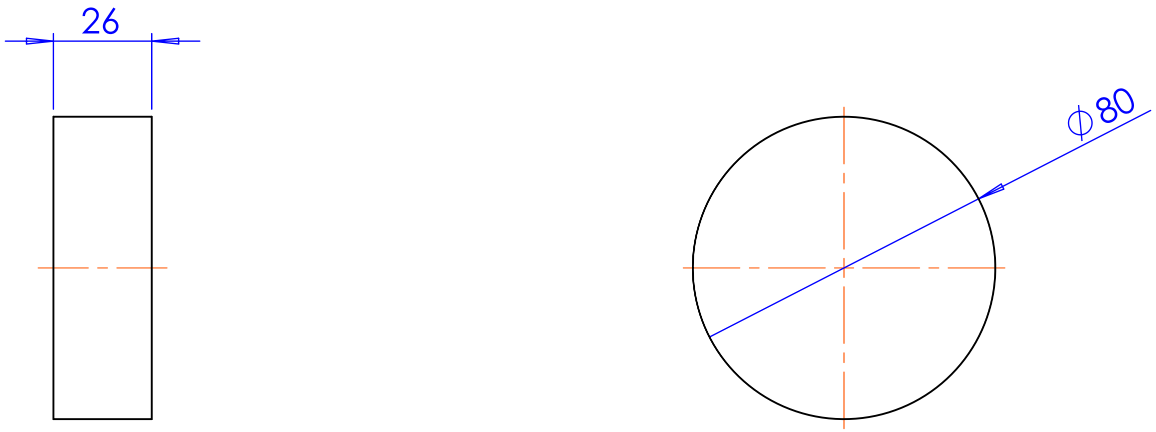

	Tolérance: 1
	Etat de surface: /
Auteur: Arnaud Lion	Date: 04-05-20
Rév: /	Projet: Banc pyrolyse
Matériau: AISI 304	
Masse: 1045.52 gr	Description: Entretoise
UCLouvain	Remarques: /
	No. de plan: /
	Echelle: 1:2
	Feuille: 1/1
	Format: A4

Conception, Réalisation et Essais de Dispositifs ElectroMécaniques

Institute of Mechanics, Materials, and Civil Engineering
Place du levant, 2 bte L5.04.03 B-1348 Louvain-la-Neuve

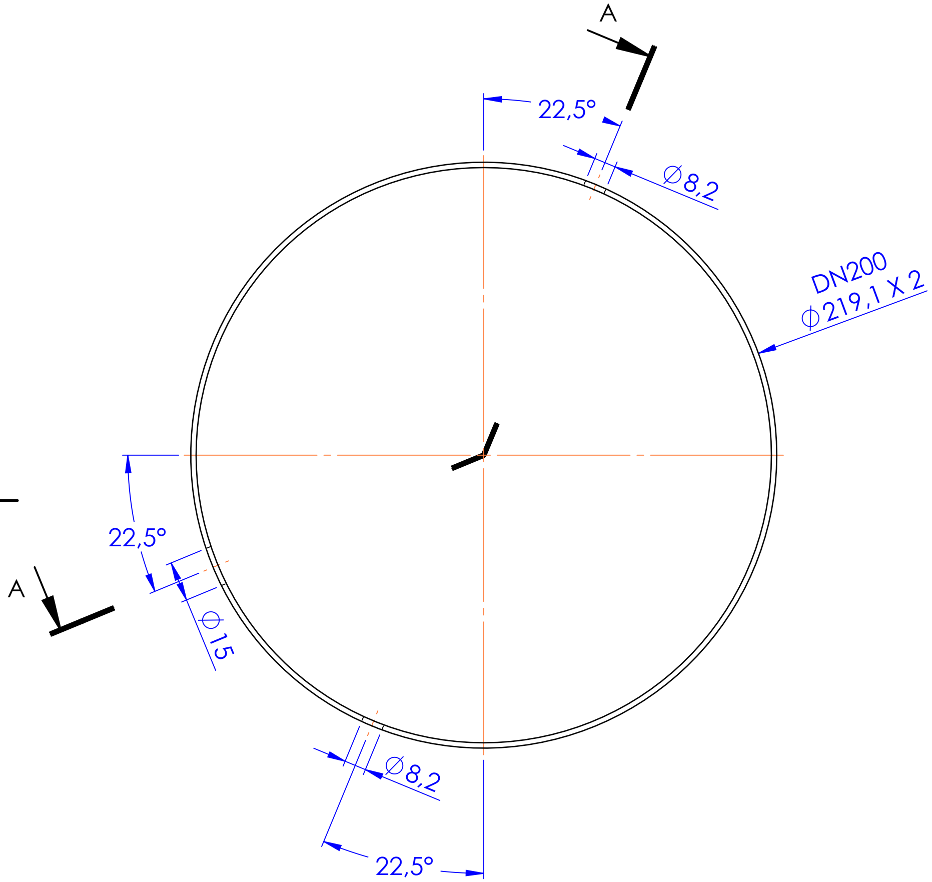

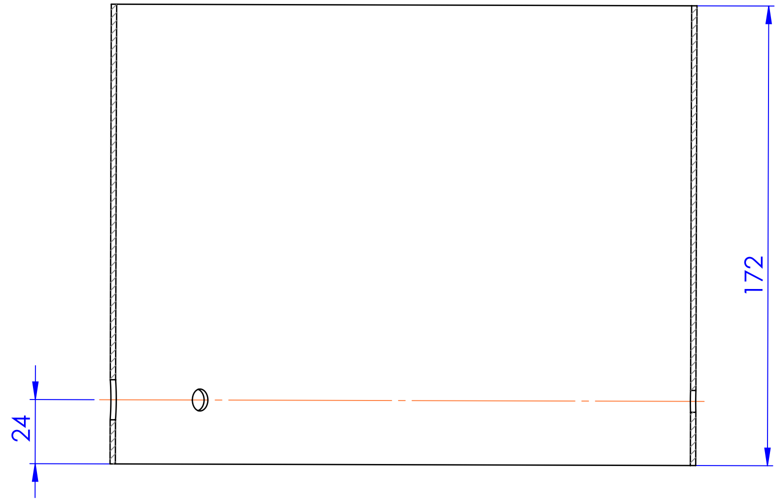

COUPE A-A

		Tolérance: 1	Etat de surface: /
Auteur: Arnaud Lion	Date: 04-05-20	Rév:	Projet: Banc pyrolyse
Matériau: AISI 304			
Masse: 1872.46 gr			Description: Tube DN 200

UCLouvain

Conception, Réalisation et Essais de Dispositifs ElectroMécaniques

Institute of Mechanics, Materials, and Civil Engineering

Place du levant, 2 bte L5.04.03 B-1348 Louvain-la-Neuve

Référence:

No. de plan: /

Echelle: 1:2
Feuille: 1/1
Format: A3

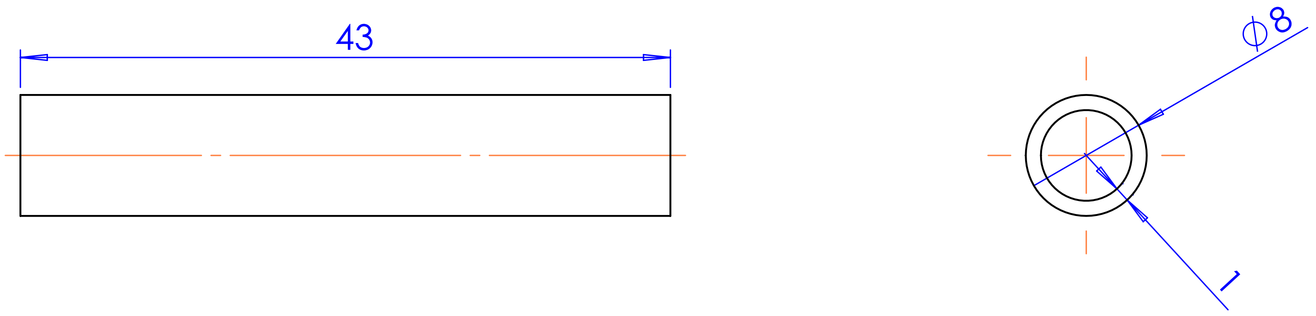

X 2

		Tolérance: 1	Etat de surface: /
Auteur: Arnaud Lion	Date: 04-05-20	Rév: /	Projet: Banc pyrolyse
Matériau: AISI 304			
Masse: 7.56 gr			Description: Tube sortie Gaz

UCLouvain

Conception, Réalisation et Essais de Dispositifs ElectroMécaniques

Institute of Mechanics, Materials, and Civil Engineering
Place du levant, 2 bte L5.04.03 B-1348 Louvain-la-Neuve

Remarques: /

No. de plan: /

Echelle: 2:1	Feuille: 1/1	Format: A4

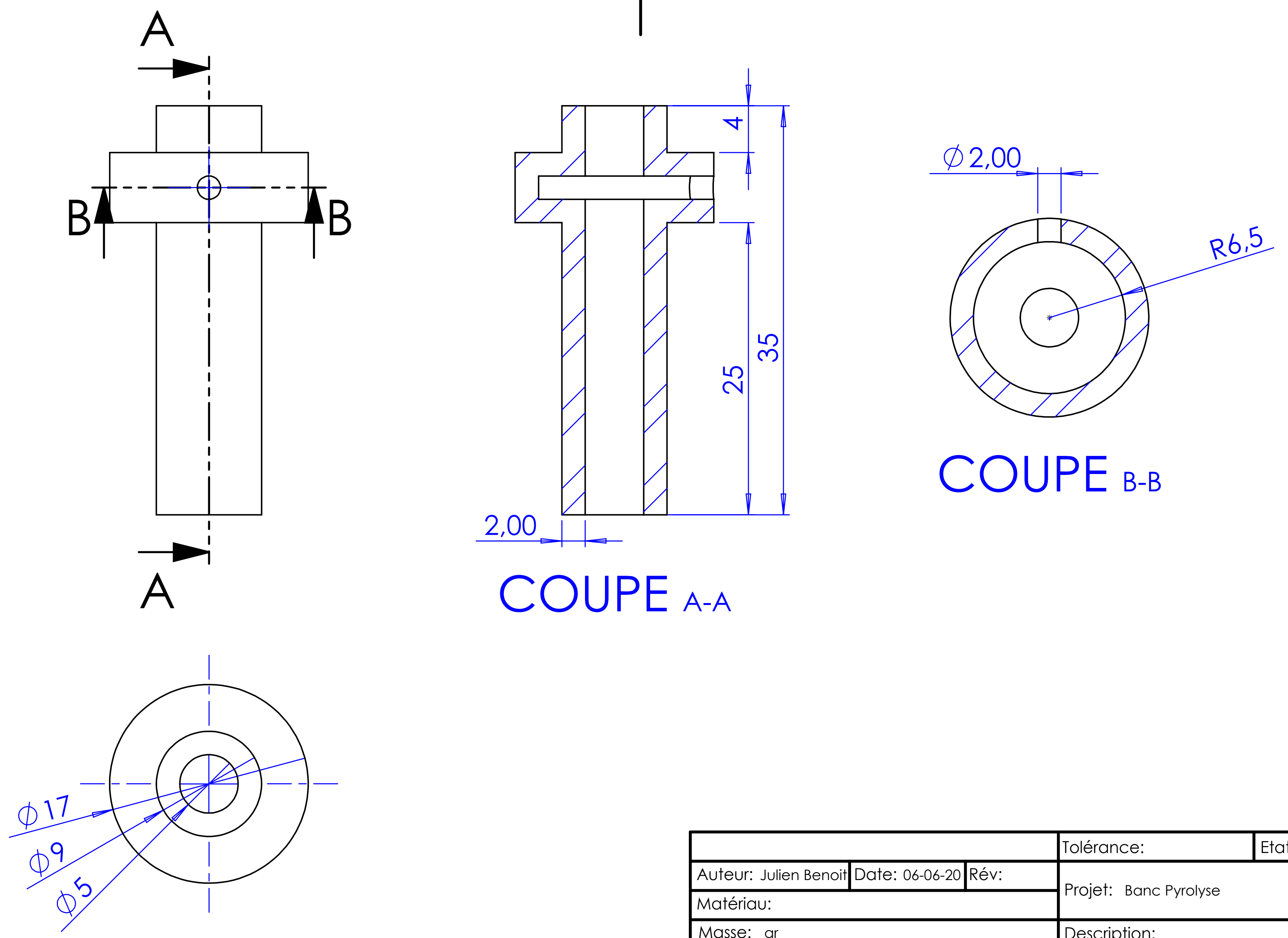

Auteur: Julien Benoit
Date: 06-06-20
Rév:
Matériau:
Masse: gr

UCLouvain

Conception, Réalisation et Essais de Dispositifs ElectroMécaniques

Institute of Mechanics, Materials, and Civil Engineering
Place du levant, 2 bte L5.04.03 B-1348 Louvain-la-Neuve

Tolérance:
Etat de surface:
Projet: Banc Pyrolyse
Description:
Gas seal
Remarques:
No. de plan:
Echelle: 2:1
Feuille: 1/1
Format: A4

Appendix B

Piping and instrumentation diagram (P&ID)

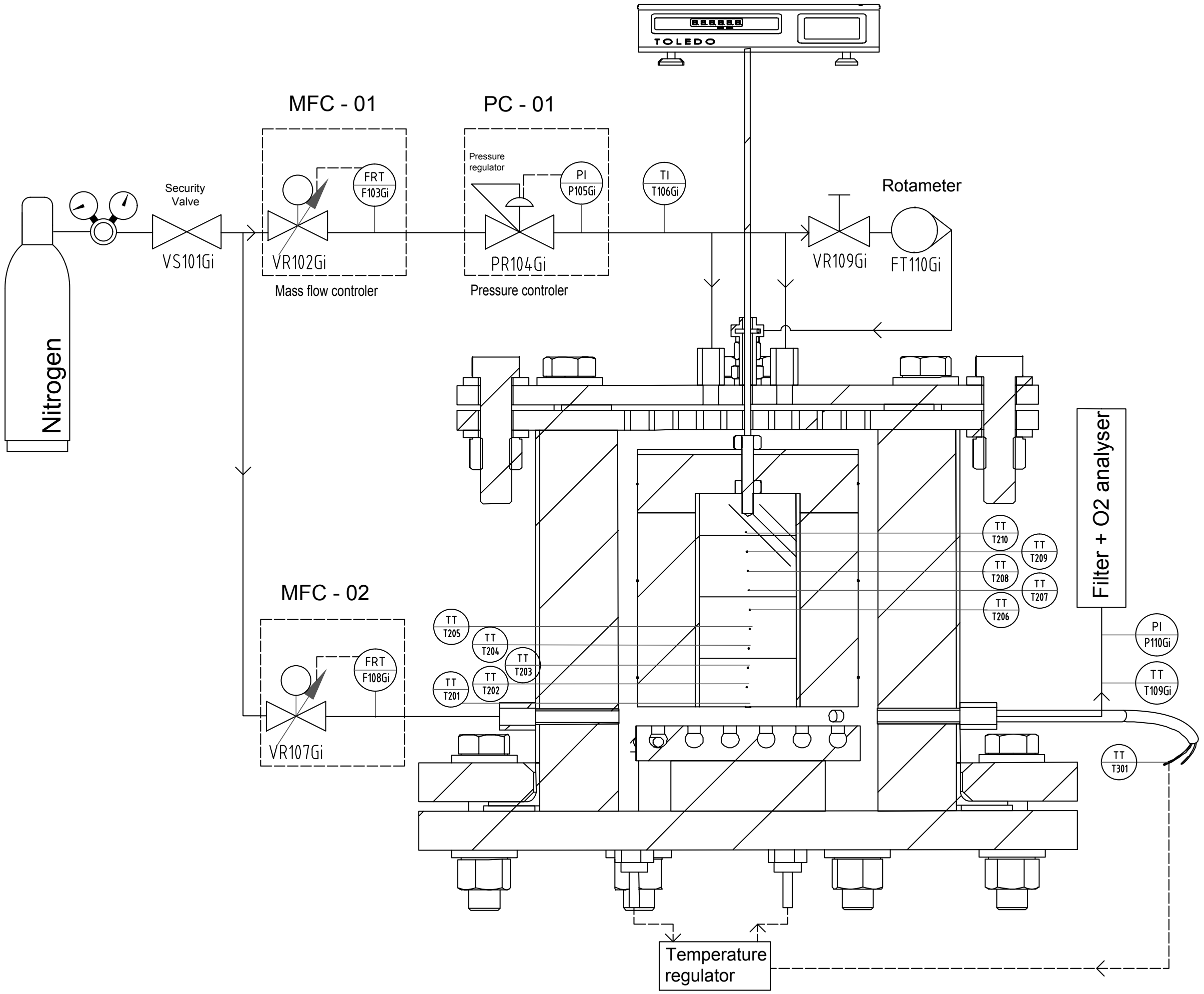

A4

UCL
Université catholique de Louvain

PROJET: BANC PYROLYSE
SUBPROJECT:
DESCRIPTION : PI&D DIAGRAM

Remarque(s) :

Resp :
Designer : JULIEN BENOIT
Date : 05-05-2020

iMMC-TFL- place du Levant, 2 - B1348 - Louvain-la-Neuve Belgique
Tél. +32(0)10-47.22.00 ; Fax. ++32(0)10-45.26.92; http ://www.uclouvain.be/immc

N° du dessin
1

Rev

Sheet.
1/1

GR	IDEN.	NUM	REF.	DEFINITION	REMARQUE	Contained fluid
1	VS	101	V101Gi	soupape de sécurité		Azote
1	VR	102	V102Gi	vanne commandée régulation débit principal	6,7 Nl/min	Azote
1	FRT	103	F103Gi	débitmètre massique thermique		Azote
1	PR	104	P104Gi	régulateur de pression		Azote
1	PI	105	P105Gi	pression entrée flux principal	1,02325 bar	Azote
1	TI	106	T106Gi	température d'entrée flux principal		Azote
1	VR	107	F107Gi	vanne commandée régulation débit		Azote
1	FRT	108	F107Gi	débitmètre massique thermique		Azote
1	VR	109	V109Gi	valve manuelle régulation débit cable pesée		Azote
1	FT	110	F110Gi	rotamètre débit cable pesée		Azote
1	TT	111	T111Gi	température de sortie du gaz		Gaz échappement
1	PI	112	P112Gi	pression de sortie du gaz	1, 01325 bar	Gaz échappement
2	TT	201	T201	température surface échantillon	r = 0, z = 10	
2	TT	202	T202	température au centre de l'échantillon	r = 0, z = 9	
2	TT	203	T203	température au centre de l'échantillon	r = 0, z = 8	
2	TT	204	T204	température au centre de l'échantillon	r = 0, z = 7	
2	TT	205	T205	température au centre de l'échantillon	r = 0, z = 6	
2	TT	206	T206	température au centre de l'échantillon	r = 0, z = 5	
2	TT	207	T207	température au centre de l'échantillon	r = 0, z = 4	
2	TT	208	T208	température au centre de l'échantillon	r = 0, z = 3	
2	TT	209	T209	température au centre de l'échantillon	r = 0, z = 2	
2	TT	210	T210	température au centre de l'échantillon	r = 0, z = 1	
3	TR	301	T301	température source de chaleur		

Appendix C

View factors

This appendix gives the view factor formulas that have been used for the different models presented in this work. All these formulas have been obtained thanks to the synthesis work carried out by J.R. Howell [57].

C.1 Disk to coaxial annular ring on parallel disk

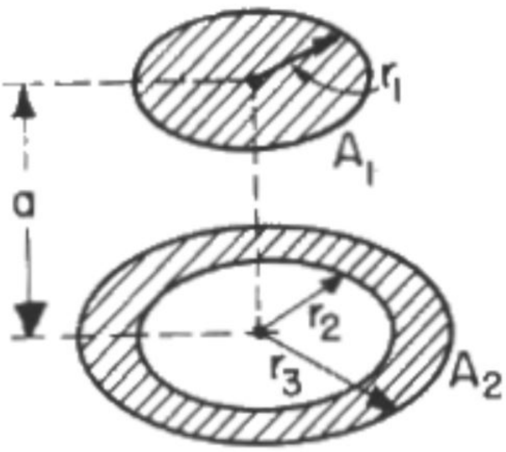

FIGURE C.1: Schematic of the configuration [57]

Definitions:

$$H = \frac{a}{r_1} \quad , \quad R_2 = \frac{r_2}{r_1} \quad , \quad R_3 = \frac{r_3}{r_1}$$

Governing equation [58] [59]:

$$F_{1-2} = \frac{1}{2}\left(R_3^2 - R_2^2 - \sqrt{(1+R_3^2+H^2)^2 - 4R_3^2} + \sqrt{(1+R_2^2+H^2)^2 - 4R_2^2}\right) \quad \text{(C.1)}$$

C.2 Exterior of inner cylinder to interior of coaxial outer cylinder of same length

Definitions:

$$R_1 = \frac{r_1}{h} \quad , \quad R_2 = \frac{r_2}{h} \quad , \quad A = R_2 + R_1 \quad , \quad B = R_2 - R_1$$

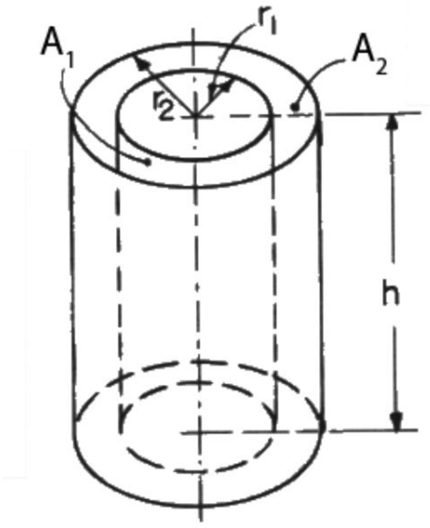

FIGURE C.2: Schematic of the configuration [57]

Governing equations [58] [59] [60] [61]:

$$F_{1-2} = \frac{1}{\pi R_1}\left[\frac{1}{2}\left(R_2^2 - R_1^2 - 1\right)\arccos\left(\frac{R_1}{R_2}\right) + \pi R_1 - \frac{\pi}{2}AB - 2R_1 \arctan\left(R_2^2 - R_1^2\right)^{1/2} + \left(\left(1+A^2\right)\left(1+B^2\right)\right)^{1/2}\arctan\left(\frac{\left(1+A^2\right)B}{\left(1+B^2\right)A}\right)^{1/2}\right] \tag{C.2}$$

C.3 Exterior of inner cylinder to interior of outer coaxial cylinder, inner cylinder entirely within outer

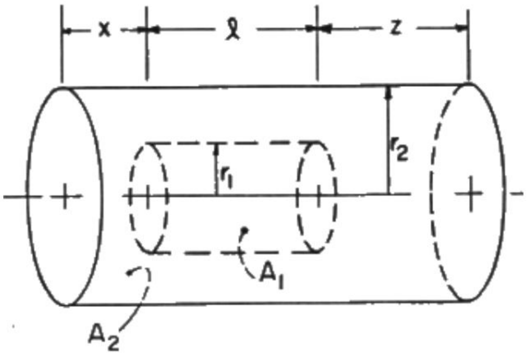

FIGURE C.3: Schematic of the configuration [57]

Definitions:

$$X = \frac{x}{r_2} \quad , \quad Z = \frac{z}{r_2} \quad , \quad L = \frac{l}{r_2} \quad , \quad R = \frac{r_1}{r_2}$$

$$A_\xi = \xi^2 + R^2 - 1 \quad , \quad B_\xi = \xi^2 - R^2 + 1$$

$$F_\xi = \frac{B_\xi}{8R\xi} + \frac{1}{2\pi}\left(\arccos\left(\frac{A_\xi}{B_\xi}\right) - \frac{1}{2\xi}\left(\frac{\left(A_\xi+2\right)^2}{R^2} - 4\right)^{1/2}\arccos\left(\frac{A_\xi R}{B_\xi}\right) - \frac{A_\xi}{2\xi R}\arcsin R\right) \tag{C.3}$$

Governing equations [62] [63]:

$$F_{1-2} = 1 + \frac{X}{L}F_X + \frac{Z}{L}F_Z - \frac{L+X}{L}F_{L+X} - \frac{L+Z}{L}F_{L+Z} \tag{C.4}$$

C.4 Exterior of inner cylinder to interior of outer coaxial cylinder, inner cylinder extends beyond one end of outer

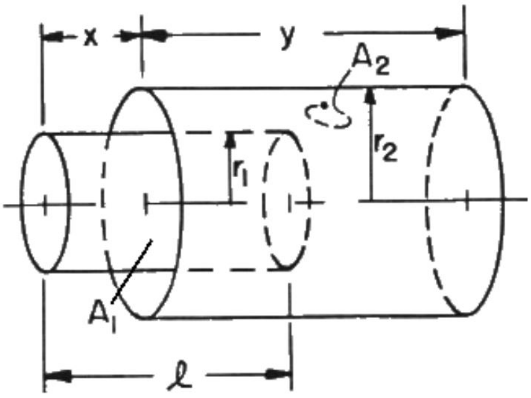

FIGURE C.4: Schematic of the configuration [57]

Definitions:

$$X = \frac{x}{r_2} \quad , \quad Y = \frac{y}{r_2} \quad , \quad L = \frac{l}{r_2} \quad , \quad R = \frac{r_1}{r_2}$$

Governing equation [62] [63]:

$$F_{1-2} = \frac{X}{L}F_X + \frac{L-X}{L}\left(1 - F_{L-X}\right) + \frac{Y+X-L}{L}F_{Y+X-L} - \frac{X+Y}{L}F_{X+Y} \tag{C.5}$$

C.5 Exterior of inner cylinder to interior of outer coaxial cylinder, inner cylinder extends beyond both ends of outer

Definitions:

$$X = \frac{x}{r_2} \quad , \quad Y = \frac{y}{r_2} \quad , \quad Z = \frac{z}{r_2} \quad , \quad L = \frac{l}{r_2} \quad , \quad R = \frac{r_1}{r_2}$$

Governing equation [62] [63]:

$$F_{1-2} = \frac{Y}{L} + \frac{X}{L}F_X + \frac{Z}{L}F_Z - \frac{X+Y}{L}F_{X+Y} - \frac{Y+Z}{L}F_{Y+Z} \tag{C.6}$$

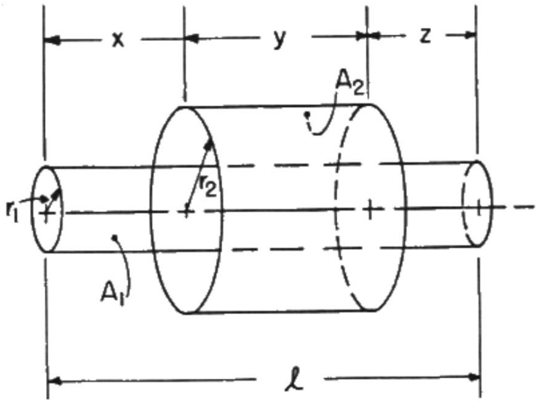

FIGURE C.5: Schematic of the configuration [57]

C.6 Exterior of inner cylinder to interior of outer coaxial cylinder, inner cylinder completely outside outer

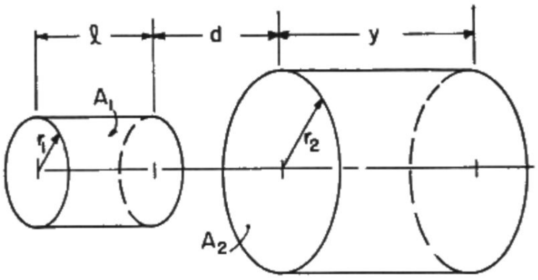

FIGURE C.6: Schematic of the configuration [57]

Definitions:

$$Y = \frac{y}{r_2} \quad , \quad D = \frac{d}{r_2} \quad , \quad L = \frac{l}{r_2} \quad , \quad R = \frac{r_1}{r_2}$$

Governing equation [62]:

$$F_{1-2} = \frac{D+L}{L} F_{D+L} + \frac{D+Y}{L} F_{D+Y} - \frac{D}{L} F_D - \frac{L+D+Y}{L} F_{L+D+Y} \tag{C.7}$$

Bibliography

[1] G. Gauthier. "Synthèse de biocarburants de deuxième génération : étude de la pyrolyse à haute température de particules de bois centimétriques". PhD thesis. Ecole des mines d'Alibi-Carmaux, Dec. 2013. URL: https://tel.archives-ouvertes.fr/tel-00999283.

[2] Shurong Wang et al. "Lignocellulosic biomass pyrolysis mechanism: A state-of-the-art review". In: *Progress in Energy and Combustion Science* 62 (2017), pp. 33 –86. DOI: 10.1016/j.pecs.2017.05.004. URL: http://www.sciencedirect.com/science/article/pii/S0360128517300266.

[3] A. J. Güell et al. "Mild Hydropyrolysis of Biomass Materials: Effect of Pressure on Product Tar Structures". In: *Advances in Thermochemical Biomass Conversion* (1993), pp. 1053–1067.

[4] T.R. Nunn et al. "Product composition and kinetics in the rapid pyrolysis of milled wood lignin". In: *Industrial and Engineering Chemistry Process Design and Development* 24.3 (Mar. 1985), pp. 836–844. DOI: 10.1021/i200030a053.

[5] Ali Akhtar, Vladimir Krepl, and Tatiana Ivanova. "A Combined Overview of Combustion, Pyrolysis, and Gasification of Biomass". In: *Energy & Fuels* 32.7 (2018), pp. 7294–7318. DOI: 10.1021/acs.energyfuels.8b01678.

[6] G.W. Huber, S. Iborra, and A. Corma. "Synthesis of Transportation Fuels from Biomass: Chemistry, Catalysts, and Engineering". In: *Chemical Reviews* 108.9 (June 2006), pp. 4044–4098. DOI: 10.1021/cr068360d.

[7] W.H. van Zyl et al. "Consolidated Bioprocessing for Bioethanol Production Using Saccharomyces cerevisiae". In: *Advances in Biochemical Engineering/Biotechnology* 108.108 (Apr. 2007), pp. 205–235. DOI: 10.1007/10_2007_061.

[8] P. Navi and F. Heger. *Comportement thermo-hydromécanique du bois*. Presses polytechniques et universitaires romandes. Oct. 2005.

[9] A. Demirbas. "Pyrolysis of ground beech wood in irregular heating rate conditions". In: *Journal of Analytical and Applied Pyrolysis* 73 (Mar. 2005), pp. 39–43. URL: https://www.sciencedirect.com/science/article/abs/pii/S0165237004000889.

[10] L. Chen et al. "Influence of Particle Size, Reactor Temperature and Gas Phase Reactions on Fast Pyrolysis of Beech Wood". In: *International Journal of Chemical Reactor Engineering* 8 (Apr. 2010).

[11] Colomba Di Blasi et al. "Pyrolytic behavior and products of some wood varieties". In: *Combustion and Flame* 124.1 (2001), pp. 165 –177. DOI: 10.1016/S0010-2180(00)00191-7. URL: http://www.sciencedirect.com/science/article/pii/S0010218000001917.

[12] R. Miller and J. Bellan. "A Generalized Biomass Pyrolysis Model Based on Superimposed Cellulose, Hemicellulose and Liqnin Kinetics". In: *Combustion Science and Technology - COMBUST SCI TECHNOL* 126 (July 1997), pp. 97–137. DOI: 10.1080/00102209708935670.

[13] Paul de Wild, H. Reith, and H.J. Heeres. "Biomass Pyrolysis for Chemicals". In: *Biofuels* 2 (Mar. 2011), pp. 185–208. DOI: `10.4155/bfs.10.88`.

[14] D. Neves et al. "Characterization and prediction of biomass pyrolysis products". In: *Progress in Energy and Combustion Science* 37 (Feb. 2011), pp. 611–630. DOI: `10.1016/j.pecs.2011.01.001`.

[15] Huy Tran et al. "Phenolic Impregnated Carbon Ablators (PICA) for Discovery class missions". In: *31st Thermophysics Conference*. DOI: `10.2514/6.1996-1911`. URL: `https://arc.aiaa.org/doi/abs/10.2514/6.1996-1911`.

[16] Brody K. Bessire, Sridhar A. Lahankar, and Timothy K. Minton. "Pyrolysis of Phenolic Impregnated Carbon Ablator (PICA)". In: *ACS Applied Materials & Interfaces* 7.3 (2015), pp. 1383–1395. DOI: `10.1021/am507816f`.

[17] Francesco Panerai et al. "Micro-tomography based analysis of thermal conductivity, diffusivity and oxidation behavior of rigid and flexible fibrous insulators". In: *International Journal of Heat and Mass Transfer* 108 (May 2017), pp. 801–811. DOI: `10.1016/j.ijheatmasstransfer.2016.12.048`.

[18] Brody K. Bessire and Timothy K. Minton. "Decomposition of Phenolic Impregnated Carbon Ablator (PICA) as a Function of Temperature and Heating Rate". In: *ACS Applied Materials & Interfaces* 9.25 (2017), pp. 21422–21437. DOI: `10.1021/acsami.7b03919`.

[19] A. W. Coats and J. P. Redfern. "Thermogravimetric analysis. A review". In: *Analyst* 88 (1053 1963), pp. 906–924. DOI: `10.1039/AN9638800906`. URL: `http://dx.doi.org/10.1039/AN9638800906`.

[20] Julien Blondeau. "Investigation of pulverised biomass combustion: detailed modelling of particle pyrolysis and experimental analysis of ash deposition". PhD thesis. Université catholique de Louvain - IMMC, May 2013. URL: `http://hdl.handle.net/2078.1/132579`.

[21] Enrico Biagini, C. Fantozzi, and Leonardo Tognotti. "Characterization of devolatilization of secondary fuels in different conditions". In: *Combustion Science and Technology* 176 (May 2004), pp. 685–703. DOI: `10.1080/00102200490428008`.

[22] Morten Gunnar Gronli. "A Theoritical and Experimental Study of the Thermal Degradation of Biomass". PhD thesis. The Norwegian University of Science and Technology, Nov. 1996.

[23] W. C. R. Chan. "Analysis of Chemical and Physical Processes During the Pyrolysis of Large Biomass Pellets". PhD thesis. University of Washington, Seattle, WA, 1983.

[24] R.A. Khalil et al. "Thermal analysis of energy crops: Part I: The applicability of a macro-thermobalance for biomass studies". In: *Journal of Analytical and Applied Pyrolysis* 81.1 (2008), pp. 52 –59. DOI: `10.1016/j.jaap.2007.08.004`. URL: `http://www.sciencedirect.com/science/article/pii/S0165237007001350`.

[25] Michaël Becidan, Øyvind Skreiberg, and Johan Hustad. "Products Distribution and Gas Release in Pyrolysis of Thermally Thick Biomass Residues Samples". In: *Journal of Analytical and Applied Pyrolysis - J ANAL APPL PYROL* 78 (Jan. 2007), pp. 207–213. DOI: `10.1016/j.jaap.2006.07.002`.

[26] Hong Lu. "Experimental and Modeling Investigations of Biomass Particle Combustion". PhD thesis. Ira A. Fulton College of Engineering and Technology; Chemical Engineering Department, 2006. URL: `https://scholarsarchive.byu.edu/etd/778`.

[27] Michel Bellais. "Modelling of the pyrolysis of large wood particles". PhD thesis. KTH - Royal Institute of Technology, 2007.

[28] H. Lu et al. "Effects of particle shape and size on devolatilization of biomass particle". In: 89.5 (2010), pp. 1156–1168. DOI: `10.1016/j.fuel.2008.10.023`.

[29] K.O Davidsson and J.B.C Pettersson. "Birch wood particle shrinkage during rapid pyrolysis". In: *Fuel* 81.3 (2002), pp. 263 –270. DOI: `10.1016/S0016-2361(01)00169-7`. URL: `http://www.sciencedirect.com/science/article/pii/S0016236101001697`.

[30] Won Chan Park, Arvind Atreya, and Howard Baum. "Experimental and theoretical investigation of heat and mass transfer processes during wood pyrolysis". In: *Combustion and Flame* 157 (Mar. 2010), pp. 481–494. DOI: `10.1016/j.combustflame.2009.10.006`.

[31] P.O. Okekunle et al. "Numerical and experimental investigation of intra-particle heat transfer and tar decomposition during pyrolysis of wood biomass". In: *Journal of Thermal Science and Technology* 6.3 (Apr. 2011), pp. 360–375. DOI: `10.1299/jtst.6.360`.

[32] P.O. Okekunle et al. "Effect of biomass size and aspect ratio on intra-particle tar decomposition during wood cylinder pyrolysis". In: *Journal of Thermal Science and Technology* 7.1 (Oct. 2012), pp. 1–15. DOI: `10.1299/jtst.7.1`.

[33] H. Rezaei et al. "A numerical and experimental study on fast pyrolysis of single woody biomass particles". In: *Applied Energy* 198 (2017), pp. 320–331. DOI: `10.1016/j.apenergy.2016.11.032`.

[34] Sykes Jr. "Decomposition Characteristics of a Char-Forming Phenolic Polymer Used for Ablative Composites". In: (Feb. 1967), p. 24. URL: `https://ntrs.nasa.gov/archive/nasa/casi.ntrs.nasa.gov/19670008814.pdf`.

[35] Howard E. Goldstein. "Pyrolysis Kinetics of Nylon 6–6, Phenolic Resin, and Their Composites". In: *Journal of Macromolecular Science: Part A - Chemistry* 3.4 (1969), pp. 649–673. DOI: `10.1080/10601326908053834`.

[36] Kimberly A. Trick and Tony E. Saliba. "Mechanisms of the pyrolysis of phenolic resin in a carbon/phenolic composite". In: *Carbon* 33.11 (1995), pp. 1509 –1515. DOI: `10.1016/0008-6223(95)00092-R`. URL: `http://www.sciencedirect.com/science/article/pii/000862239500092R`.

[37] K.A. Trick, T.E. Saliba, and S.S. Sandhu. "A kinetic model of the pyrolysis of phenolic resin in a carbon/phenolic composite". In: *Carbon* 35.3 (1997), pp. 393 –401. DOI: `10.1016/S0008-6223(97)89610-8`. URL: `http://www.sciencedirect.com/science/article/pii/S0008622397896108`.

[38] Frank S. Milos et al. "Mars Pathfinder Entry Temperature Data, Aerothermal Heating, and Heatshield Material Response". In: *Journal of Spacecraft and Rockets* 36.3 (1999), pp. 380–391. DOI: `10.2514/2.3457`. URL: `https://arc.aiaa.org/doi/pdf/10.2514/2.3457`.

[39] F. S. Milos et al. "Analysis of Galileo Probe Heatshield Ablation and Temperature Data". In: *Journal of Spacecraft and Rockets* 36.3 (1999), pp. 298–306. DOI: `10.2514/2.3465`. URL: `https://arc.aiaa.org/doi/10.2514/2.3465`.

[40] Michael Wright, Frank Milos, and Phillippe Tran. "Afterbody Aeroheating Flight Data for Planetary Probe Thermal Protection System Design". In: *Journal of Spacecraft and Rockets - J SPACECRAFT ROCKET* 43 (Sept. 2006), pp. 929–943. DOI: `10.2514/1.17703`.

[41] Francisco Torres-Herrador et al. "A high heating rate pyrolysis model for the Phenolic Impregnated Carbon Ablator (PICA) based on mass spectroscopy experiments". In: *Journal of Analytical and Applied Pyrolysis* 141 (2019), p. 104625. DOI: `10.1016/j.jaap.2019.05.014`. URL: `http://www.sciencedirect.com/science/article/pii/S0165237019301603`.

[42] Hsi-Wu Wong et al. "Detailed analysis of species production from the pyrolysis of the Phenolic Impregnated Carbon Ablator". In: *Journal of Analytical and Applied Pyrolysis* 122 (2016), pp. 258 –267. DOI: `10.1016/j.jaap.2016.09.016`. URL: `http://www.sciencedirect.com/science/article/pii/S016523701630211X`.

[43] Wen-guang Wu et al. "Isothermal Pyrolysis of Biomass by Macro-TG". In: *Asia-Pacific Power and Energy Engineering Conference, APPEEC* (Mar. 2009). DOI: `10.1109/APPEEC.2009.4918456`.

[44] Huy K. Tran et al. *Phenolic Impregnated Carbon Ablators (PICA) as Thermal Protection Systems for Discovery Missions*. Tech. rep. NASA Ames Research Center; Moffett Field, CA United States, 1997. URL: `https://ntrs.nasa.gov/search.jsp?R=19970017002`.

[45] W.A.Jr. Cote F.F.P. Kollmann. *Principles of Wood Science and Technology, I Solid Wood*. Springer-Verlag Berlin Heidelberg, 1968. ISBN: 978-3-642-87928-9.

[46] J. Blondeau and H. Jeanmart. "Biomass pyrolysis at high temperatures: Prediction of gaseous species yields from an anisotropic particle". In: *Biomass and Bioenergy* 41 (June 2012), pp. 107–121. DOI: `10.1016/j.biombioe.2012.02.016`.

[47] T.K. Chu and C.Y. Ho. "Thermal Conductivity and Electrical Resistivity of Eight Selected AISI Stainless Steels". In: *Mirkovich V.V. (eds) Thermal Conductivity* 15 (1978), pp. 79–104. DOI: `10.1007/978-1-4615-9083-5_12`.

[48] Eric Meier. *WOOD! Identifying and Using Hundreds of Woods Worldwide*. The Wood Database, 2015. ISBN: 9780982246030.

[49] Engineering ToolBox. *Emissivity Coefficients Materials, The radiation heat transfer emissivity coefficient of some common materials as aluminum, brass, glass and many more*. 2003. URL: `https://www.engineeringtoolbox.com/emissivity-coefficients-d_447.html`. (accessed: 29.05.2020).

[50] M. Gasch et al. "Progress in Manufacturing Characterizing Domestic Lyocell PICA (PICA-D) and Comparison to Heritage PICA". Poster presented at the meeting Outer Planets Advisory Group Meeting (OpAG Spring 2019). Apr. 2019.

[51] AZoM. *Stainless Steel - Grade 304 (UNS S30400)*. 2001. URL: `https://www.azom.com/article.aspx?ArticleID=965`. (accessed: 29.05.2020).

[52] SubsTech Substance Technologies. *Stainless steel AISI 304*. 2012. URL: `https://www.substech.com/dokuwiki/doku.php?id=stainless_steel_aisi_304`. (accessed: 29.05.2020).

[53] Battelle Memorial Institute. Defense Metals Information Center and W. Wood. *DMIC Report 177: Thermal Radiative Properties of Selected Materials*. Plenum Press handbooks of high-temperature materials. 1962. URL: `https://books.google.be/books?id=43vGGwAACAAJ`.

[54] R. K. Shah and A. L. London. *Laminar Flow Forced Convection in Ducts 1st Edition*. Thomas Irvine and James P. Hartnett, Jan. 1978. ISBN: 9781483191300. URL: `https://www.elsevier.com/books/laminar-flow-forced-convection-in-ducts/shah/978-0-12-020051-1`.

[55] F. Kreith and W.Z. Black. *Basic Heat Transfer*. Harper & Row, 1980. ISBN: 9780700225187. URL: `https://books.google.be/books?id=NgVRAAAAMAAJ`.

[56] O. A. Sergeev, A. G. Shashkov, and A. S. Umanskii. "Thermophysical properties of quartz glass". In: *Journal of engineering physics* 43 (Dec. 1982), 1375–1383. DOI: `https://doi.org/10.1007/BF00824797`.

[57] J.R. Howell. *A catalog of radiation heat transfer configuration factors*. URL: `http://www.thermalradiation.net/tablecon.html`. (accessed: 31.05.2020).

[58] D.C. Hamilton and W.R. Morgan. *Radiant-interchange Configuration Factors*. National Advisory Committee for Aeronautics. Dec. 1952.

[59] H. Leuenberger and R.A. Person. *Compilation of Radiation Shape Factors for Cylindrical Assemblies*. American Society of Mechanical Engineers. Paper. American Society of Mechanical Engineers, 1956. URL: `https://books.google.be/books?id=71wlAQAAIAAJ`.

[60] V.T. Alexandrov. "Determination of the angular radiation coefficients for a system of two coaxial cylindrical bodies". In: *Inzh. Fiz. Zh.* 8.5 (1965), pp. 609–612.

[61] H.Brockmann. "Analytic angle factors for the radiant interchange among the surface elements of two concentric cylinders". In: *International Journal of Heat and Mass Transfer* 37.7 (May 1994), pp. 1095–1100. DOI: `https://doi.org/10.1016/0017-9310(94)90195-3`.

[62] S.N. Rea. "Rapid method for determining concentric cylinder radiation view factors". In: *AIAA Journal* 13.8 (May 2012), pp. 1122–1123. DOI: `10.2514/3.6964`.

[63] K.N. Shukla and D. Ghosh. "Radiation configuration factors for concentric cylinder bodies in enclosure". In: *Indian J. Technology* 23 (June 1985), pp. 244–246.

UNIVERSITÉ CATHOLIQUE DE LOUVAIN
École polytechnique de Louvain
Rue Archimède, 1 bte L6.11.01, 1348 Louvain-la-Neuve, Belgique | **www.uclouvain.be/epl**